# Development of Proton Oxide-ion Electron Triple Conducting Electrodes for Protonic Ceramic Cells

# プロトンセラミックセルに対するプロトン－酸化物イオン－電子混合伝導性空気極の開発

**Ning WANG**

**Graduate School of Chemical Sciences and Engineering**

**Hokkaido University**

**September 2020**

# Abstract

It is a great challenge to address global energy and climate change crises by new clean energy devices utilizing renewable energy sources (*e.g.*, solar, wind, geothermal, biofuels). Protonic ceramic cells (PCCs) based on the proton conducting Ba(Zr, Ce)$O_3$ solid electrolytes are a highly efficient storage device of natural energy with, because they can produce hydrogen by steam electrolysis with a use of electrical powers originating from natural energy (EC mode) and conduct power generation with the hydrogen products (FC mode). Nevertheless, the performances of the current devices lag far behind those expected from the electrolyte resistances at the temperatures below 600 ℃. A major reason for the reduced performance at lower temperatures is the occurrence of the considerable interfacial polarization at air electrodes in both FC and EC modes. The well-known air electrode materials, such as $La_{1-x}Sr_xCo_{0.2}Fe_{0.8}O_3$ (LSCF), $Sm_{0.5}Sr_{0.5}CoO_3$ (SSC) and so on are oxide-ion conductors; there is a mismatch of main ionic carriers between the air electrode and the electrolyte, which limits the efficient area for air electrodes' reaction to the air electrode–electrolyte–gas triple phase boundaries (TPB). The materials having efficient proton conductivity together with electron and oxide ion conductivity, if available, is expected to extend the effective reaction area to the overall surface of the electrode, and thus decreases the interfacial polarization resistances. Such $H^+/O^{2-}/e^-$ triple conducting materials could be derived from the oxides having the pronounced hydration capability at intermediate temperatures. The main objective of this thesis is to explore the tiple perovskite type oxides with high hydration capability at intermediate temperatures, and figure out the hydration mechanism to lead a robust guideline for the material design. Finally, the excellent cell performances were demonstrated with the PCCs using triple conducting air electrodes.

In chapter 1, the general background of energy conversion devices based on protonic

ceramic cells was firstly described. Then the progresses on PCCs were summarized for the comprehensive understanding of proton-conducting oxide cells. The issues of PCCs were analyzed and the aims of this thesis were proposed.

In chapter 2, experimental and theoretical techniques used in this thesis were surveyed.

In chapter 3, $La_{0.8}Sr_{0.2}Co_{1-x}Ni_xO_{3-\delta}$ (LSCN; $x$=0-0.3) families were found to undergo the thermochemical hydration and take favorably proton defects in the concentration of 0.06–0.15 mole fraction at around 400 °C by exposed to water pressure of 0.023 atm. Hence LSCN electrodes could efficiently reduce the polarization resistances regarding to the water formation and dissociation reactions on protonic ceramic fuel cells (PCFCs) and protonic ceramic electrolysis cells (PCECs), respectively, attributed to the mixed $H^+/e^-/O^{2-}$ triple phase conductivity. The thin-film cells based on Zr-rich $BaZr_{0.4}Ce_{0.4}Y_{0.2}O_3$ electrolyte yielded the peak power density of 0.88 W $cm^{-2}$ in FC mode and electrolysis current of 1.09 A $cm^{-2}$ at 1.3 V in EC mode at 600 ℃, respectively, which are superior to the well-known $La_{0.6}Sr_{0.4}Co_{0.2}Fe_{0.8}O_3$ electrodes under the same conditions. The XAS measurements proved that the hydration did not involve the valence change of O and metal atoms.

The chapter 4 reported on the massive uptake of proton carriers in cubic perovskite type $La_{0.7}Sr_{0.3}MnO_{3-\delta}$ at intermediate temperatures through the hydration reaction triggered by the charge disproportionation between oxygen and manganese redox. $La_{0.7}Sr_{0.3}MnO_{3-\delta}$ underwent the decline of antibonding O 2*p* states hybridized with Mn 3*d* orbitals together with oxidation of $Mn^{3+}$ to $Mn^{4+}$ by hydration, and thus, retained bulk protons in the concentration of 0.14 mole fraction in wet air at around 420 °C, which was corresponding to the concentration of the well-known protonic conductor $BaZr_xCe_{0.8-x}Y_{0.2}O_{3-\delta}$. These results offered a general concept to design mixed $H^+/O^{2-}/e^-$ triple conductors operating in air conditions, namely, that transition metal oxides

possessing holes on O 2*p* states together with oxygen vacancies could be promising candidates.

In chapter 5, it was also demonstrated that a cubic-type $La_{0.7}Sr_{0.3}Mn_{0.7}Ni_{0.3}O_{3-\delta}$ (C-LSMN7373) perovskite was promising for intermediate-temperature PCFCs because of the sufficient $H^+/e^-/O^{2-}$ triple conductivity. The oxides could be hydrated by gaining 0.1 mole fraction $H_2O$ under wet air at 415 °C, as confirmed by thermogravimetry analysis. An *in situ* extended X-ray absorption fine structure (EXAFS) analysis revealed that the hydration reaction took place via the association between $H_2O$ and oxygen vacancy, coupled with the charge disproportionation between Mn and O atoms. Rhombohedral-type $La_{0.7}Sr_{0.3}Mn_{1-x}Ni_xO_{3-\delta}$ could not undergo hydration because the oxygen vacancy concentration required for water association was lower than the cubic phase concentration. The cathode performances of various PCFCs were examined by fabricating thin-film cells based on a $Ba(Zr_{0.4}Ce_{0.4}Y_{0.2})O_3$ electrolyte. The peak power density of the PCFCs with cubic-type LSMN7373 cathode was 386 mW $cm^{-2}$ at 600 °C, which was much higher than the reported values for the Zr-rich side electrolytes. Moreover, the cathodic polarization resistance was lower than that of the cell with the widely used $La_{0.6}Sr_{0.4}Co_{0.2}Fe_{0.8}O_3$ cathode below 550 °C.

The chapter 6 is the summary of this thesis. The hydration enthalpy of $La_{0.8}Sr_{0.2}Co_{0.7}Ni_{0.3}O_{3-\delta}$ and C-$La_{0.7}Sr_{0.3}Mn_{0.7}Ni_{0.3}O_{3-\delta}$ were about -110 kJ $mol^{-1}$ as calculated from the dehydration temperatures under water pressure of 0.023 atm. Therefore, these oxides must retain sufficient amount of water even in the temperature range of the PCC's operation, i.e. 500–600 °C under water partial pressure of 0.1 atm. The performances of PCECs and PCFCs with cubic-type $La_{0.7}Sr_{0.3}Mn_{0.7}Ni_{0.3}O_{3-\delta}$ air electrodes were superior to those reported for the corresponding cells with $O^{2-}/e^-$ double conductors at 500 and 600 °C, because the interfacial polarization resistances of the formers were significantly lower than those of the latter. It was concluded that the hydrated oxides could extend the reaction areas for the water formation or splitting

reactions on the proton conducting solid electrolytes due to the $H^+/O^{2-}/e^-$ triple conductivity and thus, were promising air electrodes for the intermediate temperature PCCs.

# Table of contents

**Abstract** ..... I

**Chapter 1 General introduction** ..... 1

1-1 Solid oxide fuel cells ..... 1

1-2 Protonic ceramic cells ..... 4

1-3 Protonic ceramic fuel cells ..... 7

1-4 Protonic ceramic electrolysis cells ..... 9

1-5 Reversible protonic ceramic electrochemical cells ..... 10

1-6 The issue of protonic ceramic fuel cells ..... 11

1-7 Composite air electrodes ..... 15

1-8 Mixed $H^+/O^{2-}/e^-$ triple conductors as advanced electrode materials ..... 19

1-9 Objective of this thesis ..... 21

1-10 Contents of this thesis ..... 23

1-11 References ..... 25

**Chapter 2 General experiments** ..... 30

2-1 Synthesis of perovskite oxides ..... 30

2-2 Fabrication of protonic ceramic cells ..... 31

2-3 Characterizations ..... 33

2-3-1 Structural characterizations ..... 33

2-3-2 Rietveld structure refinement ..... 33

2-3-3 Thermodynamic characterizations for hydration.....33

2-3-4 Single crystal X-ray absorption spectroscopy.....34

2-3-5 Fuel cell and electrolysis tests.....34

**Chapter 3 Enormous proton carriers incorporated $La_{0.8}Sr_{0.2}Co_{1-x}Ni_xO_{3-\delta}$ as highly efficient air electrodes for protonic ceramic cells**.....36

3-1 Introduction.....36

3-2 Experimental Section.....38

3-2-1 Synthesis of LSCN.....38

3-2-2 Fabrication of PCFC/ECs.....38

3-2-3 Characterizations.....39

3-3 Results and discussion.....42

3-3-1 Preparation of LSCN.....42

3-3-2 Hydration/dehydration reactions of LSCN oxides.....45

3-3-3 Protonic ceramic cells with LSCN air electrodes.....54

3-4 Conclusions.....64

3-5 References.....65

**Chapter 4 Incorporation of bulk proton carriers in cubic perovskite manganite driven by interplays of oxygen and manganese redox**.....68

4-1 Introduction.....68

4-2 Experimental section.....69

4-2-1 Synthesis of LSM.....69

4-2-2 Characterizations .....69

4-3 Results .....72

4-3-1 Preparation of LSM .....72

4-3-2 Hydration/dehydration reactions of LSM .....78

4-3-3 Iodometry of dehydrated LSM .....85

4-3-4 Mn *K*-edge EXAFS .....86

4-3-5 *In-situ* EXAFS .....91

4-4 Discussion .....94

4-4-1 Reaction mechanism .....94

4-4-2 Comparison of proton concentrations to other triple conductors .....99

4-5 Conclusions .....100

4-6 References .....101

**Chapter 5 Mixed Proton–electron–oxide Ion Triple Conducting Manganite as Efficient Cobalt-free Cathode for Protonic Ceramic Fuel Cells** .....104

5-1 Introduction .....104

5-2 Experimental section .....106

5-2-1 Synthesis of LSMN .....106

5-2-2 Fabrication of PCFCs .....106

5-2-3 Characterizations .....106

5-3 Results and discussion .....108

5-3-1 Preparation of LSMN .....108

5-3-2 Hydration/dehydration reactions of LSMN .....109

5-3-3 *In-situ* Mn K-edge EXAFS .....114

5-3-4 Hydration ability of LSMN .....127

5-3-5 Performances of LSMN cathodes on PCFCs.....129

5-4 Conclusions .....142

5-5 References .....143

**Chapter 6 Summary** .....145

**Publications**.....149

**Acknowledgements** .....150

# Chapter 1 General introduction

## 1-1 Solid oxide fuel cells

With the emergent growth of global economy, ones are facing the climate and energy crises and the stringent regulations on fossil fuels, and the currently serious situation drives a shift toward renewable energy sources (e.g., solar, wind, and geothermal) and cleaner, more efficient utilization of green fuels, i.e. hydrogen. Therefore, it is urgent task for many material chemists to develop advanced electrode and electrolyte materials for electrochemical energy-conversion and storage devices, such as proton-exchange membrane fuel cells (PEMFCs),[1-3] solid oxide fuel cells (SOFCs),[4-7] lithium batteries,[8,9] flow batteries,[10,11] and alkaline water electrolyzers,[12,13] solid oxide electrolysis cells (SOECs),[14,15] reversible ceramic electrochemical cells,[16-18] and so on,[19,20] as shown in Figure 1-1.[21-23]

SOFC is an electrochemical device, based on oxide-ion conducting solid electrolyte, typically Y-dope $ZrO_2$ (YSZ), and enables efficient electrical power generation with by utilizing hydrogen (or hydrocarbons) fuels with achieving more than 60% ideal efficiency (Figure 1-2). SOFCs possess several particularly attractive advantages compared with PEMFCs. I) Fuel flexibility, they can directly use hydrocarbons fuels, even solid carbon, with efficiently reforming hydrocarbons/carbon to $H_2$ and CO in the anode, because of the high operating temperatures (800-1000 ℃). II) High efficiency, SOFCs produce electricity directly from fuels upon electrochemical processes, with the efficiency over the limits of the Carnot cycle. III) Materials choice: the device does not need to use precious-metal (Pt) catalysts. Another benefit offered by high operating temperatures is that the heat produced by the SOFCs stack can be utilized by endothermic steam reforming reactions, which can increase overall system efficiency when operating on hydrocarbon or alcohol fuels. The total energy efficiency of the SOFCs system can reach up to 90% in combined high-quality waste heat and electricity

applications by recovering waste heat.

According to these advantages, recently the SOFCs system (Ceres Co Ltd.) has been applied to middle or small-sized power plants in EU and USA, in which hydrogen fuel produced by water electrolysis with renewable electricity and bio gas were converted to electricity with efficiency of more than 50%. However, the conventional SOFCs together with SOECs suffer from high running cost and poor long-term stability because of the serious material corrosion under high operation temperatures around 800 °C. Therefore, in order to solve these problems, it is strongly demanded to lower the operating temperature of SOFC devices into the range below 600 °C.

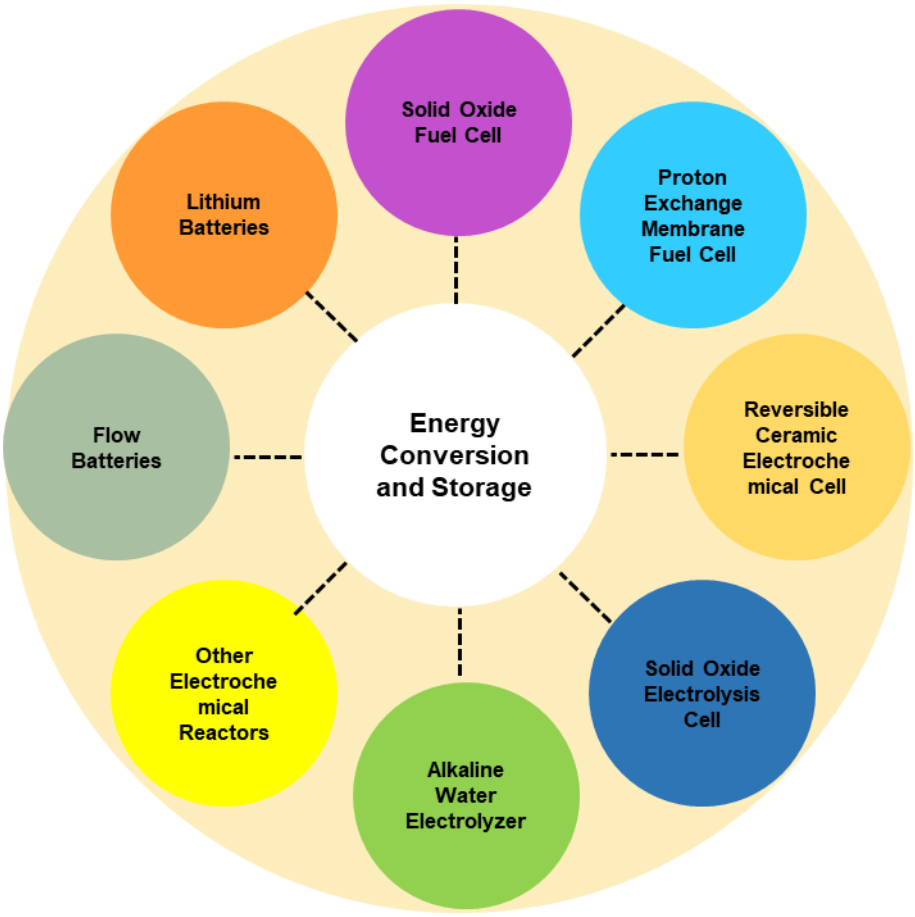


Figure 1-1 Current electrochemical devices for energy conversion and storage.

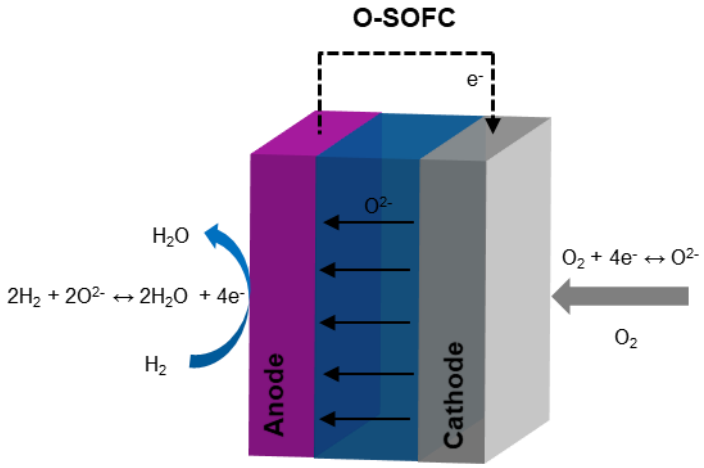


Figure 1-2 Schematic representation of an oxide-ion conducting solid oxide fuel cell.

## 1-2 Protonic ceramic cells

Proton-conducting ceramic fuel cells (PCFCs) and electrolysis cells (PCECs) are promising alternative to the conventional SOFCs and SOECs, which are based on the protonic conducting ceramic electrolytes, typically, $Ba(Zr, Ce)O_3$ base oxides. Because the protonic conducting $Ba(Zr, Ce)O_3$ possesses the lower activation energy for protonic conduction (0.3-0.5 eV) than that of oxide-ion conducting YSZ (0.8 eV) and thus exhibits significantly high conductivity (> $10^{-3}$ S $cm^{-1}$) at temperatures above 400 ℃, the related devices can be operative at temperatures below 600 ℃. Unlikely in SOFCs, PCFCs/ECs do not produce water in the fuel electrode side, so that the dilution of hydrogen fuel does not occurs during operation, which results in not only increase of the fuel utilization but also suppress of oxidation of metal catalysts.[24, 25, 26, 27] Therefore, the protonic ceramic cells deserve the extensive research aiming to next-generation intermediate temperature energy conversion systems with high efficiency, cost-effectiveness and long-term durability.

PCFCs consist of three parts, *i.e*. anode, air electrode and electrolyte (Figure 1-3a). The electrolyte is a dense solid oxide membrane which transports mainly protons from the anode to the air electrode. The anode is porous electrodes comprising typically Ni-electrolyte cermet and promotes the oxidation of fuels (*e.g*. hydrogen, hydrocarbons, alcohols, *etc.*) with separating them into protons and electrons at the electrolyte-electrode-gas triple phase boundary. The air electrode is needed to promote the reduction of oxygen molecules to oxide ions, and recombination of the resultant oxide ions and protons provided from electrolyte membrane to produce water. Electrons transport from the anode to the air electrode through an external circuit and load where the produced electricity is utilized.

PCECs operate essentially in the reverse mode of the PCFCs for hydrogen production by water electrolysis (Figure 1-3b). By applying DC power, steam is separated to

oxygen molecules and protons and electrons via oxygen evolution reaction (OER) in the anode. Protons migrate from the air electrode to the cathode through the proton-conducting electrolyte membrane. At the cathode, protons provide from cathode recombine with electrons to hydrogen gas. PCECs are very promising energy storage devices for the conversion of renewable electricity to hydrogen energy, because standard electrode potential for water splitting is decreased with temperature and thus the electrolysis potentials of PCECs tend to be lower than those of the alkaline electrolysis at around room temperature.[28]

RePCFCs are the combined system of PCFCs and PCECs, and can be categorized to energy harvesting system (Figure 1-3c). When the excess electricity generates from solar or wind at abundant days/seasons, it is applied to the RePCFCs to storage as a hydrogen energy in electrolysis mode. However, fuel cell mode will start to generate electrical power by consumption of the stored hydrogen, conversely, when the additional electricity is needed to make up for the insufficient electricity from solar and wind.

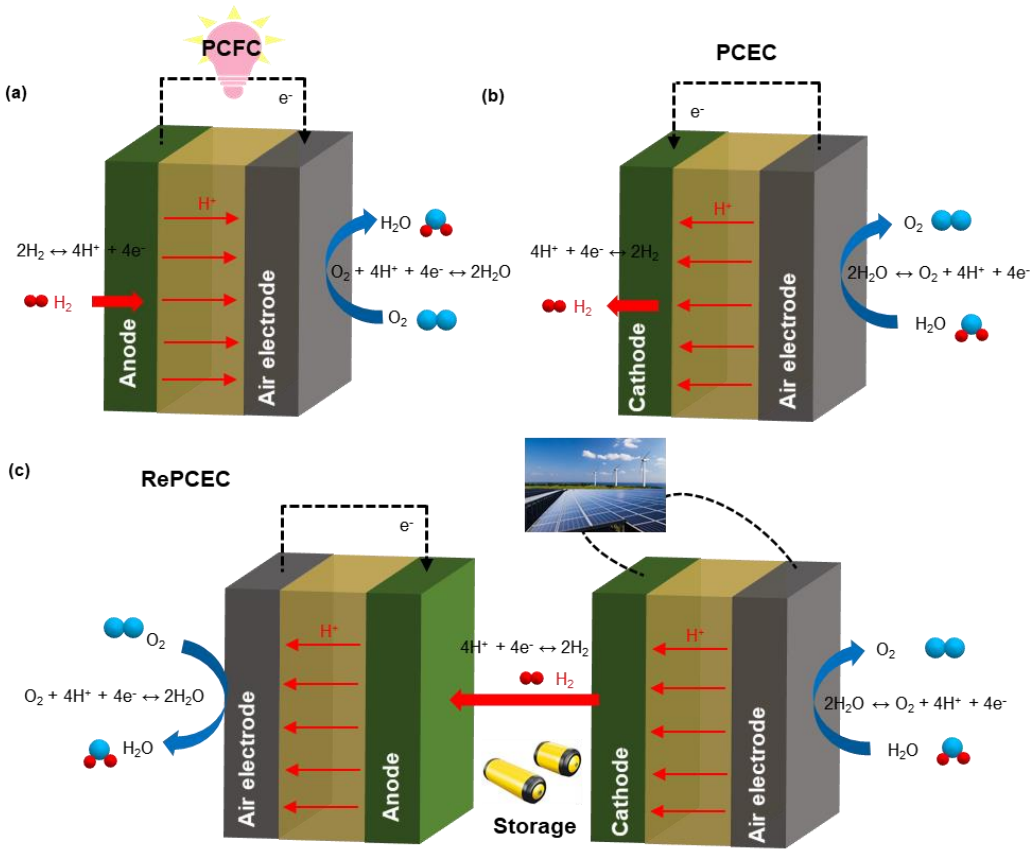


Figure 1-3 Operation mechanism of (a) proton-conducting fuel cells (PCFCs), (b) protonic ceramic electrolysis cells (PCECs), and (c) reversible protonic ceramic electrochemical cells (RePCECs).

### 1-3 Protonic ceramic fuel cells

The first page of the PCFCs was opened in 1964 with the discovery the proton conduction of $LaAlO_3$ by French scientist Francis Forrat.[29] In 1982, proton-conducting oxides, $SrCe_{1-x}M_xO_3$ (M=Sc, Yb), were applied to fuel cells.[30] In the 90s, highly proton conducting ceramic acceptor-doped Ba(Zr, Ce)$O_3$ were discovered.[31-33] In the following years, the PCFCs faced the challenge of poor sinterability, and thus received relatively little attention until the important process breakthrough on sinterability in 2007. Babilo *et al*. and Yamazaki *et al*. pioneered the use of a ZnO sintering aid to enhance densification and dramatically lowered the required sintering temperatures.[34,35] Since then, a growing body of research has focused on further enhancing sintering of protonic ceramics by adding various sintering aids, including ZnO, NiO, CuO, and CoO.[36-38]

In 2015, Duan *et al.* first reported a modified sintering-aid-assisted synthesis processes to fabricate lab-scale high performance PCFCs based on $BaZr_{0.1}Ce_{0.7}Y_{0.1}Yb_{0.1}O_3$ (BZCYYb1711) electrolyte and demonstrated excellent performance (650 mW $cm^{-2}$ at 600 ℃) and long-term stability with both hydrogen and methane fuels.[24] This work reaffirmed the feasibility of intermediate-temperature PCFCs. In 2018, Ann *et al.* demonstrated the world record power density of PCFCs with $BaCe_{0.55}Zr_{0.3}Y_{0.15}O_{3-\delta}$ electrolyte (1.302 W $cm^{-2}$ at 600 ℃).[39] In the same year, Choi *et al*. demonstrated high performance of $BaCe_{0.4}Zr_{0.4}Y_{0.1}Yb_{0.1}O_3$ (BCZYYb4411)-based PCFCs designed with an air electrode functional layer, and achieved the champion data of the peak power density (PPD) equaling to 0.548 W $cm^{-2}$ at 500 ℃.[40] Bae *et al*. reported the power output of 1.10 W $cm^{-2}$ at 600 ℃ for the cell based on $BaCe_{0.55}Zr_{0.3}Y_{0.15}O_{3-\delta}$.[41] In 2019, Song *et al* reported the PPD of 743 mW$cm^{-2}$ for BZCYYb4411 base PCFC at 600 ℃.[42] In the same year, Zhou *et al.* found a cell with a thin-film $BaZr_{0.1}Ce_{0.7}Y_{0.1}Yb_{0.1}O_3$ (BZCYYb1711) electrolyte delivered the PPD of 732 mW $cm^{-2}$, at 600 ℃.[43] In addition, Xia *et al.* reported that the single cells with $BaZr_{0.1}Ce_{0.7}Y_{0.2}O_3$ (BZCY172) electrolytes reached to 841 mW $cm^2$ at 600 ℃.[44] All the

mentioned PPDs are listed in Table 1-1. In conclusion, those excellent performances indicate that PCFCs are promising for intermediate temperature next generation fuel cells.

Table 1-1 Summary of peak power densities of PCFCs at 600 °C.

| Electrolytes | Air electrodes | Power densities (W $cm^{-2}$) | Ref |
|---|---|---|---|
| BZCY442 | BCCY | 0.40 | 42 |
| BZCY172 | BFSB3 | 0.84 | 44 |
| BZCYYb4411 | BCFZY | 0.648 | 24 |
| BZCYYb4411 | PBSCF | 1.065 | 40 |
| BZCYYb4411 | BCCY | 0.74 | 42 |
| BZCYYb4411 | PBSCF | 0.82 | 17 |
| BZCYYb4411 | LSCF | 0.42 | 17 |
| BZCYYb4411 | LSM73 | 0.37 | 17 |
| BZCYYb1711 | SSNCF | 0.73 | 43 |
| BZCYYb1711 | NBSCF | 0.69 | 46 |
| BZCYYb4411 | PNC | 0.53 | 45 |

For electrolytes: BZCY442 = $BaZr_{0.4}Ce_{0.4}Y_{0.2}O_3$; BZCY172 = $BaZr_{0.1}Ce_{0.7}Y_{0.2}O_3$; BZCYYb4411 = $BaZr_{0.4}Ce_{0.4}Y_{0.1}Yb_{0.1}O_3$; BZCYYb1711 = $BaZr_{0.1}Ce_{0.7}Y_{0.1}Yb_{0.1}O_3$;

For air electrodes: BCCY = $BaCo_{0.7}(Ce_{0.8}Y_{0.2})_{0.3}O_{3-\delta}$; BFSB3=$BaFe_{0.5}Sn_{0.2}Bi_{0.3}O_{3-\delta}$; BCFZY = $BaCo_{0.4}Fe_{0.4}Zr_{0.1}Y_{0.1}O_{3-\delta}$; PBSCF = $PrBa_{0.5}Sr_{0.5}Co_{1.5}Fe_{0.5}O_{5+\delta}$; SSNCF = $Sr_2Sc_{0.1}Nb_{0.1}Co_{1.5}Fe_{0.3}O_{6-\delta}$; NBSCF = $NdBa_{0.5}Sr_{0.5}Co_{1.5}Fe_{0.5}O_{5+\delta}$; LSCF = $La_{0.6}Sr_{0.4}Co_{0.2}Fe_{0.8}O_3$; LSM73= $La_{0.7}Sr_{0.3}MnO_3$; PNC = $PrNi_{0.5}Co_{0.5}O_3$.

### 1-4 Protonic ceramic electrolysis cells

In addition to electricity generation, protonic ceramic cells in electrolysis mode, the reversible version of an PCFC, can be used to convert electricity and water/carbon dioxide to hydrogen and/or carbon monoxide, or even other fuels by chemical electrolysis. The PCEC was firstly demonstrated by Iwahara *et al.* for the electrolysis of steam in 1982.[47] After several dozens of years development, several groups developed the PCECs with high electrolysis efficiency. Choi *et al.* demonstrated the cells with BZCYYb4411 electrolyte reached to the current density of 1920 mA $cm^{-2}$ at thermal neutral point (1.3V) at 600 ℃,[17] however, most of them are limited to 0.8 A $cm^{-2}$ at 1.3 V as shown in Table 1-2.

Table 1-2 Current densities at 1.3 V for PCECs at 600 ℃.

| Electrolytes | Air electrodes | Current densities (A $cm^{-2}$) | Ref |
|---|---|---|---|
| BZCY442 | SSC | 0.01 | 48 |
| BZY91 | LSCF-BZY82 | 0.05 | 49 |
| BZY82 | SFM-BZY | 0.21 | 50 |
| BZCY532 | SEFC-BZCY53 | 0.42 | 51 |
| BZCYYb4411 | LSM73 | 0.65 | 17 |
| BZCYYb4411 | LSCF | 0.70 | 17 |
| BZCYYb1711 | NBSCF-BZCYYb | 0.75 | 52 |
| BZCYYb1711 | PBSCF | 0.85 | 53 |
| BZCYYb4411 | PBSCF | 1.42 | 17 |
| $BZCYYb4411^{(PLD)}$ | PBSCF | 1.92 | 17 |

For electrolytes: BZCY442 = $BaZr_{0.4}Ce_{0.4}Y_{0.2}O_3$; BZY91 = $BaZr_{0.9}Y_{0.1}O_3$; BZY82 = $BaZr_{0.8}Y_{0.2}O_3$; BZCY352 = $BaZr_{0.3}Ce_{0.5}Y_{0.2}O_3$; BZCYYb4411 = $BaZr_{0.4}Ce_{0.4}Y_{0.1}Yb_{0.1}O_3$; BZCYYb1711 = $BaZr_{0.1}Ce_{0.7}Y_{0.1}Yb_{0.1}O_3$;

For air electrode: SSC = $Sm_{0.5}Sr_{0.5}CoO_3$; LSCF = $La_{0.6}Sr_{0.4}Co_{0.2}Fe_{0.8}O_3$; SFM = $Sr_2Fe_{1.5}Mo_{0.5}O_6$; SEFC = $SrEu_2Fe_{1.8}Co_{0.2}O_7$; LSM73 = $La_{0.7}Sr_{0.3}MnO_3$. PBSCF = $PrBa_{0.5}Sr_{0.5}Co_{1.5}Fe_{0.5}O_{5+\delta}$;

## 1-5 Reversible protonic ceramic electrochemical cells

Protonic ceramic cells have also been explored for energy storage when their applications are reversible protonic ceramic electrochemical cells (RePCECs), which combine the functions of PCFCs and PCECs, but greater than them. They are relatively new, hence, there are not so many researches on RePCECs. In 2017, Yang *et al.* reported that RePCECs with $BaCe_{0.5}Zr_{0.2}In_{0.3}O_3$ membrane as an electrolyte displays a power density of 151 mW $cm^{-2}$ at 700 °C in fuel cell (SOFC) mode, and manifest the current density of 729 mA $cm^{-2}$ at 700 °C with an applied voltage of 1.5 V;[54] RePCECs with BZCY53 electrolyte obtained the PPD of ~200 mW $cm^{-2}$ in fuel cell mode, and ~500 mA $cm^{-2}$ @ 1.3V in electrolysis mode at 600 °C with air electrode $SrEu_2Fe_{1.8}Co_{0.2}O_{7-\delta}$ (SEFC).[51] RePCEC based on BZCYYb1711 electrolyte with $La_{1.2}Sr_{0.8}NiO_{4-\delta}$ (LSN) air electrode exhibits maximum current density of 420 mA $cm^{-2}$ at 1.3 V in electrolysis mode, and PPD of 223 mW $cm^{-2}$, respectively, at 600 °C reported by Yang *et al.*.[55] In the same year, the same group developed $Ln_{1.2}Sr_{0.8}NiO_4$ as the air electrode of RePCEC, the electrochemical performance was still limited at lower intermediate temperature.[56] Furthermore, they infiltrated $La_{1.2}Sr_{0.8}NiO_{4-\delta}$ (LSN) into $BaCe_{0.68}Zr_{0.1}Y_{0.1}Yb_{0.1}Cu_{0.02}O_{3-\delta}$ (BCZYYC2) to make the composite air electrode, improved the electrical performance to 540 mW $cm^{-2}$, 1040 mA $cm^{-2}$, respectively, at 600 °C.[57] These researches are unsatisfied until the following RePCECs are reported. In 2019, Duan *et al.* demonstrated RePCECs for seasonal energy storage, while Choi and co-workers demonstrated RePCECs with excellent reversibility cells with BZCYYb4411 electrolyte and PBSCF air electrode yield a remarkable current density of 1920 mA $cm^{-2}$, and PPD of 1070 mW $cm^{-2}$ at 600 °C.[16,17] These works present a new hydrogen production scenario, which could facilitate cost reduction of large-scale hydrogen production and bodes well for the massive deployment of hydrogen energy integrated with renewable power plants.

## 1-6 The issue of protonic ceramic fuel cells

Hereafter, this thesis focuses on the PCFCs even though the contents are also related to PCECs and REPCFCs. Although several groups have developed thin-film PCFCs with very high power output (PPD > 1.0 W $cm^{-2}$; current density at 1.3 V > 0.8 A $cm^{-2}$) at 600 ℃ as already mentioned above,[16,17,39-41] the power generation performance rapidly deteriorates with further reduction of the operating temperature. Hence the champion data of PPD at 500 °C is 0.548 W $cm^{-2}$.[39] This is much lower than the values predicted from ohmic resistance of the current PCFC electrolytes with 10 μm thickness, which are ranged from 0.2 to 1.6 W $cm^{-2}$ with increasing temperatures from 350 to 600 ℃.[24]

One of the reasons for the deteriorated performances is the increase of electrolyte resistivity, especially at temperatures below 500 ℃. To the best of our knowledge, the vast majority of high power-output PCFCs is achieved with Ce-rich side of acceptor dope Ba(Zr, Ce)$O_3$ solid solutions, such as $BaZr_{0.1}Ce_{0.7}Y_{0.2-x}Yb_xO_3$ ($x$ = 0 or 0.1) or $BaZr_{0.4}Ce_{0.4}Y_{0.2-x}Yb_xO_3$ ($x$ = 0 or 0.1). For instances, Choi *et al.* reported that the ohmic resistance of 15 μm-thick BZCYYb4411 film is 0.5 Ω $cm^2$ at 500 ℃ under fuel cell condition.[40] Nien *et al*. reported that an ohmic resistance (ASR) of ~18 μm-thick BZCY172 film is 0.45 Ω $cm^2$ in the similar condition.[58] and An *et al.* reported that the ohmic resistance of 5 μm-thick $BaCe_{0.55}Zr_{0.3}Y_{0.15}O_{3-\delta}$ (BCZY3) film reached to 0.17 Ω $cm^2$ which is the champion data of the ceramic electrolyte membranes.[39] These ohmic resistances are still larger than the value expected from the bulk conductivity by about one order of magnitude.[17]

Another critical issue is the lack of air electrode materials especially designed for protonic ceramic cells. Mixed $O^{2-}/e^-$ double conductors, such as $La_{0.6}Sr_{0.4}CoO_3$ (LSC64), $Sm_{0.5}Sr_{0.5}CoO_3$ (SSC55), $La_{0.6}Sr_{0.4}Co_{0.2}Fe_{0.8}O_3$ (LSCF6428) and $Ba_{0.5}Sr_{0.5}Co_{0.2}Fe_{0.8}O_3$ (BSCF5528) are practically-feasible air electrodes for SOFCs.

Because their bulk oxide ion conductivities allow fast transfer of oxide ions from air electrode to electrolyte via surface and bulk diffusion, the reaction areas do not limit within the gas-electrode-electrolyte triple phase boundary (TPB) and thus, are extended to overall the surface of the double conducting oxides. (Figure 1-4a).[59]

However, these double conductors are not suitable for the air electrode of PCFCs due to the mismatch of the ion carrier with electrode and electrolyte. In case of PCFCs, protons are needed to translate from electrolyte to air electrode surface for the water formation, so that the reaction area is limited to the TPB with a use of double conducting air electrodes (Figure 1-4b).[60-63] Hence, the PCFCs with double conducting air electrode show the large polarization resistances at the cathode, resulting in the deteriorated fuel cell performances as listed in Table 1-3. The materials having sufficient proton conductivity together with electron conductivity, if available, are expected to extend the effective reaction area to the overall surface of electrode, leading to the decrease of the polarization resistances (Figure 1-4c),[64,65] which motivates us to develop mixed $O^{2-}/H^{+}/e^{-}$ triple conducting materials for the air electrode of PCFCs.

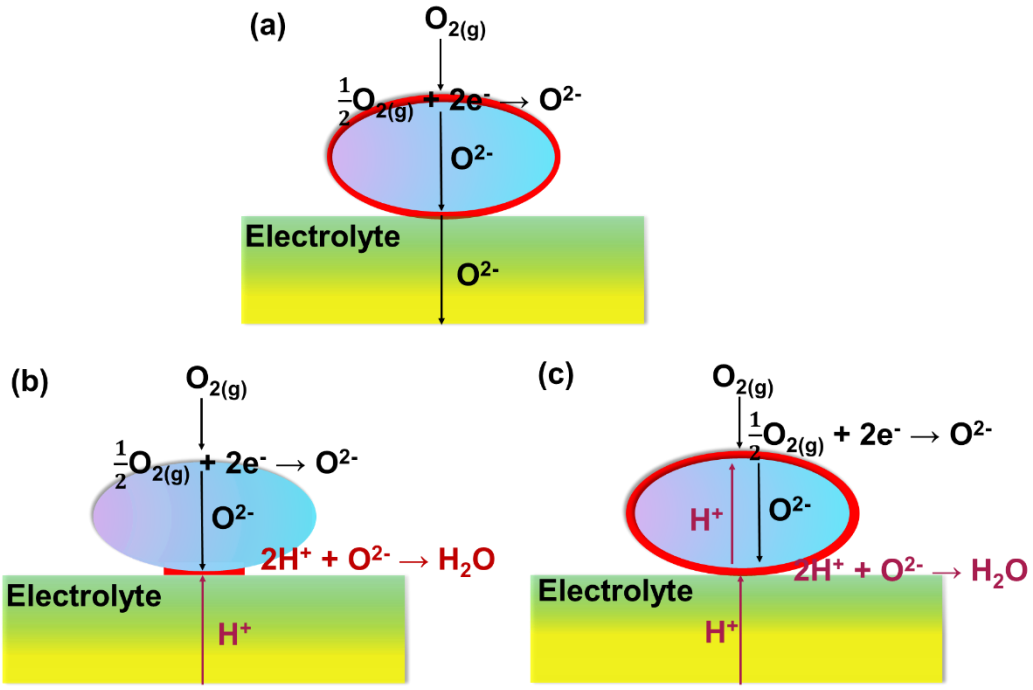


Figure 1-4 The scheme of effective reaction areas (a) air electrode reaction area of oxide-ion conducting cell with double conductor, (b) protonic ceramic cells with double conductor, and (c) mixed $O^{2-}/H^+/e^-$ triple-conducting air electrodes.

Table 1-3 List of electrochemical performances at 600 ℃ of the PCFCs with various $O^{2-}/e^{-}$ double conductors as air electrodes.

| Electrolytes | Air electrodes | PPD (mW $cm^{-2}$) | $R_p$ (Ω $cm^2$) | Ref |
|---|---|---|---|---|
| BZCY442 | BSCF | 276 | 0.74 | 66 |
| BZCY442 | BSCF | 161 | 0.18 | 67 |
| BZCY442 | LSCF | 279 | 0.71 | 68 |
| BZCY622 | LSCF | 336 | 0.58 | 68 |
| BZCY712 | LSCF | 111 | 1.34 | 68 |
| BZY15 | LSC64 | 720 | 0.15 | 69 |
| BZCY721 | LC | - | 0.14 | 70 |
| BCY91 | BSCF | - | 1.5 | 71 |
| BCSm82 | SSC | 225 | 0.21 | 72 |
| BZCY442 | $Pr_2NiO_4$ | 102 | 0.77 | 73 |
| BZYbCu | LSM6530 | 51 | 0.55 | 74 |
| BCY85 | LSM82 | 80 | 7.3 | 75 |

For electrolytes: BZCY442 = $BaZr_{0.4}Ce_{0.4}Y_{0.2}O_3$; BZCY622 = $BaZr_{0.6}Ce_{0.2}Y_{0.2}O_3$; BZCY712 = $BaZr_{0.7}Ce_{0.1}Y_{0.2}O_3$; BZY15 = $BaZr_{0.85}Y_{0.15}O_3$; BZCY721 = $BaZr_{0.7}Ce_{0.2}Y_{0.1}O_3$; BCY91 = $BaCe_{0.9}Y_{0.1}O_3$; BCSm82 = $BaCe_{0.8}Sm_{0.2}O_{2.9}$; BZYbCu = $Ba(Zr_{0.84}Yb_{0.15}Cu_{0.01})O_3$; BZY85 = $BaZr_{0.15}Y_{0.85}O_3$;

For air electrodes: BSCF = $Ba_{0.5}Sr_{0.5}Co_{0.5}Fe_{0.5}O_{3-\delta}$; $La_{0.6}Sr_{0.4}Co_{0.2}Fe_{0.8}O_3$ = LSCF; LSC64 = $La_{0.6}Sr_{0.4})CoO_{3-\delta}$; SSC = $Sm_{0.5}Sr_{0.5}CoO_3$; LSM6530 = $(La_{0.65}Sr_{0.3})MnO_{3-\delta}$; LSM82 = $La_{0.8}Sr_{0.2}MnO_3$.

## 1-7 Composite air electrodes

The development of $H^+/O^{2-}/e^-$ triple conducting materials must be indispensable as air electrodes of the advanced PCFCs, as mentioned above. The composites of double conductors and Ba(Zr, Ce, Y)$O_3$ electrolytes were first proposed as a such triple conducting materials, most of which are listed in Table 1-4. Yang *et al.* first reported composite air electrodes consisting of proton-conducting $BaZr_{0.1}Ce_{0.7}Y_{0.2}O_3$ (BZCY172) and mixed oxide-ion electron conducting $Sm_{0.5}Sr_{0.5}CoO_3$ (SSC) or $La_{0.6}Sr_{0.4}Co_{0.2}Fe_{0.8}O_3$ (LSCF), prepared by physical mixing of both with a subsequent high-temperature calcination.[25,76] The PPDs of the corresponding cells were 445 mW $cm^{-2}$ at 600 ℃ and 215 mW$cm^{-2}$ at 550 ℃.[25,76] Fabbri *et al.* reported that LSCF-$BaZr_{0.5}Pr_{0.3}Y_{0.2}O_3$ composite for the air electrode of PCFCs, and the PPD is relatively small with the value equaling to 128 mW $cm^{-2}$ at 650 ℃.[77] $La_{0.7}Sr_{0.3}FeO_3$ / $Ba(Ce_{0.51}Zr_{0.3}Y_{0.15}Zn_{0.04})O_3$ composite air electrode exhibited ~170 mW $cm^{-2}$ at 550 ℃.[78] A composite air electrode consisted of $BaZr_{0.1}Ce_{0.8}Y_{0.1}O_3$ (BZCY181) and SSC55 gives the power output 370 mW $cm^{-2}$ at 600 ℃.[79]

In more recent year, the $BaCe_{0.5}Zr_{0.35}Y_{0.15}O_{3-\delta}$ (BCZY53515) particles wrapped by LSCF6428 thin films were examined as a composite electrode, however, the related cells showed dissatisfactory peak power density of 239 mW $cm^{-2}$ at 550 ℃.[80] The $La_{0.5}Ba_{0.5}Co_{1/3}Mn_{1/3}Fe_{1/3}O_3$-$BaZr_{0.9}Y_{0.1}O_{2.95}$ composite prepared via oxidation-driven exsolution method gains the moderate performance with 440 mW $cm^{-2}$ PPD at 600 ℃.[81] Song *et al.* reported that mixed $H^+/O^{2-}/e^-$ triple conducting nanocomposite comprising protonic conducting $BaCe_{0.8}Y_{0.2}O_3$ and double conductor $BaCo_{0.9}(Ce_{0.8}Y_{0.2})_{0.1}O_3$ could be prepared by micro phase separation of perovskite-type $BaCo_{0.7}(Ce_{0.8}Y_{0.2})_{0.3}O_3$ (BCCY) and the corresponding cell yielded the PPD of 319 mW $cm^{-2}$ at 500 ℃.[82] Similarly, a stable twin-perovskite nanocomposite of $BaCe_{0.4}Fe_{0.4}Co_{0.2}O_3$ was synthesized by a one-pot Pechiney synthesis method in 2020, however, its electrochemical performance was rather limited (237 mW $cm^{-2}$, 0.26 Ω $cm^2$ at

600 ℃).[83]

In addition to the above mentioned, there are numerous reports for the PCFCs with composite air electrodes, as shown in Table 1-4. Most of them involved large polarization resistances of more than 0.3 Ω $cm^2$ and gained less than 400 mW $cm^{-2}$ in PPDs even at 600 ℃. These poor performances of the composite air electrodes imply that inhomogeneous triple conductors cannot extend the reaction area (Figure 1-5a), attributed to the small contact area between double conductors and proton conductors due to the inhomogeneity of the mixing and so on. Therefore, the single-phase oxides with mixed $H^+/O^{2-}/e^-$ triple conductivity, *i.e.* 'true' $H^+/O^{2-}/e^-$ triple conductor must be desirable for high efficiency protonic ceramic cells, whose reaction area is expected to be the overall surface of air electrodes particles (Figure 1-5b).

Table 1-4 Comparison of electrical performances of the protonic ceramic fuel cells with composite air electrodes at 600 ℃.

| Electrolytes | Air electrodes | PPDs (mW $cm^{-2}$) | $R_p$($\Omega$ $cm^2$) | Ref |
|---|---|---|---|---|
| BZCY172 | BZCY172–SSC | 445 | 0.17 | 25 |
| BZCY172 | BZCY172–LSCF | - | 0.47 | 76 |
| BZPY712 | BZPY532–LSCF | - | 0.16 | 77 |
| BZCYZn | BZCYZn–LSF73 | 270 | 0.35 | 78 |
| BZCY181 | BZCY181–SSC | 370 | 0.42 | 79 |
| BZCY172 | BZCY172–BSCF | 270 | 0.56 | 84 |
| BCZY172 | BCZY172–SSC | 350 | 0.35 | 85 |
| BZCY172 | BZCY172–GBSC | 255 | 0.39 | 86 |
| BZCY172 | BZCY172–BSPCu | 190 | 0.71 | 87 |
| BZCY172 | BZCY172–SSC | 170 | 0.71 | 88 |
| BZCY442 | BZCY442–NBFNi | 270 | 0.62 | 89 |
| BZCY442 | BZCY442–NBFNb | 215 | 0.82 | 90 |
| BZCY53515 | BZCY53515–LSCF | 324 | 0.77 | 80 |
| BZY91 | BZY91–LBCMF | - | 0.44 | 81 |
| BZY91 | BZ–LBC | - | 1.54 | 91 |
| BZCY442 | BZCY–BSCFT | 190 | 0.91 | 92 |
| BZCY352 | BZCY352–SF | 370 | 0.35 | 60 |
| BZCY442 | BCCY | 400 | 0.16 | 42 |
| BZCYYb4411 | BCCY | 740 | 0.13 | 42 |
| BZCYYb1711 | BCFC442 | 237 | 0.26 | 83 |

For electrolytes: BZCY172 = $BaZr_{0.1}Ce_{0.7}Y_{0.2}O_3$; BZPY712 = $BaZr_{0.7}Pr_{0.1}Y_{0.2}O_3$; BZCYZn = $BaZr_{0.51}Ce_{0.3}Y_{0.15}Zn_{0.04}O_3$; BZCY181 = $BaZr_{0.1}Ce_{0.8}Y_{0.1}O_3$; BZCY442 = $BaZr_{0.4}Ce_{0.4}Y_{0.2}O_3$; BZCY53515 = $BaZr_{0.5}Ce_{0.35}Y_{0.15}O_3$; BZY91 = $BaZr_{0.9}Y_{0.1}O_3$; BZCY352 = $BaZr_{0.3}Ce_{0.5}Y_{0.2}O_3$; BZCYYb4411 = $BaZr_{0.4}Ce_{0.4}Y_{0.1}Yb_{0.1}O_3$; BZCYYb1711 = $BaZr_{0.1}Ce_{0.7}Y_{0.1}Yb_{0.1}O_3$;

For air electrodes: SSC = $Sm_{0.5}Sr_{0.5}CoO_3$; LSCF = $La_{0.6}Sr_{0.4}Co_{0.2}Fe_{0.8}O_3$; LSCF = $La_{0.6}Sr_{0.4}Co_{0.2}Fe_{0.8}O_3$; LSF73 = $La_{0.7}Sr_{0.3}FeO_3$; SSC = $Sm_{0.5}Sr_{0.5}CoO_3$; BSCF = $Ba_{0.5}Sr_{0.5}Co_{0.5}Fe_{0.5}O_{3-\delta}$; GBSC= $GdBa_{0.5}Sr_{0.5}Co_2O_5$; BSPCu = $Ba_{0.5}Sr_{0.5}Fe_{0.8}Cu_{0.2}O_3$; NBFNi = $Nd_{0.5}Ba_{0.5}Fe_{1-x}Ni_xO_3$; NBFNb = $NdBaFe_{1.9}Nb_{0.1}O_5$; LBCMF = $La_{0.5}Ba_{0.5}Co_{1/3}Mn_{1/3}Fe_{1/3}O_3$; BZ–LBC = $La_{0.5}Ba_{0.5}CoO_3$–$BaZrO_3$; BSCFT= $Ba_{0.5}Sr_{0.5}(Co_{0.8}Fe_{0.2})_{0.9}Ti_{0.1}O_3$; SF= $Sr_3Fe_2O_7$; BCCY= = $BaCo_{0.7}(Ce_{0.8}Y_{0.2})_{0.3}O_{3-\delta}$; BCFC442= $BaCe_{0.4}Fe_{0.4}Co_{0.2}O_3$.

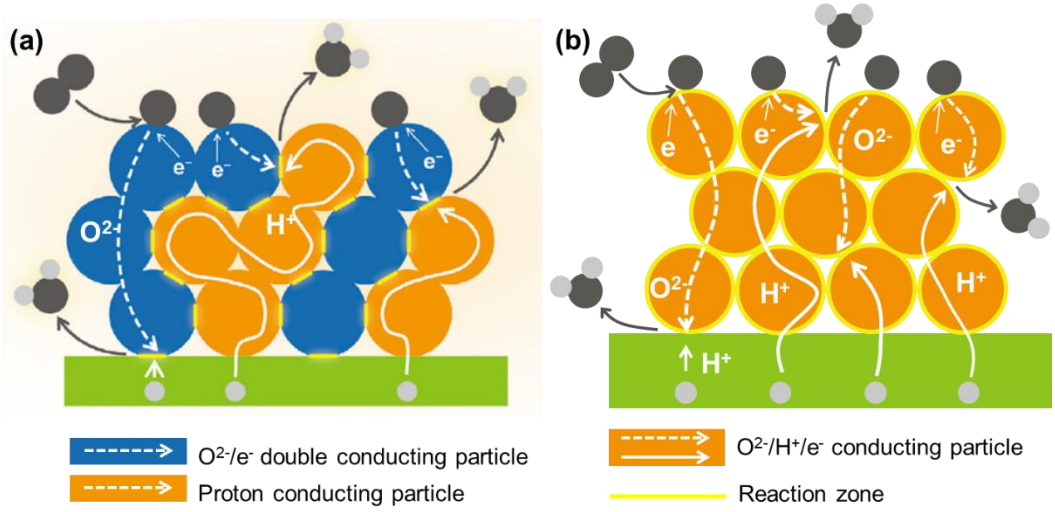


Figure 1-5 The scheme of effective reaction areas of (a) composite air electrode (Song et al., Joule, 2019, 3, 1–12), and (b) single-phase triple air electrode.

### 1-8 Mixed $H^+/O^{2-}/e^-$ triple conductors as advanced electrode materials

It has been demonstrated that the single-phase $H^+/O^{2-}/e^-$ triple conductors exhibit excellent performances as an air electrode of PCFCs (Table 1-5). Duan *et al*. first reports the triple conductor $BaCo_{0.4}Fe_{0.4}Zr_{0.1}Y_{0.1}O_{3-\delta}$ (BCFZY).[24] This oxide can be partially hydrated with retaining 0.019 mole fraction protons at 500 °C under $p_{H2O}$ of 0.0095 atm and the related cells reached the PPD of 405 mW $cm^{-2}$ at 500 °C.[24,93] In 2018, Choi *et al.* reported that $PrBa_{0.5}Sr_{0.5}Co_{1.5}Fe_{0.5}O_{5+\delta}$ (PBSCF) can be hydrated, thereby exhibiting triple $O^{2-}/H^+/e^-$ conductivity, and the cells yielded PPD of more than 500 mW $cm^{-2}$ at 500 °C, although the proton concentration abruptly decreases from 0.035 mole fraction at 200 °C to 0.017 mole fraction at 600 °C.[40] The other double perovskite type triple conductor is $Sr_2Sc_{0.1}Nb_{0.1}Co_{1.5}Fe_{0.3}O_6$ (SSNCF) which gains the peak power density of 405 mW $cm^{-2}$ at 500 ℃ with $BaZr_{0.1}Ce_{0.7}Y_{0.1}Yb_{0.1}O_3$ electrolytes.[43] $BaFe_{0.5}Sn_{0.2}Bi_{0.3}O_3$ (BFSBi3) is a new type of Co-free triple conductors, gaining PPD of 426 mW $cm^{-2}$ at 500 ℃ with BZCY172 based cells.[44] Based on these references, developing single-phase mixed $H^+/O^{2-}/e^-$ triple conductors are more powerful approach for lowering the polarization resistances of protonic ceramic cells than the composite electrodes.

Table 1-5. Comparison of electrochemical performances of the protonic ceramic fuel cells with mixed $H^+/O^{2-}/e^-$ triple air electrodes at 600 ℃.

| Electrolytes | Air electrodes | PPDs (mW $cm^{-2}$) | $R_p$(Ω $cm^2$) | Ref |
|---|---|---|---|---|
| BZCYYb1711 | SSNCF | 730 | 0.30 | 43 |
| BZCYYb1711 | NBSCF | 690 | 0.28 | 46 |
| BZCYYb4411 | PBSCF | 1065 | 0.14 | 40 |
| BZCYYb4411 | PBSCF | 820 | 0.15 | 17 |
| BZCYYb4411 | BCFZY | 648 | 0.08 | 24 |
| BZCY172 | BFSB3 | 840 | 0.09 | 44 |

For electrolytes: BZCYYb1711 = $BaZr_{0.1}Ce_{0.7}Y_{0.1}Yb_{0.1}O_3$; BZCYYb4411 = $BaZr_{0.4}Ce_{0.4}Y_{0.1}Yb_{0.1}O_3$; BZCY172 = $BaZr_{0.1}Ce_{0.7}Y_{0.2}O_3$;

For air electrodes: SSNCF = $Sr_2Sc_{0.1}Nb_{0.1}Co_{1.5}Fe_{0.3}O_{6-\delta}$; NBSCF = $NdBa_{0.5}Sr_{0.5}Co_{1.5}Fe_{0.5}O_{5+\delta}$; PBSCF = $PrBa_{0.5}Sr_{0.5}Co_{1.5}Fe_{0.5}O_{5+\delta}$; BCFZY = $BaCo_{0.4}Fe_{0.4}Zr_{0.1}Y_{0.1}O_{3-\delta}$; BFSB3=$BaFe_{0.5}Sn_{0.2}Bi_{0.3}O_{3-\delta}$;

## 1-9 Objective of this thesis

As mentioned before, developing single-phase mixed $H^+/O^{2-}/e^-$ triple conductors is promising way to improve the efficiency of PCFCs at relatively low temperatures. Normally, the formation of proton defects in oxides is conducted via hydration, driven by association between oxygen vacancies and water molecules (Equation 1-1).

$$O_O^X + V_O^{\bullet\bullet} + H_2O_{(g)} \leftrightarrow 2OH_O^{\bullet} \quad (1\text{-}1)$$

Thereby, the oxides which are capable of bulk hydration at intermediate temperatures are attractive candidates for the $H^+/O^{2-}/e^-$ triple conducting air electrodes. In most cases, the hydration enthalpies of transition metal oxides are negative,[94-96] so that the proton defect concentration tends to decrease with temperature. Unfortunately, the hydration degree of the available triple conductors is still limited and the mole fractions of protons are much lower than the values of typical proton conductor Ba(Zr, Ce, Y)$O_{3-\delta}$ (~0.1 mole fraction) even at relatively low temperatures. In fact, the cathode polarization resistances of the PCFCs with the current triple conductors are not significantly small (see Table 1-5), which implies that the proton conductivity of the most triple conductors is relatively low probably due to the lowered proton concentrations at the device operation temperatures, typically above 500 °C.

The thermogravimetry (TG) a powerful tool to characterize the hydration of oxides at elevated temperatures under controlled atmosphere. The molar fractions of hydroxide ions, i.e. protons, which is defined as $[OH_O^{\bullet}]$ were less than 0.0026 mole fraction for $La_{0.6}Sr_{0.4}Co_{1-y}Fe_yO_{3-\delta}$ under the partial water pressure ($p_{H2O}$) of 0.005 atm at 300 ℃, and that of $La_{1-x}Sr_xCoO_3$ samples were less than 0.003 mole fraction in the same conditions.[97] $BaCo_{0.4}Fe_{0.4}Zr_{0.1}Y_{0.1}O_{3-\delta}$ (BCFZY) has been reported to take 0.019 mole fraction of protons at 500 °C under the partial water pressure ($p_{H2O}$) of 0.01 atm by hydration.[24] It was demonstrated that double perovskite-type $PrBa_{0.5}Sr_{0.5}Co_{1.5}Fe_{0.5}O_{5+\delta}$ (PBSCF) favors to take proton defects equaling to 0.017 mole fraction at 600 ℃.[40]

Zohourian *et al*. conducted systematic studies for the hydration of (Ba, Sr, La)(Fe, Co, Zn, Zr, Y)$O_{3-\delta}$ perovskites by means of TG.[95] $(Ba_{0.95}La_{0.05})(Fe_{0.8}Zn_{0.2})O_{3-\delta}$ and $(Ba_{0.5}Sr_{0.5})(Sn_{0.8}Zn_{0.2})O_{3-\delta}$ show the highest proton defect concentrations among those families with equaling 0.1 and 0.063 mole fraction, respectively, at 250 °C in $p_{H2O}$ = 0.01 atm (see Figure 1-6).[95]

As aforementioned, the proton concentrations of the current triple conductors are remarkably lower than those of the well-known pure proton conductors, such as $BaCe_{0.9}Y_{0.1}O_3$, and $BaZr_{0.9}Y_{0.1}O_3$, which retain protons of 0.1 and 0.08 mole fraction at 600 °C in wet $N_2$ atmosphere ($p_{H2O}$ = 0.023 atm), respectively.[32,98] Hence it is a great challenge for materials chemists to design $H^+/O^{2-}/e^-$ triple conductors with pronounced bulk hydration ability at higher temperatures as much as proton-conducting electrolytes. The main objective of this thesis is to explore perovskite type oxides with high hydration capability at intermediate temperatures, and figure out the hydration mechanism to lead a general guideline for designing $H^+/O^{2-}/e^-$ triple conductors. Finally, the excellent cell performances are demonstrated for the PCFCs and PCECs applied with such mixed $H^+/O^{2-}/e^-$ triple conductors.

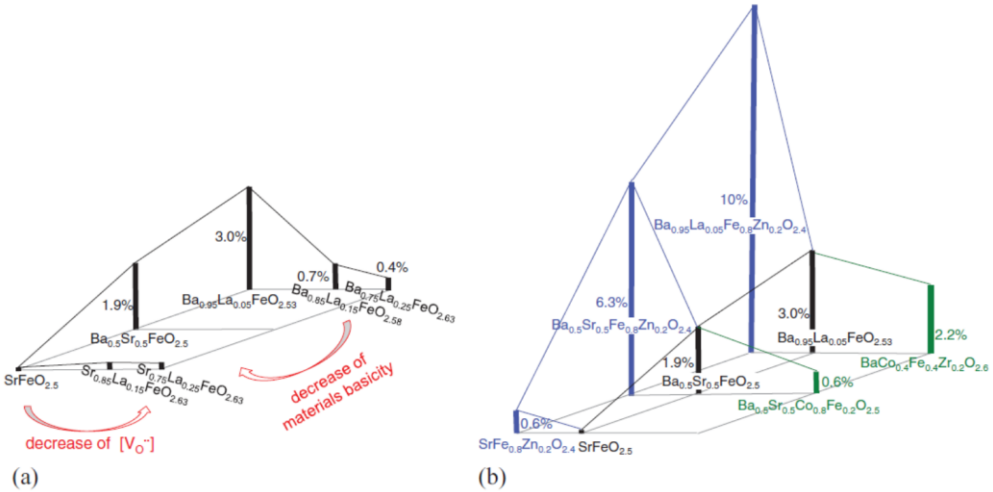


Figure 1-6 Proton concentration for (Ba, Sr, La)(Fe, Co, Zn, Zr, Y)$O_{3-\delta}$ perovskites at 250 °C in ≈16 mbar $H_2O$.[95]

## 1-10 Contents of this thesis

This thesis consists of 6 chapters as follows.

In chapter 1, the general background of SOFCs and the development of protonic ceramic cells are firstly given. Then the progresses on PCFCs, PCECs and RePCECs are generalized for the comprehensive understanding of protonic ceramic cells. Finally, the issue of protonic ceramic cells is analyzed and the corresponding solutions are proposed.

Chapter 2 gives an explanation for the general experiments used in this thesis.

Chapter 3 demonstrates the hydration capability of $La_{0.8}Sr_{0.2}Co_{1-x}Ni_xO_{3-\delta}$ (LSCN, $x$=0-0.3) in wet air condition at intermediate temperatures and sufficiently high performances of the related PCFCs and PCECs. LSCN oxides can capture bulk proton carriers in the concentration range of 0.06-0.15 mole fractions by the defect association mechanism at around 400°C. The cells with LSCN air electrodes exhibit superior electrochemical performances to the cells with conventional double conducting air electrodes in both FC and EC mode, achieving the current densities of 1.09 A $cm^{-2}$ at 1.3 V in EC mode and PPD of 0.91 W $cm^{-2}$ in FC mode at 600 ℃. The polarization resistance of LSCN was reduced to 0.09 Ω $cm^{-2}$ at 600 ℃.

In chapter 4, the massive uptake of proton carriers in cubic perovskite type $La_{0.7}Sr_{0.3}MnO_{3-\delta}$ at intermediate temperatures has been demonstrated. The thermochemical hydration reaction is not carried out by a simple association mechanism (Equation 1-1) and mediated via the charge disproportionation between oxygen and manganese atoms. $La_{0.7}Sr_{0.3}MnO_{3-\delta}$ undergoes decline of antibonding O *2p* states hybridized with Mn *3d* orbitals together with oxidation of $Mn^{3+}$ to $Mn^{4+}$ through the hydration and thus retains bulk protons in the concentrations of 0.14 in wet air at around 415 ℃. The current results offer a general concept to design triple conductors operating in air condition, namely, that transition metal oxides possessing many oxygen

vacancies and oxygen hole carriers could be promising candidates.

In chapter 5, cubic-type $La_{0.7}Sr_{0.3}Mn_{0.7}Ni_{0.3}O_{3-\delta}$ (C-LSMN7373) perovskite is promising for intermediate-temperature protonic ceramic fuel cells (PCFCs) because of the sufficient $H^+$/ $O^{2-}$/$e^-$ triple conductivity. The oxide can be hydrated by gaining 0.1 mole fraction $H_2O$ under wet air at 415 ℃, as confirmed by thermogravimetry analysis. However, rhombohedral-type $La_{0.7}Sr_{0.3}Mn_{1-x}Ni_xO_{3-\delta}$ cannot undergo hydration because the oxygen vacancy concentration required for water association is lower than the cubic phase concentration. The air electrode performances of various PCFCs are examined by fabricating thin-film cells based on a $Ba(Zr_{0.4}Ce_{0.4}Y_{0.2})O_3$ electrolyte. The peak power density of the PCFCs with cubic-type LSMN7373 air electrode is 386 mW $cm^{-2}$ at 600 ℃, which is much higher than the reported values for the Zr-rich side electrolytes. Moreover, the cathodic polarization resistance is lower than that of the cell with the widely used $La_{0.6}Sr_{0.4}Co_{0.2}Fe_{0.8}O_3$ air electrode below 550 ℃.

In chapter 6, the overall summary and conclusion of this thesis are presented.

## 1-11 References


1. N. Mebarki, T. Rekioua, Z. Mokrani, D. Rekioua and S. Bacha, *International Journal of Hydrogen Energy*, 2016, **41**, 20993-21005.
2. T. Ioroi, Z. Siroma, S. I. Yamazaki and K. Yasuda, *Advanced Energy Materials*, 2018, **9**, 1801284.
3. Y. Wang, D. F. Ruiz Diaz, K. S. Chen, Z. Wang and X. C. Adroher, *Materials Today*, 2020, **32**, 178-203.
4. R. M. Ormerod, *Chemical Society Review*, 2003, **32**, 17-28.
5. V. Dusastre and J. Kilner, *Solid state ionics*, 1999, **126**, 163-174.
6. J. Huijsmans, F. Van Berkel and G. Christie, *Journal of Power Sources*, 1998, **71**, 107-110.
7. J. M. Vohs and R. J. Gorte, *Advanced Materials*, 2009, **21**, 943-956.
8. Y. Tang, Y. Zhang, W. Li, B. Ma and X. Chen, *Chemical Society Review*, 2015, **44**, 5926-5940.
9. M. Li, J. Lu, Z. Chen and K. Amine, *Advanced Materials*, 2018, 30, 1800561.
10. A. Z. Weber, M. M. Mench, J. P. Meyers, P. N. Ross, J. T. Gostick and Q. Liu, *Journal of the Applied Electrochemistry*, 2011, **41**, 1137-1164.
11. M. Park, J. Ryu, W. Wang and J. Cho, *Nature Reviews Materials*, 2016, **2**, 1-18.
12. L. Chen, X. Dong, Y. Wang and Y. Xia, *Nature communications*, 2016, **7**, 1-8.
13. S. W. Boettcher, *Nature Catalysis*, 2018, **1**, 814-815.
14. Y. Zheng, J. Wang, B. Yu, W. Zhang, J. Chen, J. Qiao and J. Zhang, *Chemical Society Reviews*, 2017, **46**, 1427-1463.
15. C. Graves, S. D. Ebbesen, S. H. Jensen, S. B. Simonsen and M. B. Mogensen, *Nature materials*, 2015, **14**, 239-244.
16. C. Duan, R. Kee, H. Zhu, N. Sullivan, L. Zhu, L. Bian, D. Jennings and R. O'Hayre, *Nature Energy*, 2019, **4**, 230-240.
17. S. Choi, T. C. Davenport and S. M. Haile, *Energy & Environmental Science*, 2019, **12**, 206-215.
18. S. H. Jensen, C. Graves, M. Mogensen, C. Wendel, R. Braun, G. Hughes, Z. Gao and S. A. Barnett, *Energy & Environmental Science*, 2015, **8**, 2471-2479.
19. S. M. Hashemi, P. Karnakov, P. Hadikhani, E. Chinello, S. Litvinov, C. Moser, P. Koumoutsakos and D. Psaltis, *Energy & Environmental Science*, 2019, **12**, 1592-1604.
20. R. Zhu, C. Yang, M. Zhou and J. Wang, *Chemical Engineering Journal*, 2015, **260**, 427-433.
21. K. H. Sato, T. Tezuka, R. Ichinoi S. Matsumono, K. Sadakuni and K. Oyaizu, *Chemsuschem*, 2019, 13, 2443-2448.
22. Z. Hu, Z. Wu, C. Han, J. He, Z. Ni and W. Chen, *Chemical Society Review*, 2018, **47**, 3100-3128.
23. Y. Zhu, X. Luo, H. Zhi, Y. Liao, L. Xing, M. Xu, X. Liu, K. Xu and W. Li, *Journal*

*of materials chemistry A*, 2018, **6**, 10990-11004.
24. C. Duan, J. Tong, M. Shang, S. Nikodemski, M. Sanders, S. Ricote, A. Almansoori and R. O'Hayre, *Science*, 2015, **349**, 1321-1326.
25. L. Yang, C. Zuo, S. Wang, Z. Cheng and M. Liu, *Advanced Materials*, 2008, **20**, 3280-3283.
26. R. Zohourian, R. Merkle, G. Raimondi and J. Maier, *Advanced Functional Materials*, 2018, **28**, 1801241.
27. E. Fabbri, L. Bi, D. Pergolesi and E. Traversa, *Advanced Materials*, 2012, **24**, 195-208.
28. K. Zeng and D. Zhang, *Progress in Energy and Combustion Science*, 2010, **36**, 307-326.
29. F. Rosen and C. A. Nichol, *Vitamins & Hormones*, 1964, **21**, 135-214.
30. H. Iwahara, H. Uchida and N. Maeda, *Journal of Power Sources,* 1982, 7, 293-301.
31. K. Kreuer, T. Dippel, Y. M. Baikov, J. Maier, *Solid State Ionics*, 1996, **86**, 613-620.
32. K. Kreuer, *Solid State Ionics*, 1999, **125**, 285-302.
33. K. D. Kreuer, W. Münch, A. Fuchs, U. Klock and J. Maier, *Solid State Ionics*, 2001, **145**, 295-306.
34. P. Babilo, T. Uda, S. M. Haile, *Journal of Materials Research*, 2011, **22**, 1322-1330.
35. Y. Yamazaki, R. Hernandez-Sanchez and S. M. Haile, *Chemistry of Materials*, 2009, **21**, 2755-2762.
36. J. Tong, D. Clark, M. Hoban and R. O'Hayre, *Solid State Ionics*, 2010, **181**, 496-503.
37. S. Nikodemski, J. Tong and R. O'Hayre, *Solid State Ionics*, 2013, **253**, 201-210.
38. J. Tong, D. Clark, L. Bernau, M. Sanders and R. O'Hayre, *Journal of Materials Chemistry*, 2010, **20**, 6333.
39. H. An, H. W. Lee, B. K. Kim, J. W. Son, K. J. Yoon, H. Kim, D. Shin, H. I. Ji and J. H. Lee, *Nature Energy*, 2018, **3**, 870-875.
40. S. Choi, C. J. Kucharczyk, Y. Liang, X. Zhang, I. Takeuchi, H.-I. Ji and S. M. Haile, *Nature Energy*, 2018, **3**, 202-210.
41. K. Bae, D. H. Kim, H. J. Choi, J. W. Son and J. H. Shim, *Advanced Energy Materials*, 2018, **8**, 1801315.
42. Y. Song, Y. Chen, W. Wang, C. Zhou, Y. Zhong, G. Yang, W. Zhou, M. Liu and Z. Shao, *Joule*, 2019, **3**, 1-12.
43. C. Zhou, J. Sunarso, Y. Song, J. Dai, J. Zhang, B. Gu, W. Zhou and Z. Shao, *Journal of Materials Chemistry A*, 2019, **7**, 13265-13274.
44. Y. Xia, Z. Jin, H. Wang, Z. Gong, H. Lv, R. Peng, W. Liu and L. Bi, *Journal of Materials Chemistry A*, 2019, **7**, 16136-16148.
45. H. Ding, W. Wu, C. Jiang, Y. Ding, W. Bian, B. Hu, P. Singh, C. J. Orme, L. Wang, Y. Zhang and D. Ding, Nature communications, 2020, **11**, 1907.

46. J. Kim, S. Sengodan, G. Kwon, D. Ding, J. Shin, M. Liu and G. Kim, *ChemSusChem*, 2014, **7**, 2811-2815.
47. H. Iwahara, *Journal of Power Sources*, 1982, **7**, 293-301.
48. Y. Aoki, E. Tsuji, T. Motohashi, D. Kowalski and H. Habazaki, *The Journal of Physical Chemistry C*, 2018, **122**, 22301-22308.
49. L. Bi, S. P. Shafi and E. Traversa, *Journal of Materials Chemistry A*, 2015, **3**, 5815-5819.
50. L. Lei, Z. Tao, X. Wang, J. P. Lemmon and F. Chen, *Journal of Materials Chemistry A*, 2017, **5**, 22945-22951.
51. D. Huan, N. Shi, L. Zhang, W. Tan, Y. Xie, W. Wang, C. Xia, R. Peng and Y. Lu, *ACS applied materials & interfaces*, 2018, **10**, 1761-1770.
52. J. Kim, A. Jun, O. Gwon, S. Yoo, M. Liu, J. Shin, T. H. Lim and G. Kim, *Nano Energy*, 2018, **44**, 121-126.
53. W. Wu, H. Ding, Y. Zhang, Y. Ding, P. Katiyar, P. K. Majumdar, T. He and D. Ding, *Advanced science*, 2018, **5**, 1800360.
54. S. Yang, Y. Wen, S. Zhang, S. Gu, Z. Wen and X. Ye, *International Journal of Hydrogen Energy*, 2017, **42**, 28549-28558.
55. S. Yang, S. Zhang, C. Sun, X. Ye and Z. Wen, *ACS applied materials & interfaces*, 2018, **10**, 42387-42396.
56. S. Yang, Y. Wen, J. Zhang, Y. Lu, X. Ye and Z. Wen, *Electrochimica Acta*, 2018, **267**, 269-277.
57. C. Sun, S. Yang, Y. Lu, J. Wen, X. Ye and Z. Wen, *Journal of Power Sources*, 2020, **449**, 227498.
58. S. Nien, C. Hsu, C. Chang and B. Hwang, *Fuel cells*, 2011, **11**, 178-183.
59. C. Sun, R. Hui and J. Roller, *Journal of Solid State Electrochemistry*, 2009, **14**, 1125-1144.
60. Z. Wang, W. Yang, S. P. Shafi, L. Bi, Z. Wang, R. Peng, C. Xia, W. Liu and Y. Lu, *Journal of Materials Chemistry A*, 2015, **3**, 8405-8412.
61. D. Poetzsch, R. Merkle and J. Maier, *Physical Chemistry Chemical Physics*, 2014, **16**, 16446-16453.
62. A. Grimaud, F. Mauvy, J. M. Bassat, S. Fourcade, L. Rocheron, M. Marrony and J. C. Grenier, *Journal of The Electrochemical Society*, 2012, **159**, B683-B694.
63. R. Strandbakke, E. Vøllestad, S. A. Robinson, M. L. Fontaine and T. Norby, *Journal of The Electrochemical Society*, 2017, **164**, F196-F202.
64. Y. Song, W. Wang, L. Ge, X. Xu, Z. Zhang, P. S. B. Juliao, W. Zhou and Z. Shao, *Advanced science*, 2017, **4**, 1700337.
65. J. Qu, W. Wang, Y. Chen, H. Li, Y. Zhong, G. Yang, W. Zhou and Z. Shao, *ChemSusChem*, 2018, **11**, 3112-3119.
66. Y. Liu, Y. Guo, R. Ran and Z. Shao, *Journal of Membrane Science*, 2013, **437**, 189-195.
67. Y. Guo, Y. Lin, R. Ran and Z. Shao, *Journal of Power Sources*, 2009, **193**, 400-

407.
68. S. Jeong, T. Kobayashi, K. Kuroda, H. Kwon, C. Zhu, H. Habazaki and Y. Aoki, *RSC Advances*, 2018, **8**, 26309-26317.
69. K. Bae, D. Y. Jang, H. J. Choi, D. Kim, J. Hong, B. K. Kim, J. H. Lee, J. W. Son and J. H. Shim, *Nature communications*, 2017, **8**, 14553.
70. S. Ricote, N. Bonanos, F. Lenrick and R. Wallenberg, *Journal of Power Sources*, 2012, **218**, 313-319.
71. J. Dailly, S. Fourcade, A. Largeteau, F. Mauvy, J. C. Grenier and M. Marrony, *Electrochimica Acta*, 2010, **55**, 5847-5853.
72. T. Wu, Y. Zhao, R. Peng and C. Xia, *Electrochimica Acta*, 2009, **54**, 4888-4892.
73. N. Nasani, D. Ramasamy, S. Mikhalev, A. V. Kovalevsky and D. P. Fagg, *Journal of Power Sources*, 2015, **278**, 582-589.
74. J. S. Park, J. H. Lee, H. W. Lee and B. K. Kim, *ECS Transsctions*, 2009, 25, 795
75. D. K. Lim, H. N. Im, B. Singh and S. J. Song, *Journal of The Electrochemical Society*, 2015, **162**, F547-F554.
76. L. Yang, Z. Liu, S. Wang, Y. Choi, C. Zuo and M. Liu, *Journal of Power Sources*, 2010, **195**, 471-474.
77. E. Fabbri, L. Bi, D. Pergolesi and E. Traversa, *Energy & Environmental Science*, 2011, **4**, 4984-4993.
78. J. Choi, B. Kim, S. H. Song and J. S. Park, *International Journal of Hydrogen Energy*, 2016, **41**, 9619-9626.
79. J. Dailly, G. Taillades, M. Ancelin, P. Pers and M. Marrony, *Journal of Power Sources*, 2017, **361**, 221-226.
80. S. Lee, S. Park, S. Wee, H. W. Baek and D. Shin, *Solid State Ionics*, 2018, **320**, 347-352.
81. L. Rioja-Monllor, S. Ricote, C. Bernuy-Lopez, T. Grande, R. O'Hayre and M.A. Einarsrud, *Inorganics*, 2018, **6**, 83.
82. Y. Song, Y. Chen, W. Wang, C. Zhou, Y. Zhong, G. Yang, W. Zhou, M. Liu and Z. Shao, *Joule*, 2019, **3**, 1-12.
83. Z. Zhao, J. Cui, M. Zou, S. Mu, H. Huang, Y. Meng, K. He, K. S. Brinkman and J. Tong, *Journal of Power Sources*, 2020, **450**, 227609.
84. B. Lin, H. Ding, Y. Dong, S. Wang, X. Zhang, D. Fang and G. Meng, *Journal of Power Sources*, 2009, **186**, 58-61.
85. M. Liu, J. Gao, X. Liu and G. Meng, *International Journal of Hydrogen Energy*, 2011, **36**, 13741-13745.
86. H. Ding and X. Xue, *Journal of Alloys and Compounds*, 2010, **496**, 683-686.
87. L. Zhao, B. He, Y. ling, Z. Xun, R. Peng, G. Meng and X. Liu, *International Journal of Hydrogen Energy*, 2010, **35**, 3769-3774.
88. L. Yang, C. Zuo and M. Liu, *Journal of Power Sources*, 2010, **195**, 1845-1848.
89. H. Shi, Z. Ding and G. Ma, *Fuel Cells*, 2016, **16**, 258-262.
90. X. Mao, W. Wang and G. Ma, *Ceramics International*, 2015, **41**, 10276-10280.

91. L. Rioja-Monllor, C. Bernuy-Lopez, M. L. Fontaine, T. Grande and M.A. Einarsrud, *Journal of Materials Chemistry A*, 2019, **7**, 8609-8619.
92. L. Bi, E. Fabbri and E. Traversa, *Electrochemistry Communications*, 2012, **16**, 37-40.
93. R. Ren, Z. Wang, C. Xu, W. Sun, J. Qiao, D. W. Rooney and K. Sun, *Journal of Materials Chemistry A*, 2019, **7**, 18365-18372.
94. L. R. MORSS, *Chemical reviews*, 1976, **76**, 826-840.
95. R. Zohourian, R. Merkle, G. Raimondi and J. Maier, *Advanced Functional Materials*, 2018, **28**, 1801241.
96. K. D. Kreuer, *Solid State Ionics*, 1997, **97**, 1-15.
97. D. Han, Y. Okumura, Y. Nose and T. Uda, *Solid State Ionics*, 2010, **181**, 1601-1606.
98. K. D. Kreuer, *Annual Review of Materials Research*, 2003, **33**, 333-359.

# Chapter 2 General experiments

## 2-1 Synthesis of perovskite oxides

All the perovskite $La_{1-y}Sr_yMn_{1-x}Ni_xO_{3-\delta}$ (LSMN; $y$ = 0.1-0.4; $x$ = 0.0, 0.1, 0.3) and $La_{0.8}Sr_{0.2}Co_{1-x}Ni_xO_{3-\delta}$ (LSCN; $x$ = 0.0-0.3) fine powders in this thesis were synthesized via a citrate precursor route. The flow chart of synthesis procedures is shown in Figure 2-1. First, the required amounts (based on desired stoichiometry) of nitrates were completely dissolved in Milli-Q $H_2O$. Citric acid (CA; $C_6H_8O_7 \cdot H_2O$) was then added as a chelate agent in a mole ratio of CA:LSMN/LSCN = 2:1. Next, the citrate solution was heated while vigorously stirring at 60 ℃ for 2 or 3 h to evaporate $H_2O$ and promote polymerization. Thus, gelatinous products were obtained. Deep color precursors were obtained by calcination of the gel at 500 ℃ for 1 h under air, then grind them evenly by hand milling. After that, the evenly precursors were annealed in a tube furnace in oxygen atmosphere to obtain single phase powder, finally, theses powder oxides were ball milling to obtain the distributed particles.

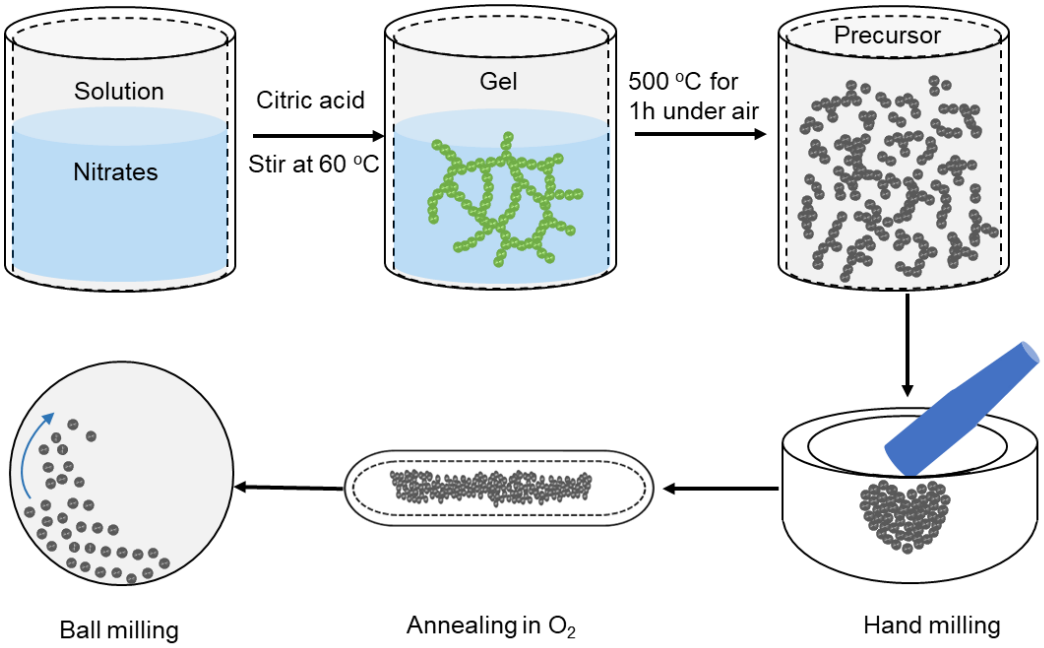


Figure 2-1 Flow chart of citrate acid method to synthesis LSMN and LSCN powders.

## 2-2 Fabrication of protonic ceramic cells

Protonic ceramic cells, including protonic conducting fuel cells (PCFCs) and electrolysis cells (PCECs) were fabricated by solid-state reactive sintering (SSRS) with a sintering aid of $Zn(NO_3)_2$, the schematic diagram for SSRS is shown in Figure 2-2. $BaCO_3$, $ZrO_2$, $CeO_2$, and $Y_2O_3$ (all high Purity Chemicals, >99.95%) with 3.56 wt% of $Zn(NO_3)_2 \cdot 6H_2O$ (ako chemicals, 99.9%) were ball-milled in ethanol and subsequently dried at 80 ℃ to obtain precursor powders of $BaZr_{0.4}Ce_{0.4}Y_{0.2}O_3$ (BZCY442). This precursor powder is denoted by Pre-1. Moreover, the precursor powders for the fuel electrode supports (noted by Pre-2) were prepared by mixing Pre-1 and NiO in ethanol and ball-milled. The Pre-2 powders were uniaxially pressed. Thus, we obtained green pellets. The precursor layers of the electrolyte films were spin-coated on both surfaces of the green pellets with sols (Figure 2-3a), which were prepared by dispersing Pre-1 into a solution containing dispersant and binder. These pellets were co-sintered, resulting in compact ceramic discs (Figure 2-3b). The back side of the sintered discs was polished with a mechanical grounder to obtain the half cells. The air electrode functional layer $La_{0.5}Sr_{0.5}CoO_5$ (LSC55) was sputtered on the half cells in chapter 3. Finally, an air electrode was deposited on the electrolyte as a porous air electrode by screen printing (Figure 2-3c).

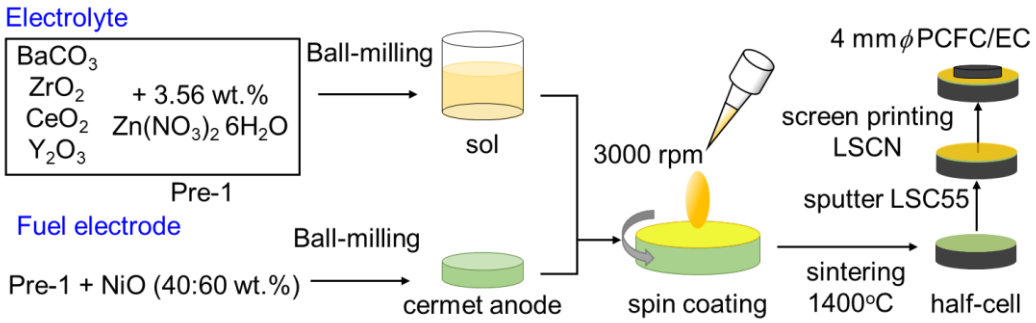


Figure 2-2 The schematic diagram for SSRS fabrication of protonic ceramic cells (PCFCs/ECs).

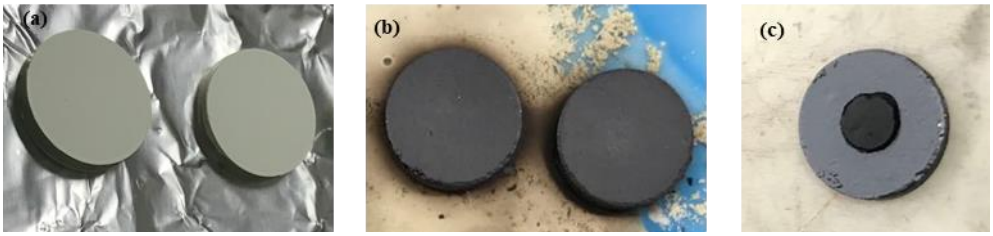


Figure 2-3 Half cells (a) before and (b) after sintering, (c) and the full cell after screen printing air electrode.

## 2-3 Characterizations

### 2-3-1 Structural characterizations

The phase purity of perovskite oxides and PCFCs/ECs was checked by X-ray powder diffraction (XRD; Rigaku, Ultima IV) using Cu Kα radiation (40 kV, 20 mA) in a 2θ range of 20−90°. The scan rate and 2θ step were 5° $min^{-1}$ and 0.02°, respectively.

Brunauer−Emmett−Teller (BET) analysis (MicrotracBel BELSORP Mini-II) was performed to measure the surface area of perovskite oxides. Scanning electron microscopy (SEM; SIGMA500, ZEISS) was performed to measure the microstructure of oxides and PCFCs, the detailed structure was further evaluated using transmission electron microscopy (TEM; JEOL, JEM-2010 F).

*In-situ* Fourier transform infrared (FT-IR) spectroscopy was conducted in diffuse-reflectance mode utilizing a FT/IR-350 spectrometer and FT-IR-4600 Fourier Transform Infrared Spectrometer from JASCO.

### 2-3-2 Rietveld structure refinement

The XRD patterns were refined by the Rietveld method using the Materials Studio or GSAS over the 2θ range of 20−80°.

### 2-3-3 Thermodynamic characterizations for hydration

Thermogravimetric (TG) analysis was performed using a STA2500 thermogravimetric analyzer (Netzsch). Thermal desorption spectroscopy (TDS) analysis couples with mass spectra was performed for as-prepared specimens using an ultra-high vacuum chamber system (ESCO TDS1400) equipped with a quadruple mass analyzer and an infrared lamp heater.

### 2-3-4 Single crystal X-ray absorption spectroscopy

The single crystal X-ray absorption spectroscopy (XAS), including Mn *K*-edge XAFS, O *K*-edge XAS, and Co, Ni *L*-edge, was obtained on the BL01B1 and BL27SU stations of Spring-8 facility, Japan Synchrotron Radiation Research Institute (JASRI) and at beamline BL-2 of Ritsumeikan University SR Center (Shiga, Japan).

### 2-3-5 Fuel cell and electrolysis tests

Impedance spectra were measured with a Solartron 1260A frequency response analyzer implemented with a Solartron 1287 potentiostat (Figure 2-4) in the frequency range of $10^6$ to 0.1 Hz with ac amplitude of 30 mV under OCV condition. The current–voltage (*I–V*) and current–power (*I–P*) characteristics under fuel cell mode and electrolysis mode were recorded on the same apparatus, the measuring apparatus is shown in Figure 2-5.


Figure 2-4 The solartron 1260A frequency response analyzer implemented with a Solartron 1287 potentiostat.

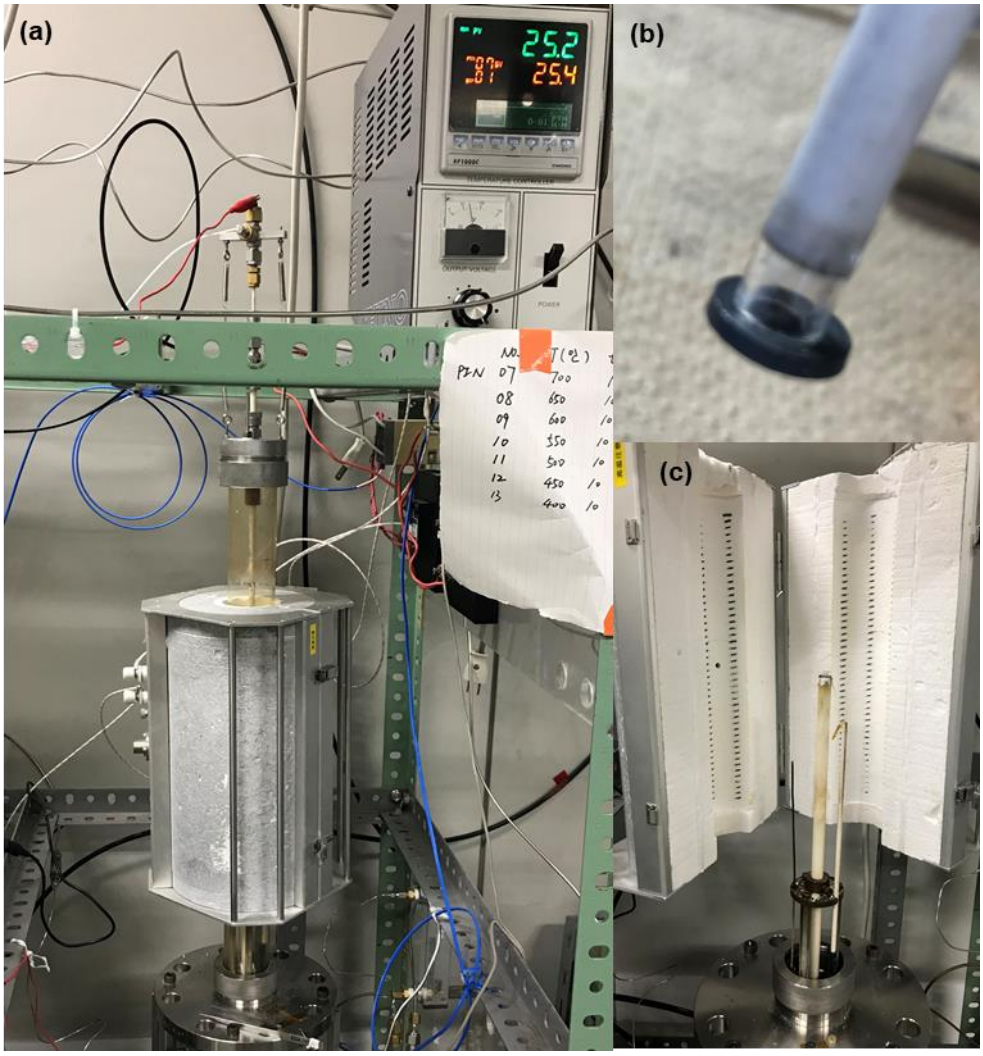


Figure 2-5 (a) The pictures of the FC/EC test equipment with the high-temperature furnace and gas supply system. (b) The picture for sealing with glass ring between the full cells and ceramic tube. (c) The pictures of the cells on the ceramic tube for fuel gas flow.

# Chapter 3 Enormous proton carriers incorporated $La_{0.8}Sr_{0.2}Co_{1-x}Ni_xO_{3-\delta}$ as highly efficient air electrodes for protonic ceramic cells

## 3-1 Introduction

Protonic ceramic fuel cells (PCFCs) and electrolysis cells (PCECs) categorized to protonic ceramic cells as the energy conversion devices have attracted many materials chemists, because the ongoing and worsening climate and energy crises promote materials chemists to urgently develop such efficient and clean electrochemical devices.[1-5] However, the peak power densities (PPDs) for PCFCs especially based on Zr-rich BZCY electrolyte, are still lower than 0.5 W $cm^{-2}$ at 600 °C, [6] and the current densities at 1.3 V for majority of PCECs based on Ba(Zr, Ce, Y)$O_3$ (BZCY) electrolytes are still less than 0.5 A $cm^{-2}$, and some even limit to tens of mA $cm^{-2}$ at 600 °C. [7-11] A major reason for the limited electrochemical performances of PCECs and PCFCs at intermediate temperatures is lack of mixed single-phase $H^+/O^{2-}/e^-$ triple conductors detailed explained in Chapter 1-6, 1-7, and 1-8. Therefore, it is necessary to develop single-phase triple conductors that exhibit sufficient $H^+/O^{2-}/e^-$ conduction to extend the efficient reaction zones beyond the air electrode-electrolyte-gas triple phase boundary and thus reduce the air electrodes' overpotentials and improve electrochemical performances for PCFC/ECs.[12-14]

The hydration reaction (Equation 3-1) is proposed to evaluate the ability of taking proton defects by association between oxygen vacancy and water molecules, the proton defects can be precisely determined by calculating the amount of incorporated water by thermogravimetry (TG) measurements under the controlled atmospheres.

$$O_O^X + V_O^{\bullet\bullet} + H_2O_{(g)} \leftrightarrow 2OH_O^{\bullet} \quad (3\text{-}1)$$

$La_{1-x}Sr_xCoO_{3-\delta}$ is the excellent catalyst for oxide-ion conducting cells, but never categorized as a protonic conductor. Therefore, the strong hydration capability of

$La_{0.8}Sr_{0.2}Co_{1-x}Ni_xO_{3-\delta}$ (LSCN, $x$=0-0.3) in wet air condition at intermediate temperatures was demonstrated in this chapter, the hydration is associated between oxygen vacancy and water molecules, and sufficiently high electrochemical performances in fuel cell and electrolysis mode were obtained by applying LSCN as the air electrodes of protonic ceramic cells.

## 3-2 Experimental Section

### 3-2-1 Synthesis of LSCN

$La_{0.8}Sr_{0.2}Co_{1-x}Ni_xO_{3-\delta}$ (LSCN; $x$ = 0.0, 0.1, 0.2, 0.3) fine powders were synthesized via a citrate precursor route reported elsewhere.[15,16] Firstly, $La(NO_3)_3$•$6H_2O$, $Sr(NO_3)_2$, $Co(NO_3)_2$•$6H_2O$ and $Ni(NO_3)_2$•$6H_2O$ (all from High Purity Chemicals and at 99.99%) in amounts corresponding to the desired stoichiometry were completely dissolved into Milli-Q $H_2O$, and then citric acid (CA; $C_6H_8O_7$•$H_2O$) was added as a chelating agent in a mole ratio of CA:LSCN = 2:1. Next, the citrate solution was heated with vigorous stirring at 60 ℃ for 2-3 h to evaporate the water and promote polymerization. The obtained gelatinous product was calcinated at 500 ℃ for 1 h in air to produce a black-colored precursor. Then, the precursor was annealed in a tube furnace at 800 °C for 15 h under pure $O_2$ atmosphere to get LSCN powders, finally, these oxides were grinded by ball milling under 300 rmp for 2 hours.

### 3-2-2 Fabrication of PCFC/ECs

The protonic ceramic fuel cells/electrolysis cells (PCFCs/ECs) were fabricated by solid-state reactive sintering (SSRS) with a sintering aid of $Zn(NO_3)_2$•$6H_2O$. $BaCO_3$ (High Purity Chemicals, 99.95%), $ZrO_2$ (High Purity Chemicals, 98%), $CeO_2$ (High Purity Chemicals, 99.99%), and $Y_2O_3$ (High Purity Chemicals, 99.99%) with 3.56 wt% of $Zn(NO_3)_2$•$6H_2O$ (Wako chemicals, 99.9%) were ball-milled in ethanol for 2 h and subsequently dried at 80 ℃ to obtain precursor powders of $BaZr_{0.4}Ce_{0.4}Y_{0.2}O_3$ (BZCY442). This precursor powder is denoted by Pre-1. At the same time, the precursor powders for the fuel electrode supports (noted by Pre-2) was prepared by mixing Pre-1 and NiO at a weight ratio of 40 : 60 (BZCY442 : NiO) in ethanol and ball-milled for 2 h. The Pre-2 was uniaxially pressed under 15 MPa and subsequently, pressed isostatically under a hydrostatic pressure of 100 MPa, and thus green pellets (~12 mm

diameter, ~1.2 mm thickness) of fuel electrode-support precursors were obtained. Precursor layers of electrolyte films were spin-coated on both surfaces of the green pellets with sols which were prepared by dispersing Pre-1 into a solution containing dispersant (20 wt% polyethyleneimine ($M_w$ 28000) dissolved in α-terpineol, called Sol-1) and binder (5 wt% surfactant dissolved in α-terpineol, called Sol-2). These pellets were co-sintered at 1500 ℃ for 10 mins then decreased to 1400 ℃ for 8 h at air atmosphere, which resulted in a compact ceramic disc with ca. 9 mm$\phi$ × 1 mm*d*. The back side of the sintered discs were polished with a mechanical grounder and then $La_{0.5}Sr_{0.5}CoO_3$ (LSC55) film was fabricated on BZCY442 electrolyte as functional interlayer by RF sputtering at 500 ℃ for 2 hours in Ar atmosphere, the RF power is 40 W, the post annealing temperature and time are 700 ℃ and 1 h in oxygen atmosphere, respectively. Finally, the back side was applied with Pt paste as a current collector, LSCN oxides as button air electrodes were deposited on sputtered electrolyte as a porous cathode by screen printing, the oxide inks were obtained by mixed oxides, Sol-1 and Sol-2 in weight ratio 9:3:1, LSCF6428 past was commercial product.

### 3-2-3 Characterizations

#### (a) Structural characterizations

The phase purity was checked by X-ray powder diffraction (XRD; Rigaku, Ultima IV) using Cu *K*α radiation (40 kV, 20 mA) in a 2$\theta$ range of 20-90°. The scan rate and 2$\theta$ step were 5° $min^{-1}$ and 0.02°, respectively. The microstructure of LSCN oxides and PCFC/ECs was observed by using scanning electron microscope (FESEM; SIGMA500, ZEISS) operated at 1.0-5.0 kV and the detailed structure was further evaluated using transmission electron microscopy (TEM; JEOL, JEM-2010 F) with the system operated at 200 kV.

**(b) Thermodynamic characterizations for hydration**

Thermogravimetric (TG) analysis was performed using a STA2500 thermogravimetric analyzer (Netzsch). The TG measurements were carried out using about 20 mg of LSCN oxide powders. The possibility of hydration was performed by heating from room temperature (RT) to 1000 ℃ at a ramp rate of 5 ℃ $min^{-1}$ under a flow of dry and wet air at 50 sccm. Dry air was prepared by mixing pure Ar and $O_2$ in $Ar/O_2$ =4/1 (v/v). Wet gases were prepared by bubbling them through a water bath at 20 ℃ at a flow rate of 50 sccm; the resultant gases had a water partial pressure ($p_{H2O}$) of 0.023 $p_0$ ($p_0$ = 101.3 kPa). Hydration ability cyclic tests were operated at 405 ℃ by switching dry and wet air ($p_{H2O}$ = 0.023 $p_0$) every 30 mins. And the hydration ability at the temperature range of 220-800 ℃ was measured by the following procedure: the sample was once measured in dry air by cooling from 800 to 220 ℃ at a rate of 5 ℃ $min^{-1}$, and abruptly heated again to 800 ℃, and then, the TG was measured again by cooling in the same conditions after switching the atmosphere to wet air.

**(c) Single crystal X-ray absorption spectroscopy**

LSCN oxides were pressed into the pellets (~5 mm diameter, ~1 mm thickness), and pre-treated at 405 ℃ in dry and wet air for 12 hours for dehydrated and hydrated samples, then, the pellets were grinded into powders. Single crystal X-ray absorption spectroscopy was carried out for the powders under ultra-high vacuum conditions at ambient temperature at BL27SU SPring-8. Transition metal L-edges (Co: 770–805 eV and Ni: 845–875 eV) and the oxygen K-edge (524–550 eV) of pre-treated samples were recorded using fluorescence yielding (FY) method.

**(d) Fuel cell and electrolysis tests**

As-prepared cells were sealed in the cell sealing system, as shown in Figure 2-5 in Chapter 2, then increased to 700 ℃ for NiO reduction by $H_2$ to make porous fuel

electrode for ~ 2 h. Then, the wet air with mixed 4 mL $min^{-1}$ $O_2$ and 16 mL $min^{-1}$ Ar by bubbling in a pure water at 25 ℃ was inlet to air electrode side, and the wet $H_2$ at 40 mL $min^{-1}$ was into the fuel electrode side. Impedance spectra of PCFC/ECs was measured by 2-probe methods, with a Solartron 1260A frequency response analyzer implemented with a Solartron 1287 potentiostat (in Figure 2-4 in Chapter 2) in the frequency range of $10^6$ to 0.1 Hz with ac amplitude of 30 mV under OCV condition, current-voltage (*I–V*) from 1.8 V to 0 V *vs* counter electrode were recorded on the same apparatus at the temperature range of 450-700 ℃. Durability test was measured by the same apparatus.

## 3-3 Results and discussion

### 3-3-1 Preparation of LSCN

Figure 3-1a shows the XRD patterns of $La_{0.8}Sr_{0.2}Co_{1-x}Ni_xO_{3-\delta}$ (LSCN; $x$ = 0.0, 0.1, 0.2, and 0.3). $La_{0.8}Sr_{0.2}Co_{1-x}Ni_xO_{3-\delta}$ oxides with $x$ = 0.0, 0.1, 0.2, and 0.3 are denoted hereafter as LSCN8210, LSCN8291, LSCN8282 and LSCN8273, respectively, according to the Co/Ni molar ratios. All oxides exhibit the similar XRD patterns as rhombohedral $La_{0.9}Sr_{0.1}CoO_3$ (Space group *R-3c*; PDF#28-1229). The ball-and-stick model of rhombohedral LSC8210 is shown in Figure 3-1b. High resolution TEM (HR-TEM) images of LSCN8210 (Figures 3-1c-e) show clear lattice fringes with spacing of 0.221 nm and 0.271 nm (Figures 3-1d and e), which is corresponding to a sequence of (202) and (110) planes, respectively, thus confirming LSCN oxides have rhombohedral perovskite type structure. LSCN powder is comprised a fine particle with a diameter of 50 to 100 nm, as confirmed by SEM (Figure 3-2).

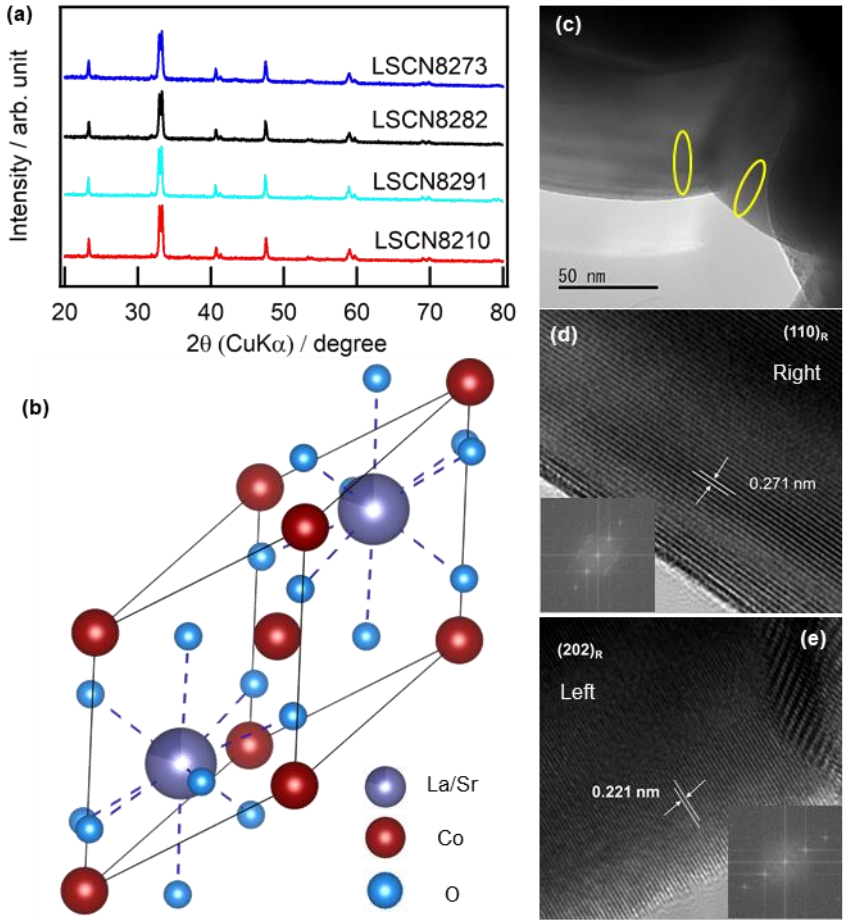


Figure 3-1 XRD patterns of $La_{0.8}Sr_{0.2}Co_{1-x}Ni_xO_{3-\delta}$ (LSCN; $x$ = 0.0, 0.1, 0.2, and 0.3) powders (a). Ball-and-stick model of rhombohedral $La_{0.8}Sr_{0.2}CoO_3$ (LSC8210) (b). HR-TEM image of LSCN8210 (c), (202) (d) and (110) (e) of rhombohedral LSC8210, and corresponding fast Fourier transform (FTT) (insets of d and e).

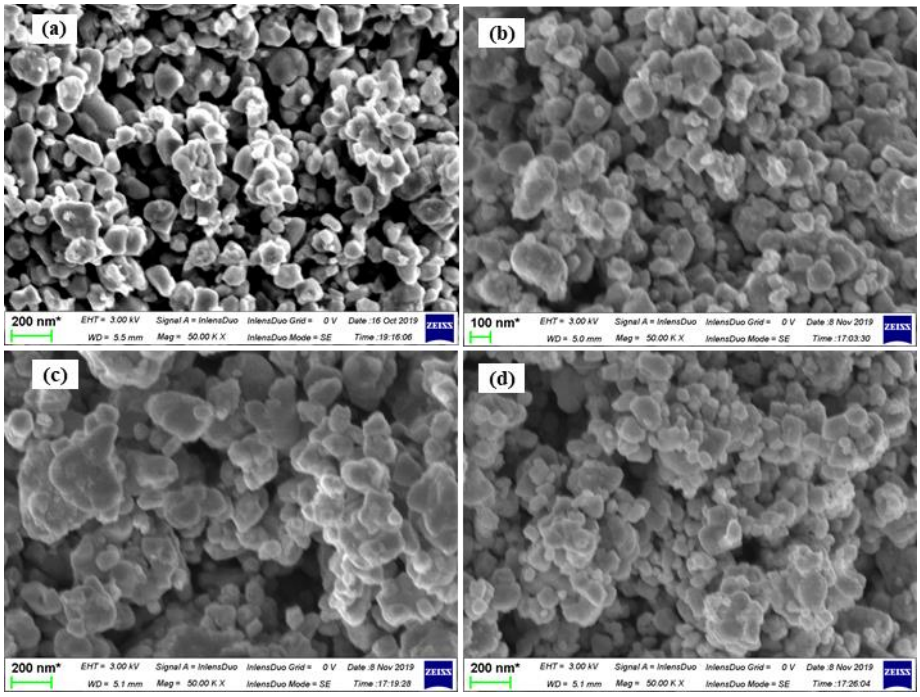


Figure 3-2 SEM images of (a) LSCN8210, (b) LSCN8291, (c) LSCN8282, and (d) LSCN8273.

### 3-3-2 Hydration/dehydration reactions of LSCN oxides

Figures 3-3a-d show thermogravimetric (TG) curves of the LSCN oxides power measured in dry and wet air ($p_{H2O}$ = 0.023 $p_0$). LSCN exhibit three steps of thermal weight losses in air. The weight losses at $T$ < 200 ℃ and at approximately 700 ℃ can be attributed to the desorption of surface $H_2O$ and the lattice oxygen loss with the thermal reduction of $Co^{4+}$ to $Co^{3+}$ and/or $Ni^{3+}$ to $Ni^{2+}$. LSCN exhibits a clear mass loss at approximately 400 ℃, probably because of the dehydration following the release of bulk $H_2O$, since the onset temperature corresponding to the mass loss increases from about 350 to 450 ℃ when changing dry to wet air (Figures 3-3a-d).

In order to verify the capability of reversible hydration/dehydration reactions, mass changes for all LSCN oxides are monitored by switching repeatedly between dry and wet ($p_{H2O}$=0.023 $p_0$) air every 30 mins for 4 cycles (Figures 3-3e-h). The temperature was fixed at 405 ℃, which is the intermediate between the dehydration temperatures in dry (350 ℃) and wet air (450 ℃). All LSCN oxides exhibit reversible mass changes by responding to dry and wet air, with a mass gain upon exposure to wet gases ($p_{H2O}$=0.023 $p_0$) and an equal mass loss when exposed to dry gases. The hydration/dehydration behavior is completely repeatable since the deviation between the amount of water release during dehydration and water uptake by hydration is within 5%. The weight variable ($\Delta W$) is defined as the mean weight difference between the samples equilibrated in dry and wet air. LSCN8210 exhibits the highest $\Delta W$ value of 0.57 wt% (Table 3-1) in wet air, which is even higher than the corresponding value of cubic perovskite type $La_{0.7}Sr_{0.3}MnO_3$ (*C*-LSM73; $\Delta W$ = 0.5 wt%) at the same temperature.[15] $\Delta W$ decreases with Ni contents ($x$) with equaling to 0.48, 0.31 and 0.24 wt% for $x$ = 0.1, 0.2 and 0.3, respectively.

The hydration capability ($\Delta n$) can be quantified by using $\Delta W$, which is defined as the molar fractions of water absorbed, i.e. $\Delta n = n(H_2O) / n$(LSCN8210). $\Delta n$ of LSCN oxides

decreases from 0.075 to 0.031 with increasing Ni contents ($x$) from 0 to 0.3 (Table 3-1). The decreased hydration/dehydration ability maybe attributed to that the decreased Co cations, $V_O^{\bullet\bullet}$ connected Co cations is essential for hydration / dehydration reaction. The concentrations of protonic defects, $[OH_O^{\bullet}]$, which must be equivalent to twice of $\Delta n$ (Equation 3-1 and Table 3-1), for LSCN series are comparable to those of the well-known proton conductors such as $BaCe_{0.9}Y_{0.1}O_3$ (~0.1) and $BaZr_{0.9}Y_{0.1}O_3$ (~0.08) at 600 °C in wet $N_2$ atmosphere ($p_{H2O}$ = 0.023 atm).

Finally, the hydration ability of LSCN at the operation temperatures of PCFCs and PCECs (400-700 ℃) was examined (Figure 3-4). Here, the temperature once increased to 800 °C and was kept isothermally for 2 h in dry air, and then TG measurements started by cooling from 800 to 220 °C at a rate of 5 °C $min^{-1}$ in the same atmosphere (1st run). Subsequently, the temperature increased again to 800 °C with keeping at the temperature for 2 h in wet air, and the TG in wet air started by the same temperature program (2nd run). Figure 3-4a show the relative mass changes of LSCN8273 during 1st and 2nd run, in which the relative mass was calculated by divided the masses at each temperature with the mass at 800 °C. The mass in wet atmosphere is clearly larger than that in dry air in the measure temperature range, and the gap between both curves expand with decreasing temperature. The proton concentrations are 0.046, 0.012, 0.009 molar fraction at 405, 500 and 600 °C (Figure 3-4b), which is consistence with the results of Figure 3-3h. These provide a clear verification for the hydration capability of LSCN oxides at the device operation temperatures.

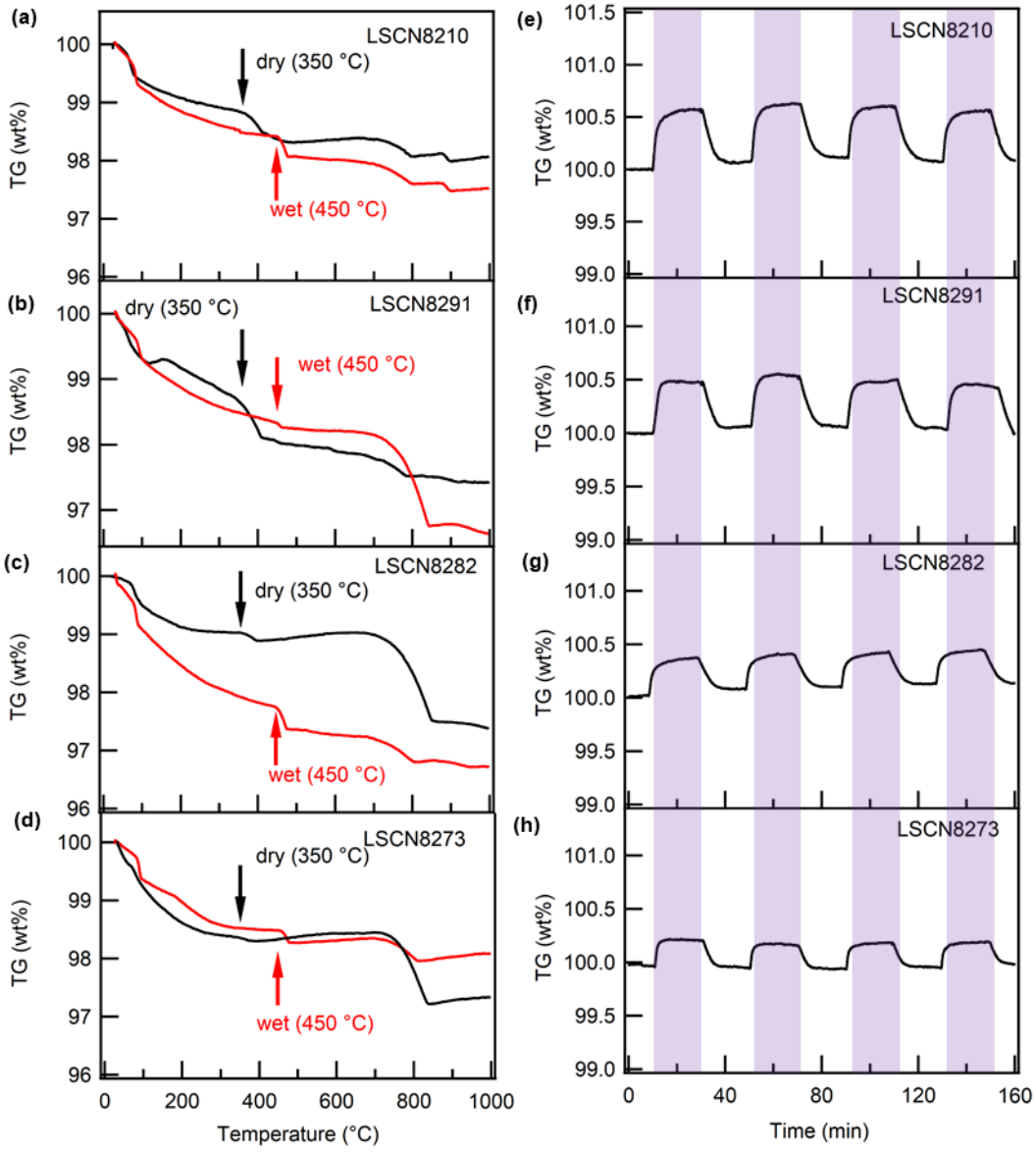


Figure 3-3 TG curves of (a) LSCN8210, (b) LSCN8291, (c) LSCN8282, and (d) LSCN8273 measured in dry and wet air ($p_{H2O}$=0.023 $p_0$). The weight gain/loss in response to atmospheric switching between wet/dry air every 30 mins for (e) LSCN8210, (f) LSCN8291, (g) LSCN8282, and (h) LSCN8273 at 405 °C. In (e)-(h), pale purple areas represent the durations of wet air.

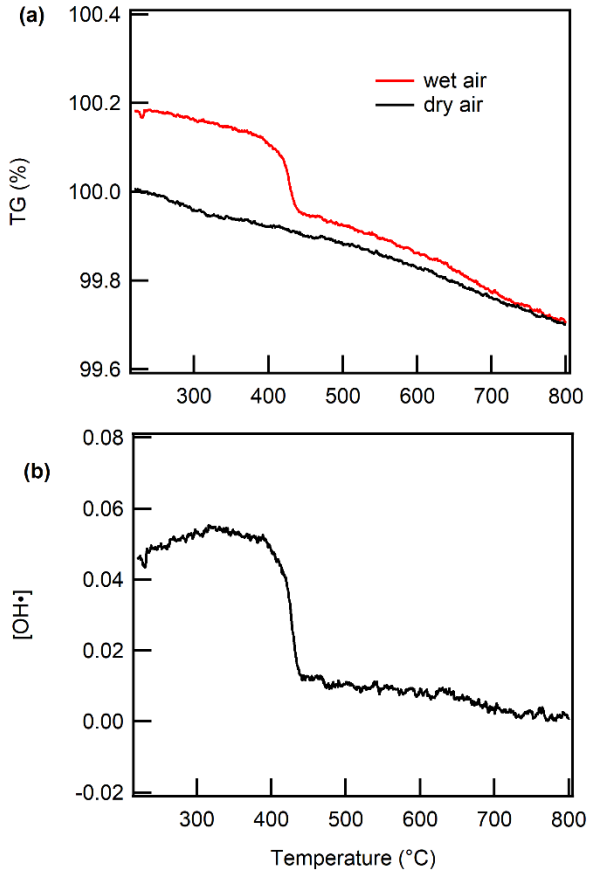


Figure 3-4 (a) TG curves of at 220-800 ℃ in dry and wet air, and (b) calculated proton concentrations from 220-800 ℃ for LSCN8273 oxide.

Table 3-1 Hydration properties of LSCN and other triple phase conductors.

| Systems | ΔW (wt%) | Δ*n* * | Proton concentration* | Temperature (℃) | $p_{H2O}$ / $p_0$ | Ref. |
|---|---|---|---|---|---|---|
| LSCN8210 | 0.57 | 0.075 | 0.15 | 405 | 0.023 | This work |
| LSCN8291 | 0.48 | 0.063 | 0.126 | 405 | 0.023 | This work |
| LSCN8282 | 0.31 | 0.041 | 0.082 | 405 | 0.023 | This work |
| LSCN8273 | 0.24 | 0.031 | 0.062 | 405 | 0.023 | This work |
| LSCN8273 | 0.11 | 0.012 | 0.025 | 500 | 0.023 | This work |
| LSCN8273 | 0.09 | 0.011 | 0.022 | 600 | 0.023 | This work |
| *C*-$La_{0.7}Sr_{0.3}MnO_{2.95}$ | 0.56 | 0.070 | 0.142 | 415 | 0.023 | 15 |
| *C*-$La_{0.7}Sr_{0.3}MnO_{2.95}$ | 0.32 | 0.041 | 0.082 | 415 | 0.009 | 15 |
| $PrBa_{0.5}Sr_{0.5}Co_{1.5}Fe_{0.5}O_{5+\delta}$ | - | 0.018 | 0.036 | 200 | 0.02 | 27 |
| $Ba_{0.95}La_{0.05}Fe_{0.8}Zn_{0.2}O_{3-\delta}$ | - | 0.050 | 0.10 | 200 | 0.016 | 28 |
| $BaCo_{0.4}Fe_{0.4}Zr_{0.2}O_{3-\delta}$ | - | - | 0.015-0.05 | 200-400 | 0.015 | 29 |
| $Ba_{0.5}Sr_{0.5}Fe_{0.8}Zn_{0.2}O_{3-\delta}$ | - | - | 0.015 | 350 | 0.02 | 30 |
| $Ba_{0.5}Sr_{0.5}Fe_{0.8}Zn_{0.2}O_{3-\delta}$ | - | - | 0.02 | 400 | 0.02 | 30 |
| $Ba_{0.5}Sr_{0.5}Fe_{0.8}Zn_{0.2}O_{3-\delta}$ | - | - | 0.013-0.032 | 350-600 | 0.02 | 30 |
| $PrBa_{0.5}Sr_{0.5}Co_{1.5}Fe_{0.5}O_{5+\delta}$ | - | 0.009 | 0.018 | 600 | 0.02 | 27 |
| $Ba_{0.95}La_{0.05}Fe_{0.8}Zn_{0.2}O_{3-\delta}$ | - | 0.023 | 0.056 | 400 | 0.016 | 31 |
| $Ba_{0.95}La_{0.05}Fe_{0.8}Zn_{0.2}O_{3-\delta}$ | - | 0.012 | 0.024 | 500 | 0.016 | 31 |
| $BaCo_{0.4}Fe_{0.4}Zr_{0.1}Y_{0.1}O_{3-\delta}$ | - | 0.095 | 0.019 | 500 | 0.001 | 29 |

* Represented by molar fraction.

In order to confirm the chemical state of O and metal atoms before and after hydration, X–ray adsorption spectroscopy (XAS) was carried out at the Co *L*-edge, Ni *L*-edge, and O *K*-edge for the hydrated and dehydrated LSCN8210 and LSCN8273 oxides (Figure 3-5). The spectra were normalized by the jump height of the main edge. Metal *L* edge adsorption peak corresponding to the transition from 2*p* core level to unoccupied states normally sprits into $L_2$ and $L_3$ peaks attributed to the 2*p* core-hole spin-orbit interaction. Co $L_3$ and $L_2$ absorption peaks appear at around 779 eV and 794 eV, respectively (Figure

3-5a). In both LSCN8210 and LSCN8273, the Co *L*–edge features are perfectly identical between hydrated and dehydrated phases, indicating that Co valence state does not change by hydration. Although Ni $L_3$–edge peak (852 eV) is overlapped with La *M*–edge peak (849 eV) and thus is not well-defined (Figure 3-5b), Ni $L_2$ features of LSCN8273 remain unchanged before and after hydration, which confirms Ni valence state is also kept through the hydration. In conclusion, there is no Co and Ni redox during hydration/dehydration reaction.

O *K*–edge XANES spectra, however, were found to change drastically with hydration (Figure 3-5c). The XANES of cobalt and nickel oxides correspond to the transitions of the O *1*s electrons to the unoccupied O *2p* states mixed in the M *3d* bands (M = Co and Ni), and thus, tend to display the complicated features because of the strong *2p–3d* hybridization. The O K-edge features of LSCN8210 are very similar to those reported for $La_{0.8}Sr_{0.2}CoO_3$ elsewhere.[17,18] Based on these previous papers,[19] the pre-edge features (A, B, α, and β) below the threshold (533 eV) could be assigned to the O *2p* states mixed with Co *3d* bands, ones between 534 and 538 eV (C and D) to O *2p* states mixed with La *5d* bands, and ones between 538 and 550 eV (E and F) to O *2p* states mixed with Co *4sp* bands. Hereafter, we discuss mainly the pre-edge features below 533 eV.

In dehydrated LSCN8210, the pre-edge peaks at 529.3 and 530.6 eV, which are denoted as A and B, respectively, are identical to antibonding $e_g$ and $t_{2g}$ states, respectively.[19,20] The A and B peaks decreases after hydration, whereas additional two peaks newly develop at 530.7 and 531.8 eV as denoted as α, and β, respectively, even though the α looks very broad by overlapped with B. The energy level of antibonding O *2p* states could be increased in the pre-edge region at around 531.8 eV and, alternatively, the intensity of pre-edge peaks of A and B significantly deceases by hydration. It has been verified by X-ray photoelectron spectroscopy (XPS) that the O*1s* core level in the hydroxide groups is chemically shifted by 1.2 eV to higher binding

energy relative to oxygen sites, because a decrease of the negative charge on the ionized atom, leads to a increasement of its core binding energies.[21,22] This effect could involve comparable chemical shift in the energy position of O K-edge XAS features. In fact, similar chemical shifts of O K-edge pre-edge peaks was reported for NiO and $Ni(OH)_2$ systems, in which the pre-edge position of $Ni(OH)_2$ (533.3 and 532.1 eV) is higher than that of NiO (531.7 eV).[23,24] The energy positions of α (530.7 eV) and β (531.8 eV) are higher than those of A (529.3 eV) and B (530.6 eV) by about 1 eV, respectively, which indicates that α and β can be assigned to $e_g$ and $t_{2g}$ component of hydroxyl groups, respectively. Thus, the small peaks at 529.2 and 530.2 eV in the dehydrated phase must be due to the residue of the hydrated phase. The total areas of A, B, α and β peaks are almost same between the hydrated and dehydrated phase (Figures 3-5d and e), revealing that the population of the unoccupied O *2p* states are preserved through hydration and dehydration reactions.

Hydrated and dehydrated LSCN8273 exhibit similar spectral features as such LSCN8210, except for the pre-edge features below 533 eV. LSCN8273 show clear two peaks in the lower energy side of A and B, which is noted as A' (528.1 eV) and B' (529.5 eV), respectively. Referred to the pre-edge peaks of $LaNiO_3$ due to the hybridization of O(*2p*) – Ni(*3d*) appearing in the relatively low energy position than those of $LaCoO_3$,[25] the peak of A' and B' can be featured intermixing of antibonding $e_g$ and $t_{2g}$ states due to O(2p)/Ni(3d) hybridization. Likely in LSCN8210, the intensity of A' and B' decreases while additional α and β peaks appears at 530.9 and 531.6 eV, respectively, attributed to the formation of hydroxyl group by hydration. The totals in the peak areas of A', B', α and β are similar each other before and after hydration (Figures 3-5d and e), which suggest that Co–O and Ni–O bonds retain significant degree of covalency even after hydration. Combined results of XAS measurements clarifies that the thermochemical hydration of LSCN8210 is carried out by the association reaction of oxygen vacancy and water as represented by equation (3-1) without the charge proportionation between

transition metal and O, the different hydration behavior between $La_{0.8}Sr_{0.2}CoO_3$ and $La_{0.7}Sr_{0.3}MnO_3$ systems can be attributed to the high covalent nature of Co-O bond than Mn-O bonds.[26]

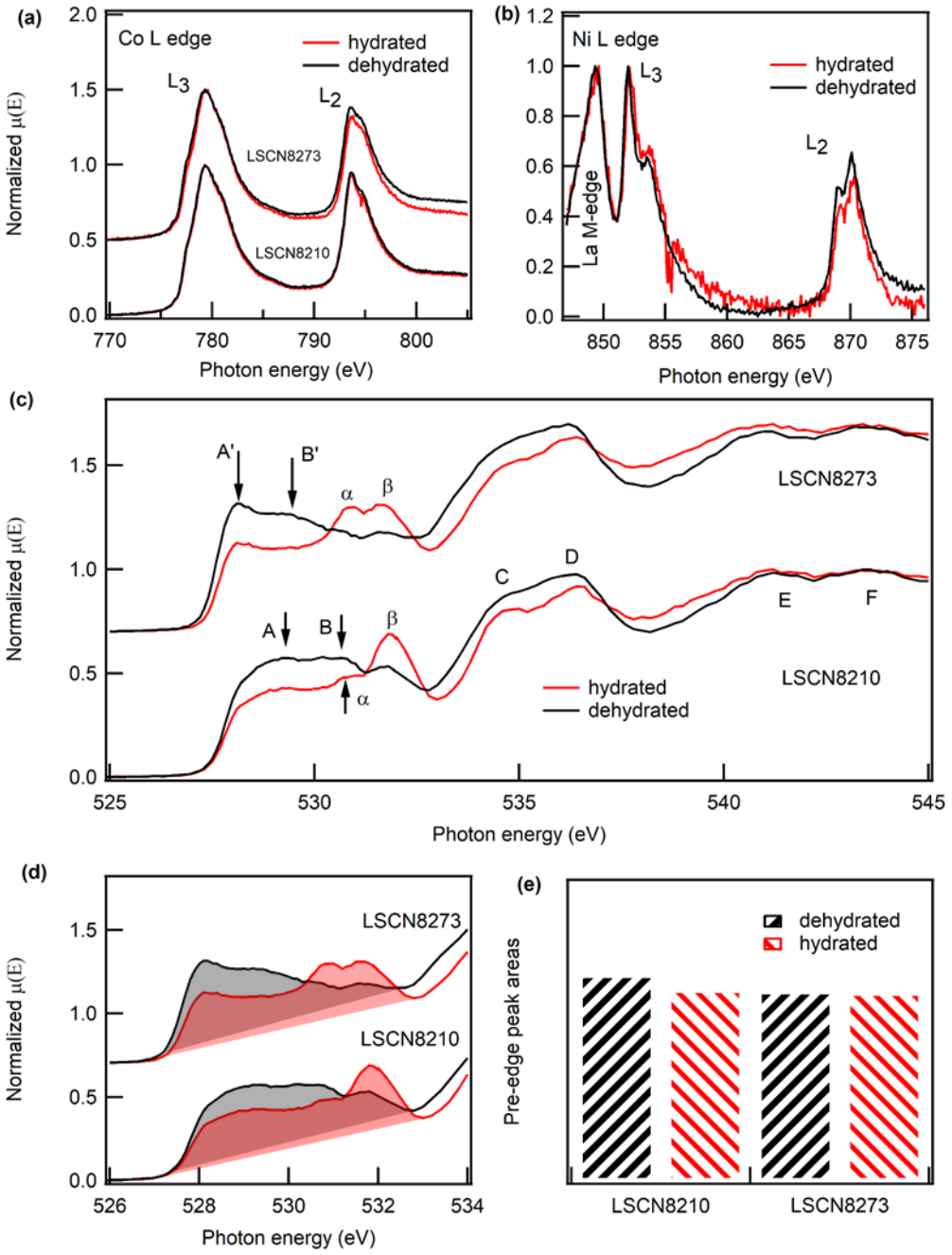


Figure 3-5 (a) Co *L*-edge, (b) Ni *L*-edge, and (c) O K-edge XAS spectra, (d) Pre-edge areas of O 2*p*-Co/Ni 3*d*, and (e) the peaks area of peaks A, B, A', B', α and β by integrating the black and red areas in (d) for hydrated and dehydrated LSCN8210 and LSCN8273, The hydrated and dehydrated phases were prepared by preheating at 405 °C for 6 h in wet and dry air, respectively. Black and red distinguish the dehydrated and hydrated phases, respectively. A-F, α and β peaks are represented in the main text.

### 3-3-3 Protonic ceramic cells with LSCN air electrodes

The bulk hydration ability of LSCN oxides ensures the bulk proton conduction at intermediate temperature range as analyzed above, so that LSCN oxides should be promising for the $H^+/O^{2-}/e^-$ triple conducting electrodes of PCFCs and PCECs in the intermediate temperature region. Here, we fabricated thin film cells comprising $BaZr_{0.4}Ce_{0.4}Y_{0.2}O_3$ (BZCY442) electrolyte films and Ni / BZCY442 cermet support with LSCN air electrodes and evaluated the performances in FC and EC modes. The cross-section SEM images for the cell with LSCN8210 air electrode are shown in Figure 3-6. The cell comprises of three distinct layers: porous LSCN layer made of 50 nm-size particles, dense electrolyte film with a thickness of 24 μm and porous cermet support (Figure 3-6a). LSCN8210 air electrode maintains perfect contact with electrolyte without any delimitation (Figure 3-6b), and the electrolyte is densely sintered with the grains of ~9 μm diameters (Figures 3-6c). The Ni-BZCY442 cermet support retains clear porosity to provide enough pathway for fuel diffusion (Figure 3-6d).

The current-voltage (*I-V*) curves (Figure 3-7) for PCFC/ECs were recorded by sweeping voltages on LSCN air electrodes from 1.8 V to 0 V *vs* counter electrode with supplying wet hydrogen to the fuel electrode and wet air to LSCN side. The wet gases ($p_{H2O}$ = 0.03 atm) were prepared by bubbling in a pure water at 25 ℃. The negative current density refers to electrolysis cell operation, called EC mode, while the positive current density to fuel cell operation, called FC mode. Here the cell with mixed $O^{2-}/e^-$ conducting $La_{0.6}Sr_{0.4}Co_{0.2}Fe_{0.8}O_3$ (LSCF6428) was also examined to compare ones using triple conducting LSCN oxides (Figures 3-7c and f). Cell potential value at zero current density is defined to the open-circuit voltage (OCV). All cells exhibit similar OCVs with the values increasing from 0.99 V to 1.1 V with lowering temperatures from 700 to 500 ℃ (Figures 3-7a-c, Table 3-2), which are slightly lower than the theoretical OCVs because of the hole conductivity of BZCY442 electrolytes. However, the output

currents are largely altered with the different air electrodes in both EC and FC modes. In EC mode, the current densities with 1.3 V bias at 700, 600 and 550 ℃ are 2.22, 0.868 and 0.482 A $cm^{-2}$, respectively, for LSCN8210, and 2.32, 1.09 and 0.684 A $cm^{-2}$, respectively, for LSCN8273. Although these electrolysis currents do not reach to the values (1.92 A $cm^{-2}$ at 600 ℃) reported by Choi,[27] these are higher than most of the oxide ion conducting electrolysis cells (0.08~0.21 A $cm^{-2}$; Table 3-3).[32,33,34] Moreover LSCN cells exhibit pronounced fuel cell performances. LSCN8210 achieves the peak power density (PPD) of 1.13, 0.724 and 0.526 W $cm^{-2}$ at 700, 600 and 550℃, respectively, and LSCN8273 of 1.25, 0.882 and 0.652 W $cm^{-2}$ at 700, 600 and 550 ℃, respectively. The PPDs of our LSCN cells are considerably higher than those of the PCFC with Zr-rich side Ba(Zr, Ce, Y)$O_3$ electrolytes, because the PPDs of the latter cases are still limited to a few hundred mW $cm^{-2}$ at 600 ℃ as listed in Table 3-3. In general, PCFCs tends to show higher power outputs with increasing Ce contents of BZCY electrolytes because the proton conductivity is increased with the contents.[35] Actually, PPDs of the LSCN cells at 700°C is close to the champion data of PCFCs based on Ce-rich side, $BaZr_{0.1}Ce_{0.7}Y_{0.1}Yb_{0.1}O_3$ (BZCYYb1711) (1.37 W $cm^{-2}$) and $BaZr_{0.1}Ce_{0.7}Y_{0.2}O_3$ (BZCY172) (1.28 W $cm^{-2}$) at 700 ℃ (Table 3-3).[36,37]

Apparently, the electrochemical performances of the LSCN cells were much superior to those of the cells using a mixed $O^{2-}/e^-$ double conducting LSCF6428 electrode. The LSCF6428 cell yields the electrolysis currents of 1.57, 0.498 and 0.265 A $cm^{-2}$ at 700, 600 and 550 ℃, respectively, with 1.3 V bias, and the PPDs of 0.842, 0.475 and 0.301 W $cm^{-2}$ at 700, 600 and 550 ℃, respectively. (Figures 3-7c, f and 3-8a, b). The electrolysis currents and PPDs of LSCN8273 cell at 600 ℃ are 2.2 and 2.1 times as the values of LSCF6428 cell. Finally, the durability of LSCN8210 cell was examined by conducting constant voltage operation of electrolysis under 1.3 V at 600 ℃. The cell yielded a stable output without degradation for about 60 hours, confirming the excellent durability of LSCN under relatively high voltage conditions (Figure 3-9). In a

conclusion, the LSCN is promising air electrodes for PCFCs and PCECs.

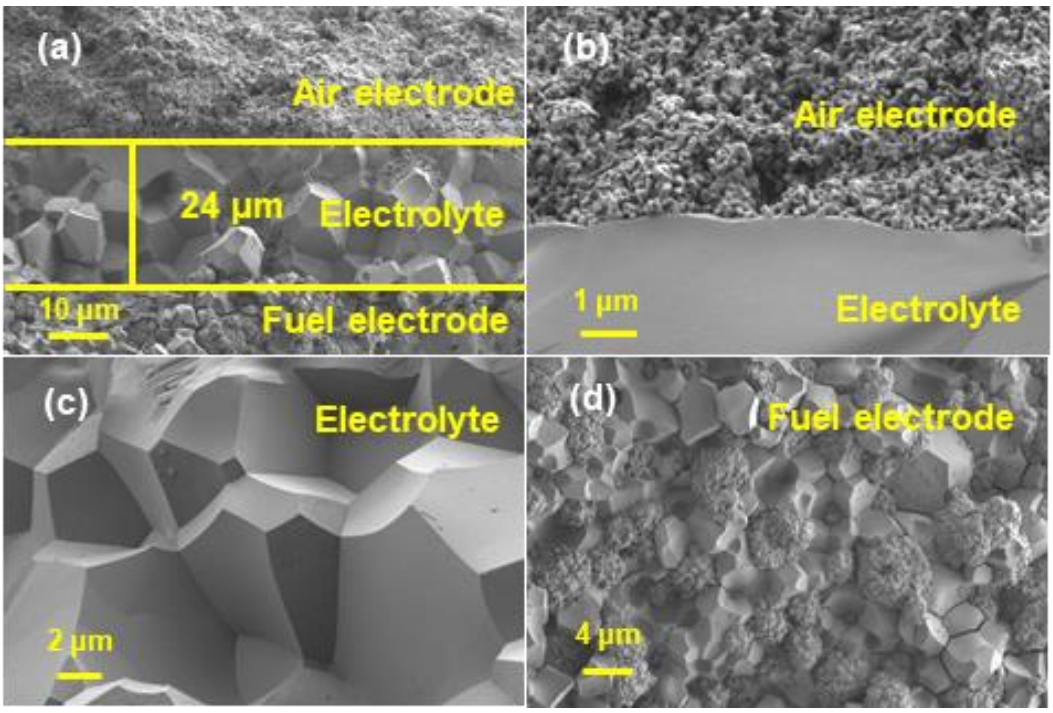


Figure 3-6 (a) Cross section SEM images of cermet-supported PCFC/EC with BZCY442 electrolyte thin films and LSCN8210 air electrodes. (b) High magnification near the interface between LSCN8210 electrode and BZCY electrolyte. Magnifications to highlight grain sizes of (b) BZCY442 electrolyte and (c) BZCY442-Ni cermet support after reduction.

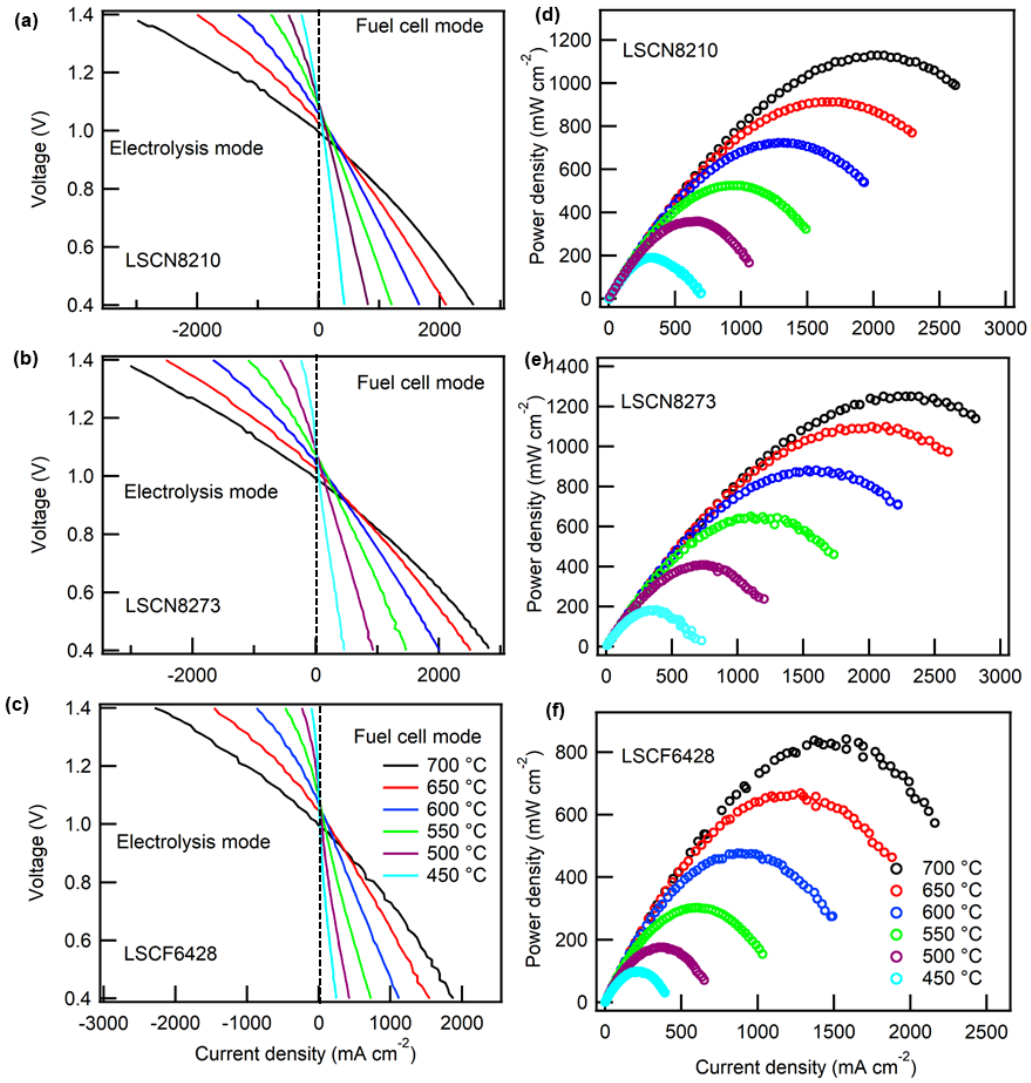


Figure 3-7 Current-Voltage (*I-V*) curves of PCFC/ECs with (a) LSCN8210, (b) LSCN8273 and (c) LSCF6428 air electrodes in the temperature range of 450-700 °C. The negative current was set to electrolysis mode. The current-voltage-power (*I-V-P*) curves of fuel cell with (d) LSCN8210, (e) LSCN8273, and (f) LSCF6428 air electrodes.

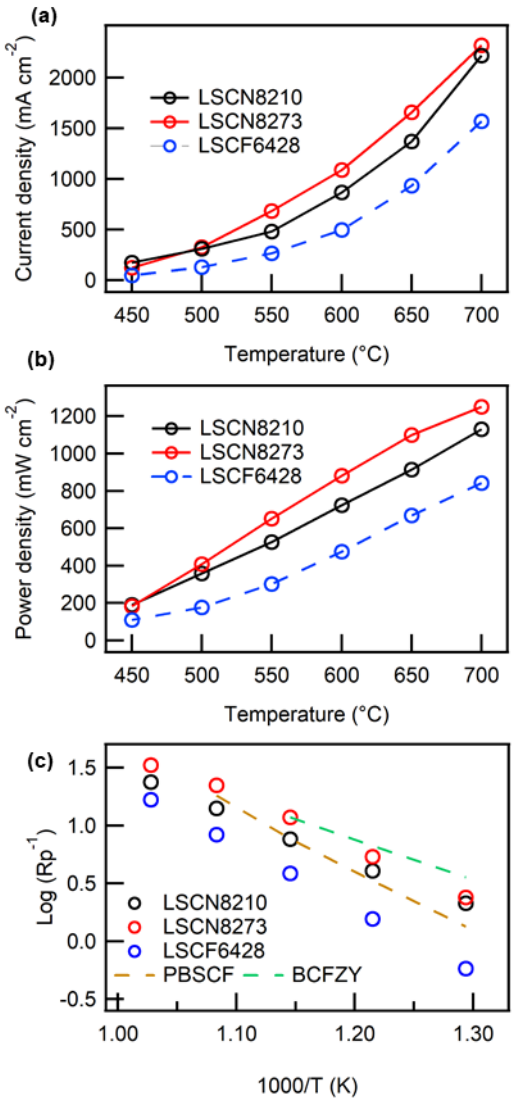


Figure 3-8 (a) Electrolysis current at 1.3 V and (b) PPDs in FC mode for the BZCY442 base cells with different air electrodes at each temperature. (c) Arrhenius plots of $R_p$ under OCV.

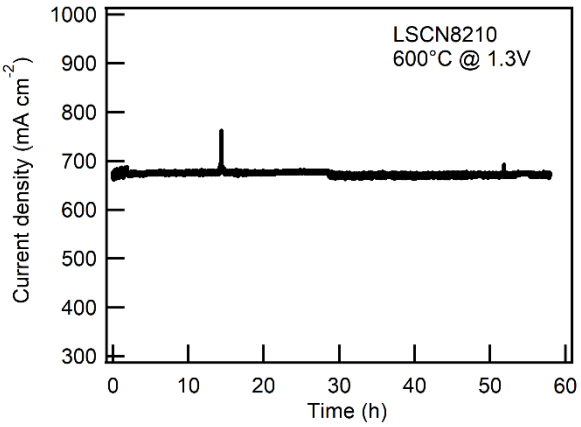


Figure 3-9 Durability test of LSCN8210 cell in a constant voltage operation under 1.3 V at 600 ℃.

Table 3-2 Theoretical and observed open circuit voltages (OCVs) of PCFCs with LSCN and LSCF6428 air electrodes at 700, 600 and 500 ℃.

| OCVs | Theoretical | LSCN8210 | LSCN8273 | LSCF6428 |
|---|---|---|---|---|
| 700 ℃ | 1.140 | 0.99 | 0.99 | 0.99 |
| 600 ℃ | 1.152 | 1.06 | 1.05 | 1.07 |
| 500 ℃ | 1.164 | 1.10 | 1.09 | 1.10 |

Electrochemical impedance spectra (EIS) of LSCN and LSCF cells were measured under OCV condition (Figure 3-10). In general, the Nyquist plots of impedance responses of PCFC and PCEC have the *x*-intercept in a high-frequency region, which corresponds to electrolyte resistances ($R_{ohm}$). After the intercept, they exhibit broad semi-arcs due to the interfacial polarization resistance at the cathode side, and, the diameters of the arcs provide polarization resistance ($R_p$) at the cathode side. The diameters of the semi arcs of the fuel cells with LSCN cathodes are several times smaller than those of the cells with LSCF6428 ones, revealing that $R_p$ of the former is

much lower than that of the latter despite their similar chemical compositions. Figure 3-8c shows Arrhenius plot of $R_p$ for the cells with deferent cathodes, determined from the diameters of the impedance semi-arcs under OCV condition. The $R_p$ of LSCN cells are much smaller than those of LSCF6428 cells in the range from 700 to 450°C. Moreover, the gap between both expand with decreasing temperature (Figure 3-8c) because the activation energy ($E_a$) of $R_p$ for LSCN (about 0.72 eV) are much smaller than that of LSCF6428 (1.1 eV, Figure 3-8c). This feature validates the proton conductivity of LSCN electrodes, because the hydration degree of LSCN increase with decreasing temperatures and thus, the proton conductivity more efficiently promotes the water formation and dissociation at lower temperatures.

Surprisingly, the $E_a$ of LSCN8210 cell is smaller than other triple conducting oxide electrodes, such as $BaCo_{0.7}(Ce_{0.8}Y_{0.2})_{0.3}O_{3-\delta}$ (BCCY; 1.13 eV),[6] $BaCo_{0.4}Fe_{0.4}Zr_{0.1}Y_{0.1}O_3$ series (BCFZY; 1.15 eV)[38] and $BaFe_{0.5}Sn_{0.2}Bi_{0.3}O_3$ (BFSB3; 0.84 eV) (Table 3-2).[39] Hence LSCN8273 cell possesses $R_p$ of 0.09 Ω $cm^2$ at 600 ℃, which is comparable with the smallest value (0.08 Ω $cm^2$) of the PCFC as reported for BCFZY electrodes.[29] These results confirmed that the hydrated LSCN electrodes efficiently extend the reaction areas beyond electrode electrolyte gas TPB due to the enhanced the $H^+/e^-/O^{2-}$ triple conductivity in the intermediate temperatures. The $R_p$ of the LSCN cells is smaller than the BZCY442 electrolyte resistances in the temperature range of 550-700 ℃. Therefore, combining with more-conductive, Ce-rich side BZCY electrolytes leads to simultaneous improvement in lowering operation temperature to less than 600 ℃ and in increasing efficiency in both FC and EC modes.

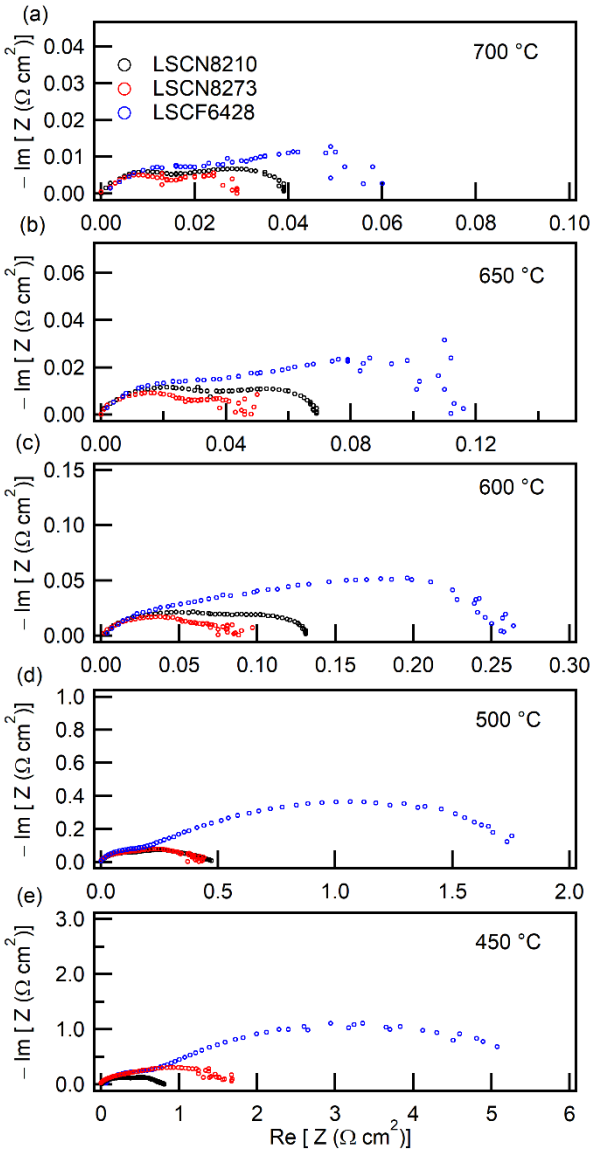


Figure 3-10 Electrochemical impedance spectra of PCFC/ECs with LSCN series as air electrodes at (a) 700 ℃, (b) 650 ℃, (c) 600 ℃ and (d) 500 ℃ under OCV condition.

Table 3-3 Comparison of electrochemical performances of the protonic ceramic cells with various air electrodes at 600 ℃.

| Electrolyte | Air electrode | Electrolysis density at 1.3 V (A $cm^{-2}$) | PPD (W $cm^{-2}$) | $R_p$(Ω $cm^2$) | Ref |
|---|---|---|---|---|---|
| BZCY442 | LSCN8210 | 0.87 | 0.72 | 0.13 | This work |
| BZCY442 | LSCN8273 | 1.09 | 0.88 | 0.09 | This work |
| BZCY442 | LSCF | 0.50 | 0.48 | 0.26 | This work |
| BZCY442 | BSCF | - | 0.28 | 0.74 | 40 |
| BZCY442 | $Pr_2NiO_4$ | - | 0.10 | 0.77 | 41 |
| BZCY442 | BZCY-BSCFT | - | 0.19 | 0.91 | 9 |
| BZCY442 | BSCF | - | 0.23 | - | 42 |
| BZCY442 | BCCY | - | 0.40 | 0.16 | 6 |
| BZCY172 | BFSB3 | - | 0.84 | 0.094 | 39 |
| BZCY352 | SF-BZCY352 | - | 0.37 | 0.35 | 43 |
| BZCYYb4411 | BCFZY | - | 0.648 | 0.08 | 29 |
| BZCYYb4411 | PBSCF | - | 1.065 | 0.14 | 27 |
| BZCYYb4411 | BCCY | - | 0.74 | 0.13 | 6 |
| BZCYYb1711 | SSNCF | - | 0.73 | 0.30 | 44 |
| BZCYYb1711 | NBSCF | | 0.69 | 0.28 | 37 |
| BZCY532 | SEFC-BZCY53 | 0.42 | - | - | 11 |
| BZY82 | SFM-BZY | 0.21 | - | - | 10 |
| BZY91 | LSCF-BZY82 | 0.05 | - | - | 45 |
| BZCYYb4411 | PBSCF | 1.42 | 0.82 | 0.15 | 46 |
| BZCYYb4411(PLD) | PBSCF | 1.92 | - | 0.14 | 46 |
| BZCYYb4411 | LSCF | 0.70 | 0.42 | - | 46 |

| | | | | | |
|---|---|---|---|---|---|
| BZCYYb4411 | LSM | 0.65 | 0.37 | - | 46 |
| BZCYYb1711 | NBSCF-BZCYYb | 0.75 | - | - | 47 |
| BZCYYb1711 | PBSCF | 0.85 | - | - | 48 |

For electrolyte: BZCY442 = $BaZr_{0.4}Ce_{0.4}Y_{0.2}O_3$; BZCY172 = $BaZr_{0.1}Ce_{0.7}Y_{0.2}O_3$; BZCY352 = $BaZr_{0.3}Ce_{0.5}Y_{0.2}O_3$; BZCYYb4411 = $BaZr_{0.4}Ce_{0.4}Y_{0.1}Yb_{0.1}O_3$; BZCYYb1711 = $BaZr_{0.1}Ce_{0.7}Y_{0.1}Yb_{0.1}O_3$; BZCY532 = $BaZr_{0.5}Ce_{0.3}Y_{0.2}O_3$; BZY82 = $BaZr_{0.8}Y_{0.2}O_3$; BZY91 = $BaZr_{0.9}Y_{0.1}O_3$;

For air electrode: C-LSMN7373 = cubic type $La_{0.7}Sr_{0.3}Mn_{0.7}Ni_{0.3}O_3$; BSCF = $Ba_{0.5}Sr_{0.5}Co_{0.5}Fe_{0.5}O_{3-\delta}$; BZCY-BSCFT = $BaZr_{0.4}Ce_{0.4}Y_{0.2}O_3$-$Ba_{0.5}Sr_{0.5}(Co_{0.8}Fe_{0.2})_{0.9}Ti_{0.1}O_{3-\delta}$; BCCY = $BaCo_{0.7}(Ce_{0.8}Y_{0.2})_{0.3}O_{3-\delta}$; BFSB3=$BaFe_{0.5}Sn_{0.2}Bi_{0.3}O_{3-\delta}$; SFO-BZCY352=SrFeO3-$BaZr_{0.3}Ce_{0.5}Y_{0.2}O_3$; BCFZY = $BaCo_{0.4}Fe_{0.4}Zr_{0.1}Y_{0.1}O_{3-\delta}$; PBSCF = $PrBa_{0.5}Sr_{0.5}Co_{1.5}Fe_{0.5}O_{5+\delta}$; SSNCF = $Sr_2Sc_{0.1}Nb_{0.1}Co_{1.5}Fe_{0.3}O_{6-\delta}$; NBSCF = $NdBa_{0.5}Sr_{0.5}Co_{1.5}Fe_{0.5}O_{5+\delta}$;

## 3-4 Conclusions

In summary, LSCN oxides were demonstrated to exhibit bulk proton conduction at intermediate temperature region by pronounced hydration/dehydration reactions with retaining sufficient mole fraction of water under wet air atmosphere in at temperatures below 800 ℃. LSCN8210 and LSCN8273 undergo thermochemical hydration in wet air by the defect association between oxygen vacancy and water molecules with gaining proton carriers of 0.15 and 0.06 mole fraction at around 400 ℃, respectively, which is quite similar to the concentration of the widely-used protonic conducting ceramic $BaCe_{0.9}Y_{0.1}O_3$. The cells comprising LSCN8273 air electrode and BZCY442 electrolyte yielded PPD of 0.65 W $cm^{-2}$ in FC mode and electrolysis current at 1.3V of 0.68 A $cm^{-2}$ in EC mode at 550 ℃, and thus, was demonstrated to have the performances close to the champion data reported for the cells with BZCYYb electrolytes despite using relatively poor-conductive, Zr-rich side electrolytes. The cell with LSCN8273 air electrode has similar polarization resistance (0.09 Ω $cm^2$) at 600 ℃ as the smallest values reported for advanced triple conducting electrodes, and, moreover, the related activation energy is significantly lower than those for the other triple conducting materials. These superior performances of LSCN electrodes verify the extended reaction areas at electrode/electrolyte interfaces due to the enhanced proton conductivity. In conclusion, $La_{0.8}Sr_{0.2}Co_{1-x}Ni_xO_{3-\delta}$ with sufficient protonic conduction are promising air electrodes for protonic ceramic cells operating at intermediate temperatures.

## 3-5 References


1. L. Xu, Q. Jiang, Z. Xiao, X. Li, J. Huo, S. Wang and L. Dai, *Angewandte Chemie International Edition*, 2016, **55**, 5277-5281.
2. S. Dresp, F. Luo, R. Schmack, S. Kühl, M. Gliech and P. Strasser, *Energy & Environmental Science*, 2016, **9**, 2020-2024.
3. S. Park, Y. Shao, J. Liu and Y. Wang, *Energy & Environmental Science*, 2012, **5**, 9331-9344.
4. L. Yang, S. Wang, K. Blinn, M. Liu, Z. Liu, Z. Cheng and M. Liu, *Science*, 2009, **326**, 126-129.
5. M. A. Pellow, C. J. Emmott, C. J. Barnhart and S. M. Benson, *Energy & Environmental Science*, 2015, **8**, 1938-1952.
6. Y. Song, Y. Chen, W. Wang, C. Zhou, Y. Zhong, G. Yang, W. Zhou, M. Liu and Z. Shao, *Joule*, 2019, DOI: 10.1016/j.joule.2019.07.004.
7. T. Kobayashi, K. Kuroda, S. Jeong, H. Kwon, C. Zhu, H. Habazaki and Y. Aoki, *Journal of The Electrochemical Society*, 2018, **165**, F342-F349.
8. S. Li and K. Xie, *Journal of The Electrochemical Society*, 2013, **160**, F224-F233.
9. L. Bi, E. Fabbri and E. Traversa, *Electrochemistry Communications*, 2012, **16**, 37-40.
10. L. Lei, Z. Tao, X. Wang, J. P. Lemmon and F. Chen, *Journal of Materials Chemistry A*, 2017, **5**, 22945-22951.
11. D. Huan, N. Shi, L. Zhang, W. Tan, Y. Xie, W. Wang, C. Xia, R. Peng and Y. Lu, *ACS applied materials & interfaces*, 2018, **10**, 1761-1770.
12. Y. Lin, R. Ran and Z. Shao, *International Journal of Hydrogen Energy*, 2010, **35**, 8281-8288.
13. J. Dailly, S. Fourcade, A. Largeteau, F. Mauvy, J.-C. Grenier and M. Marrony, *Electrochimica Acta*, 2010, **55**, 5847-5853.
14. A. Grimaud, F. Mauvy, J. Bassat, S. Fourcade, L. Rocheron, M. Marrony and J. Grenier, *Journal of The Electrochemical Society*, 2012, **159**, B683-B694.
15. N. Wang, S. Hinokuma, T. Ina, H. Toriumi, M. Katayama, Y. Inada, C. Zhu, H. Habazaki and Y. Aoki, *Chemistry of Materials*, 2019, **31**, 8383-8393.
16. Y. Aoki, E. Tsuji, T. Motohashi, D. Kowalski and H. Habazaki, *The Journal of Physical Chemistry C*, 2018, **122**, 22301-22308.
17. N. Tsvetkov, Q. Lu, L. Sun, E. J. Crumlin and B. Yildiz, *Nat Mater*, 2016, **15**, 1010-1016.
18. N. M. M. Imamura, and H. Shimada, *Journal of Physical Chem B* 2000.
19. D. N. Mueller, M. L. Machala, H. Bluhm and W. C. Chueh, *Nature communications*, 2015, **6**, 6097.
20. B. Gilbert, C. S. Kim, C.L. Dong, J. Guo, P. S. Nico and D. K. Shuh, *AIP Conference Proceedings*, 2007, **882**, 721.
21. I. D. Welsh and P. M. Sherwood, *Physical review. B, Condensed matter*, 1989, **40**,

6386-6392.
22. J. C. Dupin, D. Gonbeau, P. Vinatier and A. Levasseur, *Physical Chemistry Chemical Physics*, 2000, **2**, 1319-1324.
23. M. Yoshida, Y. Mitsutomi, T. Mineo, M. Nagasaka, H. Yuzawa, N. Kosugi and H. Kondoh, *The Journal of Physical Chemistry C*, 2015, **119**, 19279-19286.
24. X. Su, Y. Wang, J. Zhou, S. Gu, J. Li and S. Zhang, *Journal of the American Chemical Society*, 2018, **140**, 11286-11292.
25. D. Drevon, M. Gorlin, P. Chernev, L. Xi, H. Dau and K. M. Lange, *Sci Rep*, 2019, **9**, 1532.
26. R. D. Shannon, *Book*.
27. S. Choi, C. J. Kucharczyk, Y. Liang, X. Zhang, I. Takeuchi, H.-I. Ji and S. M. Haile, *Nature Energy*, 2018, **3**, 202-210.
28. D. Poetzsch, R. Merkle and J. Maier, *Faraday discussions*, 2015, **182**, 129-143.
29. C. Duan, J. Tong, M. Shang, S. Nikodemski, M. Sanders, S. Ricote, A. Almansoori and R. O'Hayre, *Science*, 2015, **349**, 1321-1326.
30. D. Poetzsch, R. Merkle and J. Maier, *Physical Chemistry Chemical Physics*, 2014, **16**, 16446-16453.
31. I. K. Andersen, E. K. Andersen, P. Norby and E. Skou, *Journal of Solid State Chemistry*, 1994, **113**, 320-326.
32. L. Bi, S. P. Shafi and E. Traversa, *Journal of Materials Chemistry A*, 2015, **3**, 5815-5819.
33. Y. Gan, J. Zhang, Y. Li, S. Li, K. Xie and J. T. S. Irvine, *Journal of The Electrochemical Society*, 2012, **159**, F763-F767.
34. F. He, D. Song, R. Peng, G. Meng and S. Yang, *Journal of Power Sources*, 2010, **195**, 3359-3364.
35. R. Wang, C. Byrne and M. C. Tucker, *Solid State Ionics*, 2019, **332**, 25-33.
36. Y. Xia, Z. Jin, H. Wang, Z. Gong, H. Lv, R. Peng, W. Liu and L. Bi, *Journal of Materials Chemistry A*, 2019, **7**, 16136-16148.
37. J. Kim, S. Sengodan, G. Kwon, D. Ding, J. Shin, M. Liu and G. Kim, *ChemSusChem*, 2014, **7**, 2811-2815.
38. R. Ren, Z. Wang, C. Xu, W. Sun, J. Qiao, D. W. Rooney and K. Sun, *Journal of Materials Chemistry A*, 2019, **7**, 18365-18372.
39. Y. Xia, Z. Jin, H. Wang, Z. Gong, H. Lv, R. Peng, W. Liu and L. Bi, *Journal of Materials Chemistry A*, 2019, **7**, 16136-16148..
40. Y. Liu, Y. Guo, R. Ran and Z. Shao, *Journal of Membrane Science*, 2013, **437**, 189-195.
41. N. Nasani, D. Ramasamy, S. Mikhalev, A. V. Kovalevsky and D. P. Fagg, *Journal of Power Sources*, 2015, **278**, 582-589.
42. Y. Guo, Y. Lin, R. Ran and Z. Shao, *Journal of Power Sources*, 2009, **193**, 400-407.
43. Z. Wang, W. Yang, S. P. Shafi, L. Bi, Z. Wang, R. Peng, C. Xia, W. Liu and Y. Lu,

*Journal of Materials Chemistry A*, 2015, **3**, 8405-8412.
44. C. Zhou, J. Sunarso, Y. Song, J. Dai, J. Zhang, B. Gu, W. Zhou and Z. Shao, *Journal of Materials Chemistry A*, 2019, **7**, 13265-13274.
45. L. Bi, S. P. Shafi and E. Traversa, *Journal of Materials Chemistry A*, 2015, **3**, 5815-5819.
46. S. Choi, T. C. Davenport and S. M. Haile, *Energy & Environmental Science*, 2019, **12**, 206-215.
47. J. Kim, A. Jun, O. Gwon, S. Yoo, M. Liu, J. Shin, T.-H. Lim and G. Kim, *Nano Energy*, 2018, **44**, 121-126.
48. W. Wu, H. Ding, Y. Zhang, Y. Ding, P. Katiyar, P. K. Majumdar, T. He and D. Ding, *Advanced science*, 2018, **5**, 1800360.

# Chapter 4 Incorporation of bulk proton carriers in cubic perovskite manganite driven by interplays of oxygen and manganese redox

## 4-1 Introduction

As already mentioned in Chapter 1, it's highly motivated to develop single-phase mixed $H^+/O^{2-}/e^-$ triple conductors in order to eliminate the mismatch of main ionic carriers between the double conducting air electrode and the electrolyte and thus, extend the reaction area at the air electrode.[1-3] As described in Chapter 1-8, the proton defect concentrations of the current triple conductors are still low in comparison to the well-known proton conductor Ba(Ce, Zr, Y)$O_3$.[4,5,6] In general, incorporation of protonic defects in oxides is driven via association between oxygen vacancy and water molecules.

$La_{1-x}Sr_xMnO_3$ (LSM) is a well-known cathode material for solid oxide fuel cells however, Rhombohedra LSM was recognized as a bad cathode for them at elevated temperatures,[5,7,8] and it has not been subject to a proton conducting material. This chapter describes the discovery of the pronounced hydration capability in cubic perovskite type $La_{0.7}Sr_{0.3}MnO_{3-\delta}$, mediated by the charge disproportionation between oxygen and manganese atoms. $La_{0.7}Sr_{0.3}MnO_{3-\delta}$ undergoes decline of antibonding O *2p* states hybridized with Mn *3d* orbitals together with oxidation of $Mn^{3+}$ to $Mn^{4+}$ through the hydration, subsequently protons attach to oxygen. Hence $La_{0.7}Sr_{0.3}MnO_{3-\delta}$ is capable of up-taking bulk proton carriers in wet air with the proton concentrations equaling to that of well-known protonic electrolyte material Ba(Zr, Ce, Y)$O_3$ at the intermediate temperature (IT) region.

## 4-2 Experimental section

### 4-2-1 Synthesis of LSM

$La_{1-x}Sr_xMnO_{3-\delta}$ (LSM; $x$ = 0.1, 0.2, 0.3, 0.4) fine powders were synthesized via a citrate precursor route reported elsewhere.[8] Firstly, $La(NO_3)_3•6H_2O$, $Sr(NO_3)_2$, and $Mn(NO_3)_2•6H_2O$ (all from High Purity Chemicals and at 99.99%) in amounts corresponding to the desired stoichiometry (calculated from total 0.05 mole LSM) were completely dissolved into Milli-Q $H_2O$, and then citric acid (CA; $C_6H_8O_7•H_2O$) was added as a chelating agent in a mole ratio of CA:LSM = 2:1. Next, the citrate solution was heated with vigorous stirring at 60 ℃ for 2 h to evaporate the water and promote polymerization. The obtained gelatinous product was calcinated at 500 °C for 1 h under air to produce a black-colored precursor. Finally, the precursor was annealed in a tube furnace at 700, 800, or 1000 ℃ for 15 h under pure $O_2$ atmosphere (15 mL $min^{-1}$).

### 4-2-2 Characterizations

#### (a) Structural characterizations

XRD and SEM were carried out for the phase impurity and microstructure of LSM oxides, the measurement conditions were detailed described in Chapter 3-2-3. Brunauer-Emmett-Teller (BET) analysis (Microtrackbel BELSORP Mini-II) was performed to measure the surface area of LSM powders. Fourier transform infrared (FT-IR) spectroscopy was conducted in diffuse-reflectance mode utilising a JASCO FT/IR-350 spectrometer. LSM powder was sealed in a gas-sealed optical cell with an antireflective glass window under controlled atmospheric and thermal conditions to perform *in-situ* FT-IR measurements.

#### (b) Rietveld structure refinement

The obtained XRD patterns were refined by the Rietveld method using the Materials

Studio software over the $2\theta$ range of 20-80° to precisely determine the phase structure of LSM oxides annealed at different temperatures.

**(c) Thermodynamic characterizations for hydration**

The TG measurements for possibility of hydration and hydration ability cycles were performed by the same techniques mentioned in Chapter 3-2-3, but slightly difference in measuring conditions. Besides the former mentioned conditions in Chapter 3-2-3, Ar gas and wet gases (air, Ar) with various water partial pressure ($p_{H2O}$) were used to characterize hydration ability of LSM. Here, Ar gas with added $O_2$ (10 ppm) was used as a dry Ar gas without further purification, wet gases were prepared by bubbling them through a water bath at -8, 5 and 20 °C at a flow rate of 50 sccm; the resultant gases had a water partial pressure ($p_{H2O}$) of 0.003, 0.009 and 0.023 $p_0$ ($p_0$ = 101.3 kPa).

Thermal desorption spectroscopy (TDS) analysis was performed for as-prepared specimens using an ultra-high vacuum chamber system (ESCO TDS1400) equipped with a quadruple mass analyzer and infrared lamp heater. The spectra were recorded during heating from 50 to 1000 °C at 30 °C $min^{-1}$ under the initial pressure of $2.0 \times 10^{-7}$ Torr. Prior to the measurement, the samples were dried in oven at 120 ℃ overnight.

**(d) Single crystal X-ray absorption spectroscopy**

*In-situ* extended X-ray absorption fine structure (EXAFS) for the Mn K-edge was obtained on the BL01B1 station of Spring-8 facility, Japan Synchrotron Radiation Research Institute (JASRI). The sample placed in a temperature- and atmosphere-controllable cell was heated to 415 °C at a heating rate of 10 °C $min^{-1}$ in dry air ($He/O_2$ = 4/1 (v/v), flow rate: 50 mL/min). A Si (111) double-crystal monochromator was used. The incident and transmitted X-rays were monitored in ionization chambers filled with $N_2$ and 85% $N_2$ + 15% Ar. Quick EXAFS in the continuous scanning mode was recorded from 6520 to 6600 eV (5 min $scan^{-1}$). All samples were mixed with boron

nitride (BN) powder to achieve an appropriate absorbance at the edge energy. The weight ratio of sample and BN is about 1:10. The EXAFS data were processed using the IFEFFIT software package (Athena and Artemis).

O K-edge X-ray absorption spectra (XAS) were obtained at beamline BL-2 of Ritsumeikan University SR Center (Shiga, Japan). Here, measurements were conducted on the dehydrated and hydrated LSM specimens that were prepared by heating at 430 ℃ for 6 h in dry and wet air, respectively. Subsequently, the specimens were sealed in a specially designed transfer vessel without exposure to ambient atmosphere and then supplied to the high vacuum sample chamber of BL-2. All procedures from heating to sealing were conducted in Ar-filled glove box. The XAS data were obtained in the partial fluorescence X-ray yield (PFY) mode with a silicon drift detector (KETEK, VITUSR100 with a 0.1 mm thick Parylene-N film window), because the PFY mode is more bulk-sensitive than the total electron yield (TEY) mode.

## 4-3 Results

### 4-3-1 Preparation of LSM

Figure 4-1a shows XRD patterns of $La_{1-x}Sr_xMnO_{3-\delta}$($x$ = 0.1, 0.2, 0.3, and 0.4; LSM), denoted hereafter as LSM91, LSM82, LSM73, and LSM64, respectively according to the La/Sr mole ratios. For LSM91, LSM82, and LSM73, annealing at 700 ℃ for 15 h in pure $O_2$ result in a single cubic-type perovskite phase, as checked by XRD Rietveld analysis. The LSM specimens thus prepared show only a single intensive peak in the 2θ range of 31–34°, so that these would be identical to cubic or orthorhombic structure rather than rhombohedral one involving two distinct peaks in the 2θ region (Figure 4-1b). Rietveld refinement was performed for the LSM series prepared at 700 ℃ with the cubic (*Pm-3m*), orthorhombic (*Pnma*) and rhombohedral (*R-3c*) $LaMnO_3$ structure model.[9-11] For these, the best fitting is obtained with cubic structure model with the minimized Rietveld parameter ($R_{wp}$) values (Figure 4-2, 4-3 and Table 4-1), confirming that the LSM prepared at 700 ℃ is analogous to cubic perovskite phase. These are denoted hereafter with the prefix of '*C*-' (e.g. *C*-LSM91) to identify their cubic structure. The relatively broad XRD peaks of the cubic phase are attributed to the relatively small grain sizes (Figure 4-4), with the values of LSM91, LSM82 and LSM73 equaling 30 nm, 19 nm, and 27 nm, respectively.

LSM91 and LSM82 retain cubic structure even after annealing at 1000 ℃, whereas LSM73 becomes rhombohedral phase by annealing at 1000 ℃. The LSM73 prepared at 1000 ℃ exhibited a split in the main peak at round 32º, which is attributed to the transformation to rhombohedral phase (PDF-70-3942; Figure 4-1b), and thus shows two intense peaks at around 31.98 and 32.21° corresponding to the (110) and (104) planes (Figure 4-1b), respectively. The best fitting of Rietveld refinement is obtained with rhombohedral space group (R-3c, 167; Figure 4-3d), confirming that a single rhombohedral phase (*R*-LSM73) is available.

The phase stability of $La_{1-x}Sr_xMnO_3$ systems is sensitive to oxygen stoichiometry,[12-14] and thus, they tend to take different crystal structure depending on the preparation roots.[12] Wang et al reported that $La_{1-}Sr_xMnO_3$ ($x$=0.3) prepared by modified polymer complex method and post-annealing at 750 ℃ take cubic phase and transform to orthorhombic phase by post-annealing at 850 ℃,[9] however, Anderson et al reported that $La_{1-x}Sr_xMnO_3$ ($0.0 \leq x < 0.2$) prepared by wet chemical methods and post annealing at 900 ℃ in $N_2$ crystallize orthorhombic phase.[14] Rietveld refinement unambiguously demonstrates that LSM members prepared here take cubic structure with annealing at 700 ℃ and LSM73 rhombohedral with annealing at 1000 ℃. Unfortunately, LSM64 yielded only a small amount of secondary phase $Sr_{1.5}La_{0.5}MnO_4$ under the preparation conditions tested here, and thus further characterization was not applied for this composition.

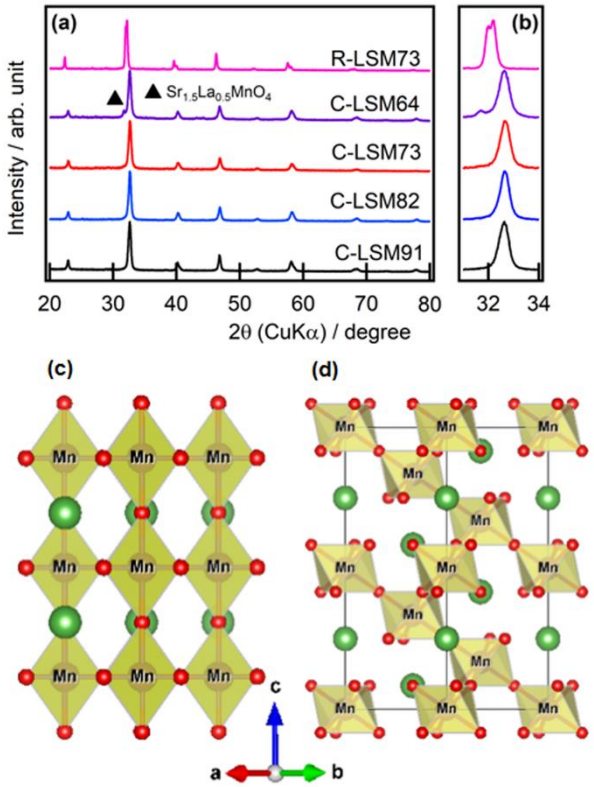


Figure 4-1 (a) XRD patterns of cubic- and rhombohedral-type $La_{1-x}Sr_xMnO_{3-\delta}$ ($x$ = 0.1, 0.2, 0.3, and 0.4). (b) Expansion of (110) peaks for the cubic phase, and (110) and (104) peaks for the rhombohedral phase from 31° to 34°. Ball-and-stick models of (c) cubic and (d) rhombohedral $LaMnO_3$.

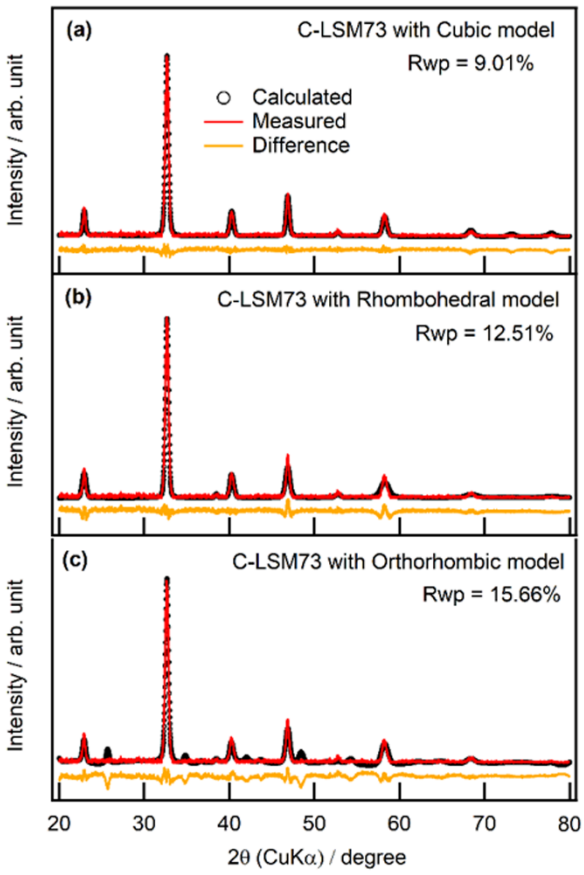


Figure 4-2 Rietveld refinement profiles for *C*-LSM73 assuming models of (a) cubic (*Pm-3m*, #221), (b) rhombohedral (*R-3c*, #167) and (c) orthorhombic (*P4ma*, #62).

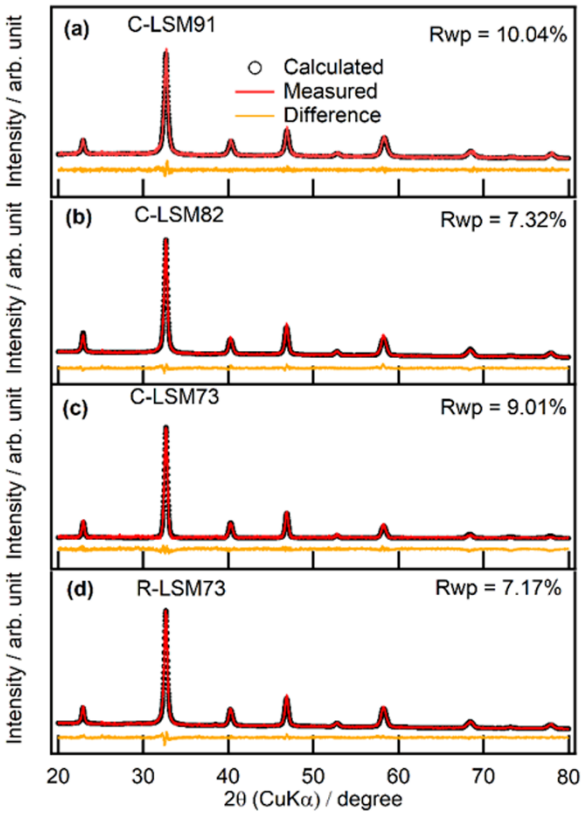


Figure 4-3 Rietveld refinement profiles for (a) *C*-LSM91, (b) *C*-LSM82 and (c) *C*-LSM73 assuming models of cubic structure (*Pm-3m*, #221), and (d) *R*-LSM73 assuming models of rhombohedral (*R-3c*, #167).

Table 4-1 Refined lattice parameters for LSM materials.

| *Samples* | Space group | Lattice Parameters (Å) | | | | | | Reliability |
|---|---|---|---|---|---|---|---|---|
| | | *a* | *b* | *c* | *α* | *β* | *γ* | ($R_{wp}$%) |
| *C*-PDF# 75-0440 | Pm-3m | 3.88 | 3.88 | 3.88 | 90 | 90 | 90 | - |
| *R*-PDF#70-3942 | R-3c | 5.531 | 5.531 | 13.363 | 90 | 90 | 120 | - |
| *O*-PDF#72-0841 | Pnma | 5.742 | 7.668 | 5.532 | 90 | 90 | 90 | - |
| *C*-LSM91 | Pm-3m | 3.880 | 3.880 | 3.880 | 90 | 90 | 90 | 10.04 |
| *C*-LSM82 | Pm-3m | 3.878 | 3.878 | 3.878 | 90 | 90 | 90 | 7.32 |
| *C*-LSM73 | Pm-3m | 3.875 | 3.875 | 3.875 | 90 | 90 | 90 | 9.01 |
| *R*-LSM73 | R-3c | 5.567 | 5.567 | 13.610 | 90 | 90 | 120 | 7.17 |
| *C*-LSM73 | R-3c | 5.497 | 5.497 | 13.367 | 90 | 90 | 120 | 12.51 |
| *C*-LSM73 | Pnma | 5.465 | 7.747 | 5.505 | 90 | 90 | 90 | 15.66 |

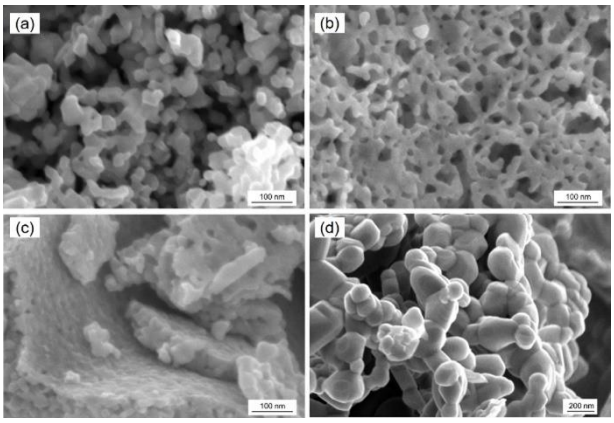


Figure 4-4 SEM images of *C*-LSM91 (a), *C*-LSM82 (b), *C*-LSM73 (c), and *R*-LSM73 (d) with grain size 30 nm, 19 nm, 27 nm, and 162 nm, respectively.

### 4-3-2 Hydration/dehydration reactions of LSM

Figures 4-5a-c show thermogravimetric (TG) curves of the *C*-LSM samples, measured mainly in dry and wet Ar gases with $O_2$ additive at 10 ppm. (In the discussion hereafter, the 'Ar gases' all include 10 ppm $O_2$.) The TG profiles of *C*-LSM91 (Figure 4-5a) and *C*-LSM82 (Figure 4-5b) in dry Ar are similar to each other, revealing a mass loss at $T < 200$ ℃ due to desorption of surface $H_2O$ and mass losses at $T > 700$ ℃ probably due to oxygen release with the reduction of $Mn^{4+}$ to $Mn^{3+}$.[15] The TG curves are also similar either in wet or dry conditions, indicating that they are inert to water vapor at elevated temperature.

The profiles of *C*-LSM73 (Figures 4-5c) are comparatively quite different. In addition to the desorption of surface water at $T < 200$ ℃ and oxygen release at $T >$ 700 ℃, a mass loss of about 0.5 wt% occurs at around 350 and 430 ℃ in dry and wet Ar, respectively. There is also a subsequent thermogravimetric plateau from about 400 to 700 ℃ due to the formation of thermochemically stable phase. The BET surface area of *C*-LSM73 (18.6 $m^2\ g^{-1}$) is quite similar to those of *C*-LSM91 and *C*-LSM82 (20.3 and 26.5 $m^2\ g^{-1}$, respectively), and therefore the mass loss at around 400 ℃ can be related to the bulk reaction rather than surface desorption. The weight losing onset temperature under the wet condition (430 ℃) is clearly higher than that under the dry condition (350 ℃), indicating that the mass losses are related to thermochemical reactions with water vapor. On the other hand, this event is not sensitive to the oxygen partial pressure ($p_{O2}$): the mass loss starts at 350 ℃ in dry air and at 430 ℃ in wet air, which are the same as the values in dry and wet Ar, respectively (Figure 4-5d). *R*-LSM73 exhibits small weight loss at around 430 ℃ in wet air and at 350 ℃ in dry air (Figure 4-5e).

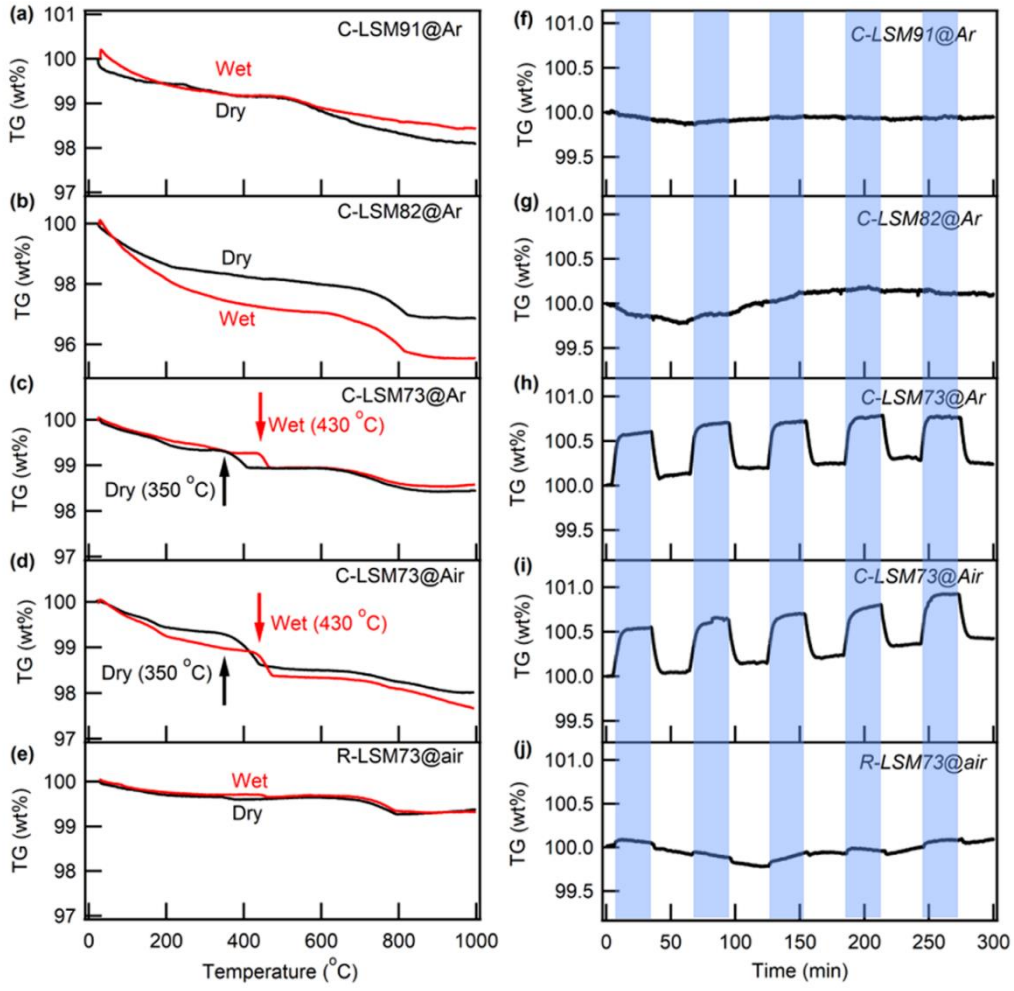


Figure 4-5 TG curves of (a) *C*-LSM91, (b) *C*-LSM82, (c) *C*-LSM73, and (e) *R*-LSM73 measured in the range from RT to 1000 ℃ in dry and wet Ar atmosphere (10 ppm $O_2$). $p_{H2O}$ of the wet gas is 0.023 $p_0$. (d) TG curves of *C*-LSM73 measured in dry and wet air. The weight gain/loss in response to atmospheric switching between wet/dry Ar every 30 mins for (f) *C*-LSM91, (g) *C*-LSM82, (h) *C*-LSM73, and (j) *R*-LSM73. (i) Weight gain/loss in response to atmospheric switching between wet/dry air every 30 mins for *C*-LSM73. In (f)-(j), pale blue areas represent the durations of wet atmosphere.

To elucidate the released gases, thermal desorption spectroscopy (TDS) was performed for *C*-LSM91, *C*-LSM73 and *R*-LSM73 (Figure 4-6a). *C*-LSM73 exhibits an intensive desorption peak of $H_2O$ (*m/z* = 18) at around 300-500 ℃ after the desorption of surface-adsorbed water in the range below 200 ºC, and a flat profile of $O_2$ (*m/z* = 32) in the range below 600 ℃. *C*-LSM91 does not exhibit any desorption peak of $H_2O$ at temperatures above 200 ℃. High-temperature XRD data confirms that *C*-LSM73 retains the cubic-type perovskite structure before and after the mass losses at around 400 ℃ (Figure 4-7). These findings unambiguously demonstrate that *C*-LSM73 undergoes an isostructural dehydration reaction at around 400 ℃. *R*-LSM73 has a relatively small water desorption peak at intermediate temperature (Figure 4-6a), which is in agreement with very small weight loss (0.054 % in Ar) at around 415 ℃ (Figure 4-5j). *R*-LSM73 is weakly hydrated in comparison to *C*-LSM73.

*In-situ* infrared absorption spectroscopy (IR) highlights the enhanced hydration behavior of *C*-LSM73. The O–H vibration modes are developed in the wavenumber range of 3100 to 3500 $cm^{-1}$ as exposed to wet air ($p_{H2O}$ = 0.023 $p_0$), in which a strong peak appears at 3240 $cm^{-1}$ and two broad peaks at 3170 and 3380 $cm^{-1}$ (Figure 4-6b). These features are in agreement with vibration bands of O–H groups incorporating into oxygen vacancies of $BaZr_{0.8}Y_{0.2}O_3$; the vibration modes split in concerned with various local coordination environment of the O site.[16,17] These results demonstrate that *C*-LSM73 causes bulk hydration via association of water and oxygen vacancy under wet atmosphere at around 400 ℃. *R*-LSM73 and *C*-LSM91 show a quite small absorption of O–H groups at around 3200 $cm^{-1}$ (Figure 4-6c and d) even after exposure to wet gases, indicting the less pronounced hydration ability.

Actually, *C*-LSM73 was found to undergo reversible hydration/dehydration reactions in response to $p_{H2O}$ at around 400 ℃. At the fixed temperature of 415 ℃, mass changes were monitored for repeated cycles of atmospheric switching between dry and wet Ar (10 ppm $O_2$) every 30 mins (Figure 4-5h). At the same time, the weights of *C*-LSM91

and *C*-LSM82 remain unchanged throughout these cycles (Figure 4-5 f and g), which is consistent with their TG profiles (Figures 4-5a and b) and confirms that both are incapable of up-taking and releasing water at around 400 ℃.

*C*-LSM73 has reversible mass changes by dry/wet switching in both Ar and air atmospheres (Figures 4-5h and i), with a mass gain of about 0.5 wt% upon exposure to wet gases ($p_{H2O}$=0.023 $p_0$) and an equal mass loss when exposed to dry gases. Apparently, *C*-LSM73 does not change its mass in response to $p_{O2}$ by switching between air and Ar, either in the dry or wet conditions (Figure 4-8), which confirms that the oxide does not conduct reversibly uptake/release oxygen at around 400 °C. The hydration/dehydration behaviors are completely repeatable, because the mass loss during dehydration and mass gain during hydration agree within 10%. These combined results prove that *C*-LSM73 is capable of reversible water uptake/release in the intermediate temperature range, mediated by bulk proton conduction. In Figures 4-5h and i, the mass changes decayed quickly during the dry/wet switching, reaching equilibria within a few minutes, which provides clear evidence for the significant bulk proton conductivity of *C*-LSM73 in the IT region. Here, the weight variable ($\Delta W$) is defined as the mean weight difference between the samples equilibrated in dry and wet conditions for 5 switching cycles. For *C*-LSM73, $\Delta W$ is equal to 0.56 and 0.51 wt% in air and Ar, respectively (Table 4-2) under $p_{H2O}$ = 0.023 $p_0$. $\Delta W$ of *R*-LSM73 is 0.054 wt% (Table 4-2 and Figure 4-5j), confirming that amount of water sorbate of *R*-LSM73 is much smaller than that of *C*-LSM73.

The dehydration onset temperature of *C*-LSM73 is clearly dependent on $p_{H2O}$ (Figure 4-9). It shifts from 350 to 401 to 410 to 430 ℃ (Figure 4-9a) with switching from dry to $p_{H2O}$ = 0.003 to 0.009 to 0.023 $p_0$. $\Delta W$, moreover, decreases from 0.56 wt% to 0.32 wt% to 0.18 wt% with decreasing $p_{H2O}$ from 0.023 to 0.009 to 0.003 in wet air (Figure 4-9b). These features prove that hydration/dehydration reactions of *C*-LSM73 thermochemically undergo.

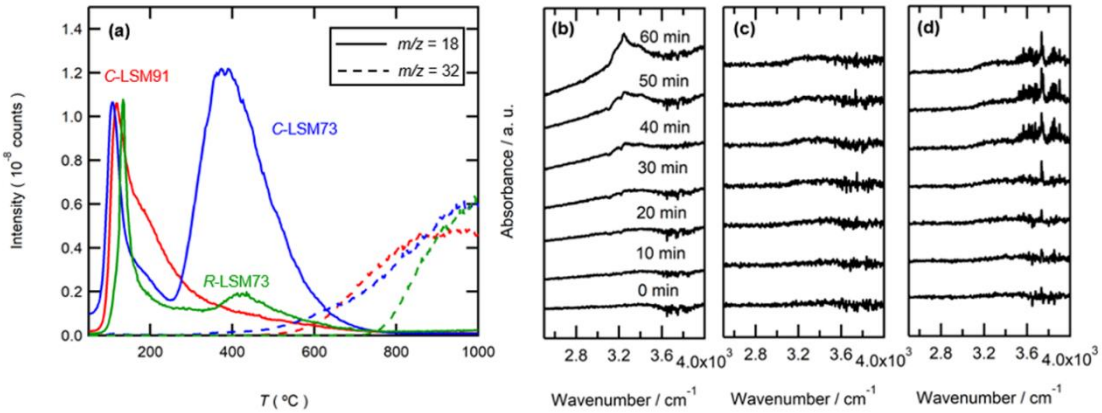


Figure 4-6 (a) TDS of water (*m/z* = 18) and $O_2$ (*m/z*=32) for *C*-LSM91, *C*-LSM73, and *R*-LSM73. *In situ* IR spectra of (b) *C*-LSM73, (c) *R*-LSM73 and (d) *C*-LSM91 during exposure to wet air ($p_{H2O} = 0.023\ p_0$) at 415 ℃. In all cases, the IR spectra were recorded every 10 mins.

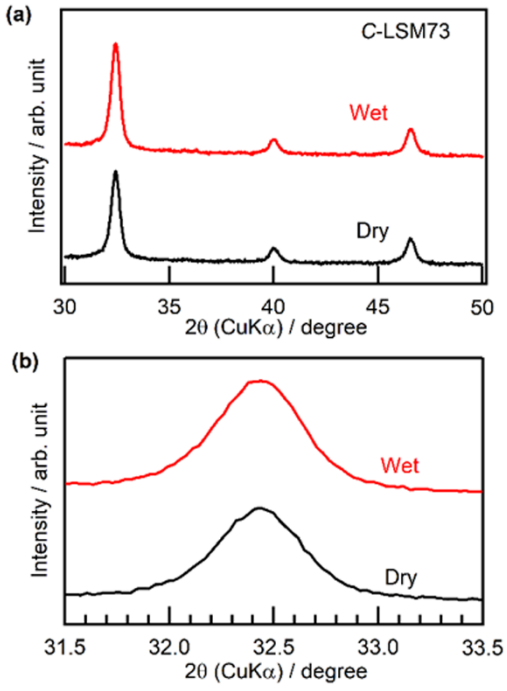


Figure 4-7 (a) High temperature XRD patterns of *C*-LSM73 at 415 ℃ under dry and wet Ar. (b) Expansion of (110) peaks for cubic phase.

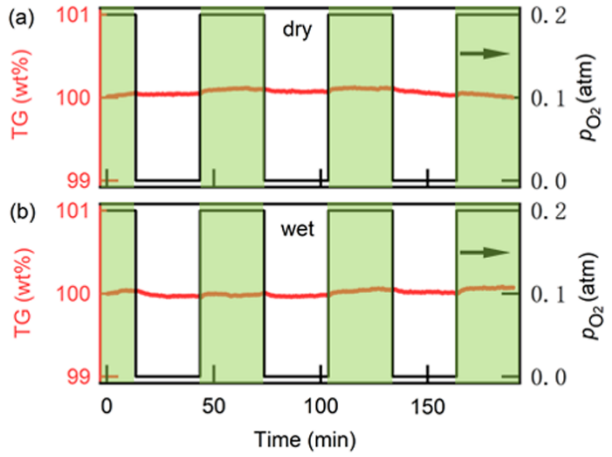


Figure 4-8 The weight gain and loss in response to atmospheric switching between Ar (50 mL/min; 10 ppm $O_2$) and air (10 ml/min $O_2$ and 40 mL/min Ar) every 30 mins at 415 ℃ in (a) dry and (b) wet conditions for *C*-LSM73.

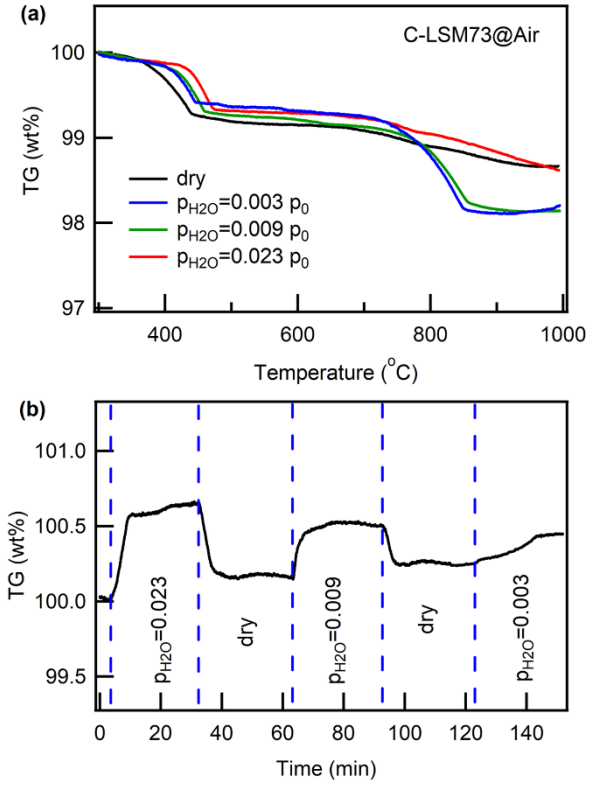


Figure 4-9 (a) TG curves of *C*-LSM73 under wet air atmosphere with different $p_{H2O}$. Here, '100 wt%' of the TG curves was took at the weight at 300 °C for the comparison. (b) Weight gain/loss in response to atmospheric switching between wet/dry air every 30 mins for *C*-LSM73 with different $p_{H2O}$.

Table 4-2 Hydration properties of *C*-LSM73 and other triple conductors.

| Systems | ΔW (wt%) | Δ*n* * | Proton concentration* | Temperature (℃) | $p_{H2O}$ / $p_0$ | Ref. |
|---|---|---|---|---|---|---|
| *C*-$La_{0.7}Sr_{0.3}MnO_{2.95}$ | 0.56 (air)<br>0.51 (Ar) | 0.070 (air)<br>0.064 (Ar) | 0.142 (air)<br>0.128 (Ar) | 415 | 0.023 | This work |
| *C*-$La_{0.7}Sr_{0.3}MnO_{2.95}$ | 0.32 (air) | 0.041 (air) | 0.082 (air) | 415 | 0.009 | This work |
| *C*-$La_{0.7}Sr_{0.3}MnO_{2.95}$ | 0.18 (air) | 0.023 (air) | 0.046 (air) | 415 | 0.003 | This work |
| *R*-$La_{0.7}Sr_{0.3}MnO_{2.98}$ | 0.054 (Ar) | 0.007 (Ar) | 0.014 (Ar) | 415 | 0.023 | This work |
| $PrBa_{0.5}Sr_{0.5}Co_{1.5}Fe_{0.5}O_{5+\delta}$ | - | 0.018 | 0.036 | 200 | 0.02 | 6 |
| $Ba_{0.95}La_{0.05}Fe_{0.8}Zn_{0.2}O_{3-\delta}$ | - | 0.050 | 0.10 | 200 | 0.016 | 18 |
| $BaCo_{0.4}Fe_{0.4}Zr_{0.2}O_{3-\delta}$ | - | - | 0.015-0.05 | 200-400 | 0.015 | 19 |
| $Ba_{0.5}Sr_{0.5}Fe_{0.8}Zn_{0.2}O_{3-\delta}$ | | - | 0.015 | 350 | 0.02 | 20 |
| $Ba_{0.5}Sr_{0.5}Fe_{0.8}Zn_{0.2}O_{3-\delta}$ | - | - | 0.02 | 400 | 0.02 | 20 |
| $Ba_{0.5}Sr_{0.5}Fe_{0.8}Zn_{0.2}O_{3-\delta}$ | - | - | 0.013-0.032 | 350-600 | 0.02 | 20 |
| $PrBa_{0.5}Sr_{0.5}Co_{1.5}Fe_{0.5}O_{5+\delta}$ | - | 0.009 | 0.018 | 600 | 0.02 | 6 |
| $Ba_{0.95}La_{0.05}Fe_{0.8}Zn_{0.2}O_{3-\delta}$ | - | 0.023 | 0.056 | 400 | 0.016 | 18 |
| $Ba_{0.95}La_{0.05}Fe_{0.8}Zn_{0.2}O_{3-\delta}$ | - | 0.012 | 0.024 | 500 | 0.016 | 18 |
| $BaCo_{0.4}Fe_{0.4}Zr_{0.1}Y_{0.1}O_{3-\delta}$ | - | 0.095 | 0.019 | 500 | 0.0095 | 4 |

* Represented by mole fraction.

### 4-3-3 Iodometry of dehydrated LSM

The oxidation states of Mn cations in LSM altogether with $LaMnO_3$ and $CaMnO_3$ references were determined by iodometry. For the analysis, all powder specimens were once annealed in dry air at 430 °C for 6 h, quenched in dry air and immediately dissolve into 0.1 mole HCl solutions. Average valence states of Mn cations in $LaMnO_3$ and $CaMnO_3$ were determined to +3.20 and +3.99, respectively, thereby, the nominal composition of both at 430°C equaling to $LaMnO_{3.10}$ and $CaMnO_{3.00}$. The value of $LaMnO_3$ are in close agreement with the results ($LaMnO_{3.15}$ at 400°C) reported by Mizusaki.[21] Valence states of Mn in *C*-LSM73, *C*-LSM82, *C*-LSM91 and *R*-LSM73 are +3.26, +3.28, +3.34 and +3.34, respectively, and thus the corresponding stoichiometries are expresses as *C*-$La_{0.7}Sr_{0.3}MnO_{2.98}$, *C*-$La_{0.8}Sr_{0.2}MnO_{3.04}$, *C*-$La_{0.9}Sr_{0.1}MnO_{3.12}$ and *R*-$La_{0.7}Sr_{0.3}MnO_{3.02}$, respectively, which are in agreement with the analytical results reported by Mizusaki.[21] Most of LSM members prepared here include apparent oxygen excesses. $La_xSr_{1-x}MnO_3$ system thermodynamically favors to create cation vacancies, such as $V_{La}'''$ and $V_{Mn}'''$, rather than oxygen vacancies,[21-24] and thus tend to decompose with increasing the oxygen deficiencies to more than 0.13.[21] that possess less-pronounced hydration ability.

Meanwhile, only *C*-LSM73 includes oxygen deficiency and, moreover, this can exhibit enhanced hydration ability unlike the other LSM members. This feature proves that the hydration reaction undergoes mediated via oxygen vacancies. If the molecular formula of dehydrated *C*-LSM73 is assumed to be $La_{0.7}Sr_{0.3}MnO_{2.98}$ as determined by iodometry (Figure 4-10), its hydration capability ($\Delta n$, defined by the mole fractions of water absorbed, $n(H_2O)$, i.e. $\Delta n = n(H_2O)/n(\text{LSM73})$) can be calculated from the $\Delta W$ values listed in Table 4-2. For *C*-LSM73, $\Delta n$ = 7.1 and 6.4 mol% in Ar and air atmospheres, respectively. The corresponding proton concentrations are 14.2 and 12.8 mol% in air and Ar (10 ppm $O_2$), respectively (Table 4-2).

### 4-3-4 Mn *K*-edge EXAFS

Extended X-ray absorption fine structure (EXAFS) analysis was conducted on the Mn K-edge for LSM, together with reference samples of $LaMnO_3$ and $CaMnO_3$. Figure 2-10a presents normalized absorption in the X-ray absorption near edge spectroscopy (XANES) region measured at 415 °C in dry air. All LSM samples exhibit a pre-edge peak at around 6540 eV attributed to the electric dipole-forbidden transition of *1s* electron to an unoccupied *3d* orbital, which is partially allowed because of electric quadrupole coupling and/or *3d-4p* orbital mixing arising from the non-centrosymmetric environment of the slightly distorted $MnO_6$ octahedral framework.[25] The relatively weak pre-edge features of LSM series are characteristic of octahedrally coordinated Mn oxides.[26]

After the pre-edge, all samples yield a vertically rising main edge with a maximum peak at around 6553 eV, corresponding to electron transition from *1s* to *4p* orbitals.[25-27] For K-edge XANES of octahedrally-coordinated manganese oxides, the absorption edge position is more sensitive to valence state rather than $MnO_6$ octahedral coordination symmetry, and the absorption edge shifts to higher energy in proportion to the average Mn valence states, since the core electron binding energy linearly increases with the positive charges on the cations.[28,29] Hence, a relative shift in the position of these features, called the chemical shift, allows one to determine the average Mn valence states of the oxides.[30-32] Here, the absorption edge is defined as the energy corresponding to half of maximum of the main absorption peak. The adsorption edges of LSM series locate between ones of two references, *i.e.* $LaMnO_3$ and $CaMnO_3$ (6550.07 and 65552.82 eV, respectively; Figure 4-10a), confirming that Mn valence state of LSM is between +3.20 and +3.99. Thus, the average Mn valence state of LSM series is determined by interpolating to the calibration line connecting $LaMnO_3$ (+3.20) and $CaMnO_3$ (+3.99; Figure 4-11), which results in valence state equaling to +3.27, +3.20, and +3.20 for *C*-LSM91, *C*-LSM82, and *C*-LSM73, respectively (Figure 4-10c

and Table 4-3), which is accordant with the reports elsewhere.[33, 34] The small gap (0.06) in the Mn valence state determined by Mn K-edge and iodometry confirms that the chemical shifts of Mn K-edge can properly probe the valence state of Mn atoms for all LSM (Figure 4-10c).

Oxygen stoichiometry ($3+\delta$) of dehydrated $La_{1-x}Sr_xMnO_{3+\delta}$ is calculated from the average Mn valence state determined by Mn K-edge, assuming that the stoichiometry of metal cations is the same as in the raw materials, and the valences of Sr, La and O are fixed at +2 +3 and -2, respectively (Figure 4-10d and Table 4-3). Although the main edge of *R*-LSM73 is located at a higher energy than in *C*-LSM73, the former is estimated to have a small amount of oxygen deficiency ($\delta = -0.02$).

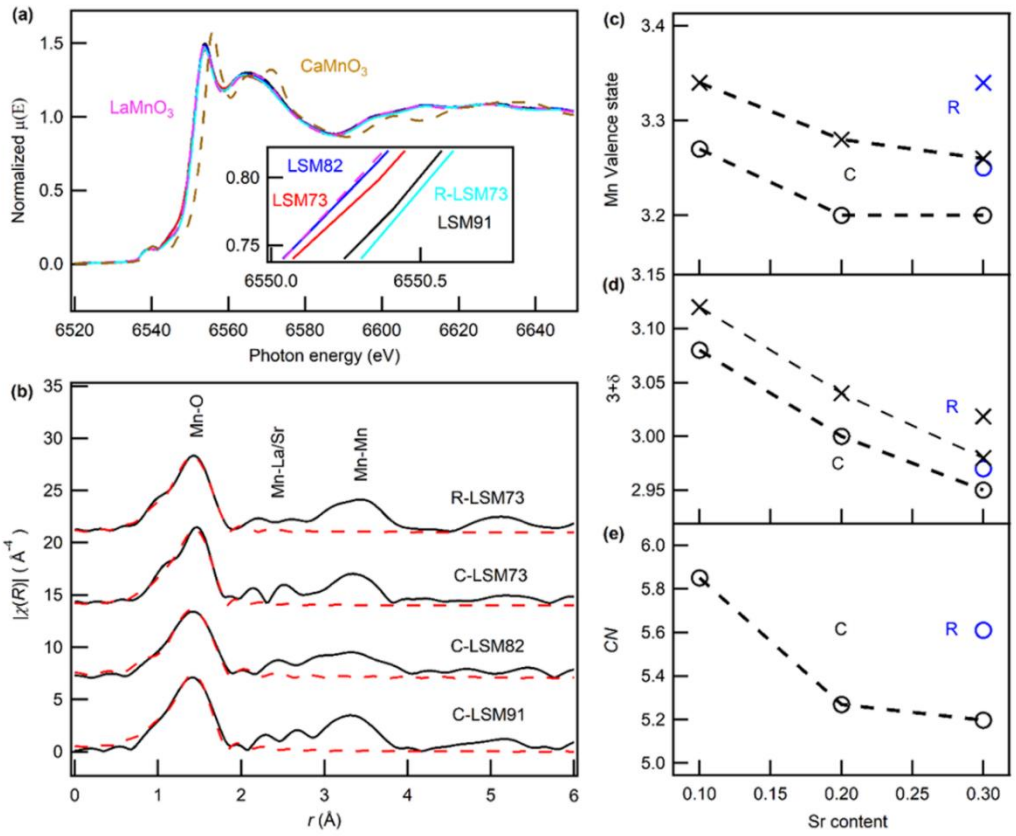


Figure 4-10 (a) Mn K-edge XAFS spectra of $La_{1-x}Sr_xMnO_{3-\delta}$ and reference samples at 415 ºC under dry air ($He/O_2$ = 4/1 (v/v)). Insets of (a) show enlarged absorption edge region. (b) Radial distribution functions obtained by Fourier transforming the EXAFS at 415 ºC under dry air ($He/O_2$ = 4/1 (v/v)). Black and red lines are the observed and the curve-fitting profiles to the 1st coordination shell (Mn-O), respectively. (c) Average Mn valence state determined from the chemical shift of XANES (○) and from iodometry (×). (d) Oxygen stoichiometry ($3+\delta$) calculated with the Mn valence due to XANES (○) and iodometry (×). (e) Oxygen-coordination number (*CN*) of Mn cations determined by EXAFS fitting analysis depicted in (b). In (c)−(e), the black and blue coloring distinguishes the cubic and rhombohedral phase, respectively.

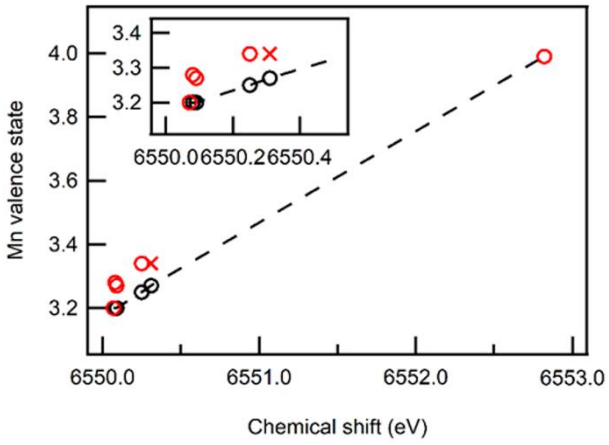


Figure 4-11 Mn valence states determined by XANES (black circles-dash line) and iodometry (red circles represent cubic LSM series and red cross is Rhombohedral LSM73). Inset is the enlarged part from 6550-6550.5 eV.

The radial distribution function (RDF) obtained from the Fourier-transformed EXAFS is presented in Figure 4-10b. For *C*-LSM, the first coordination shells corresponding to an intense peak at around 1.6−2.0 Å can be attributed to the shortest Mn−O bond, and the second and third coordination shells distributed between 2.0−4.0 Å can be assigned to the coherence in Mn−La or Mn−Sr and in Mn−Mn (Figure 4-10b). The curve fitting analysis to the first Mn−O coordination shell of *C*-LSM could converge very well by using atomic coordinates of cubic perovskite $LaMnO_3$ as an initial set,[33,35] yielding a Mn-O distance (*r*) of approximately 1.9 Å together with the oxygen-coordination numbers (*CN*) around Mn of 5.85±0.78, 5.27±0.82, and 5.20±0.60 for *C*-LSM91, *C*-LSM82, and *C*-LSM73, respectively (Figure 4-10e). The best fitting parameters including the *CN*, interatomic distance (*r*), and Debye−Waller parameters (*DW*) for the first Mn–O shell are summarized in Table 4-3. EXAFS normally tends to underestimate *CN* around transition metal atoms due to the effects of the *DW*, which is sensitive to the local symmetry of coordination sphere.[36] Nevertheless, all LSM yield significantly low *DW* of about 0.009, indicating that the contributions of the orbital symmetry are almost equivalent each other in LSM series. The *CN* of cubic-type $La_{1-}$

$_{x}Sr_{x}MnO_{3+\delta}$ decreases with $x$, which is in agreement with the trend of oxygen excesses ($+\delta$) determined from the iodometry (Figure 4-10d).

Table 4-3 Parameters obtained by simulation of EXAFS spectra for LSM.

| Samples | Conditions | Mn valence state | *CN* | r/Å | *DW* |
|---|---|---|---|---|---|
| *C*-LSM91 | dry | 3.27 | 5.85±0.78 | 1.91 | 0.0092±0.002 |
| | wet | 3.27 | 5.87±0.85 | 1.91 | 0.0094±0.002 |
| *C*-LSM82 | Dry | 3.20 | 5.27±0.82 | 1.92 | 0.0088±0.002 |
| | Wet | 3.20 | 5.25±0.82 | 1.93 | 0.0007±0.003 |
| *C*-LSM73 | dry | 3.20 | 5.20±0.60 | 1.92 | 0.0085±0.002 |
| | wet | 3.25 | 5.38±0.67 | 1.90 | 0.0084±0.001 |
| *R*-LSM73 | dry | 3.25 | 5.61±0.51 | 1.93 | 0.0095±0.001 |
| | wet | 3.25 | 5.62±0.89 | 1.93 | 0.0093±0.002 |

### 4-3-5 *In-situ* EXAFS

In order to elucidate the local structural rearrangements accompanying the hydration/dehydration reactions, *in-situ* Mn *K*-edge XANES was measured for *C*-LSM91, *C*-LSM82, *C*-LSM73, and *R*-LSM73 with switching of dry and wet air at 415 °C (Figures 4-12a-d). The absorption edge position of *C*-LSM73 shifts from 6550.09 to 6550.28 eV with switching from dry to wet (Figure 4-12c), indicating the average Mn valence state increases from 3.20 to 3.25 by hydration (Figure 4-12i, Table 4-3). The position recovers to 6550.09 eV after switching back to dry condition, and thus the chemical shifts occur reversibly in response to wet and dry gases (Figure 2-13). Fourier transform EXAFS clarifies that the peak of the first Mn–O coordination sphere becomes stronger by hydration, which results in the increase of *CN* from 5.20 to 5.38 for *C*-LSM73 (Figures 4-12g and j, Table 4-3). These results unambiguously demonstrate that the hydration and dehydration reactions of *C*-LSM73 involve oxidation and reduction of the Mn cations, respectively, together with decrease and increase of oxygen vacancies, respectively.

On the other hand, *C*-LSM91, *C*-LSM82 and *R*-LSM73 do not cause chemical shifts of adsorption edge (Figures 6a-c) and amplification of Mn-O coordination peaks (Figures 4-12e-h) in response to dry to wet switching, confirming that the changes of valence state and *CN* are negligibly small during dry/wet switching (Figure 4-12i and j, Table 4-3).

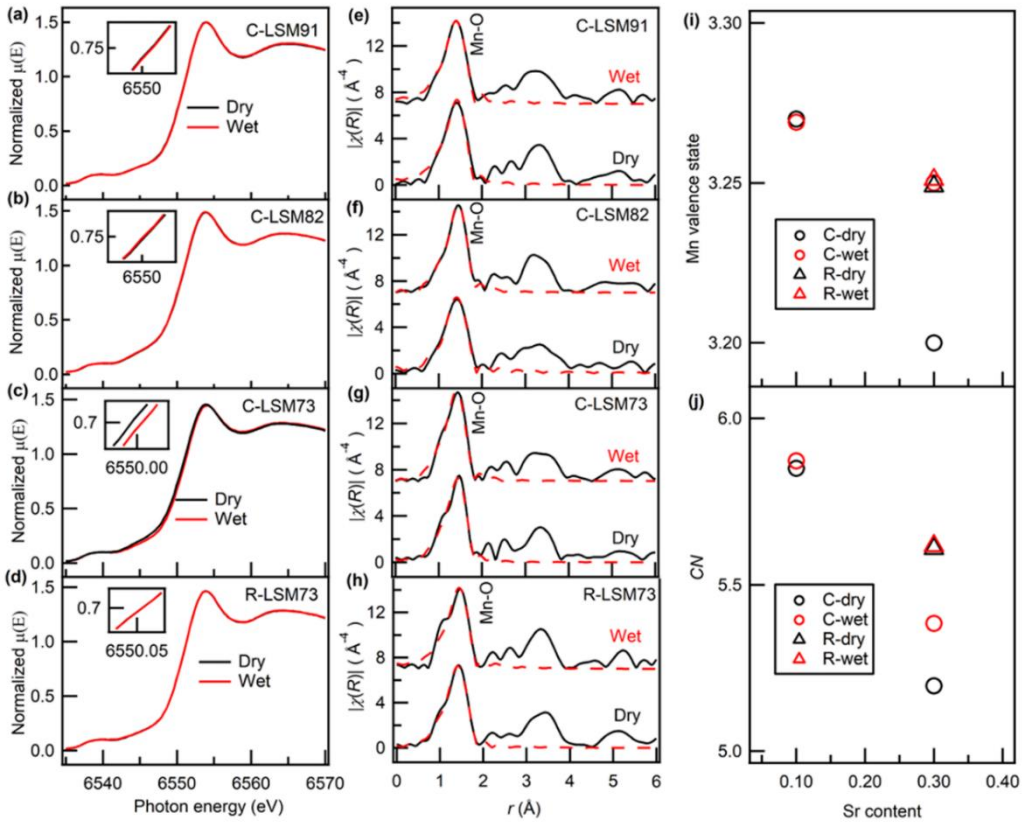


Figure 4-12 *In-situ* Mn K-edge XAFS of (a) *C*-LSM91, (b) *C*-LSM82, (c) *C*-LSM73, and (d) *R*-LSM73 in a cycle of dry and wet air supply at 415 ºC. Insets of (a)-(d) show the enlarged absorption edge region. Fourier-transformed EXAFS radial distribution functions of (e) *C*-LSM91, (f) *C*-LSM82, (g) *C*-LSM73, and (h) *R*-LSM73. In (e)-(h), black and red lines show the observed and the curve-fitting profiles to the 1st coordination shell (Mn-O), respectively. (i) Average Mn valence state determined from the chemical shift of absorption edges depicted in (a), (b), (c) and (d). (j) Oxygen-coordination numbers (*CN*) of Mn cations determined by EXAFS fitting analysis depicted in (e), (f), (g) and (h). In (i) and (j), the circles and triangular symbols represent the cubic and rhombohedral phases, and black and red distinguish the dry and wet atmosphere, respectively.

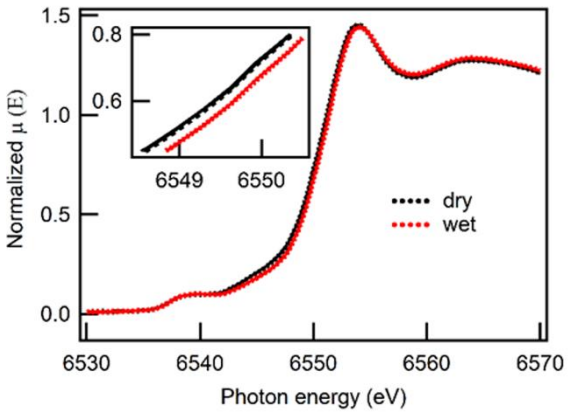


Figure 4-13 *In-situ* Mn K-edge XANES spectra of *C*-LSM73, measured during repeated 5 cycles of atmospheric switching between wet/dry every 30 mins at 415 ℃ in air conditions. Inset presents an enlarge of adsorption edge region, the absorption edge position repeatedly shifts from 6550.09 to 6550.28 eV.

## 4-4 Discussion

### 4-4-1 Reaction mechanism

Combined results of TG, iodometry and EXAFS proves that *C*-LSM73 involves thermochemical dehydration/hydration reactions via association between oxygen vacancies and water molecules due to the presence of significant amount of oxygen vacancies. *R*-LSM73 is expected to have small amount of the vacancies, thereby becoming weakly hydrated under wet atmosphere. *C*-LSM91 and *C*-LSM82 have apparent oxygen excesses and thus, do not undergo the hydration reactions.

In proton-conducting ceramic electrolytes such as $BaZr_{1-x-y}Ce_xY_yO_3$, the proton carriers are incorporated via the association between oxygen vacancies and water molecules, as represented in Equation (4-1).[16,37,38]

$$O_O^X + V_O^{\bullet\bullet} + H_2O_{(g)} \leftrightarrow 2OH_O^{\bullet} \qquad (4\text{-}1)$$

Equation (4-1) uses the Kröger-Vink notation, with $OH_O^{\bullet}$ being the proton defect, $O_O^X$ the lattice oxygen, and $V_O^{\bullet\bullet}$ the oxygen vacancy. In metal oxides, association between oxygen vacancies and oxygen gas is equilibrated.

$$V_O^{\bullet\bullet} + 1/2\ O_2 \rightarrow O_O^X + 2\ h^{\bullet} \qquad (4\text{-}2)$$

Here, $h^{\bullet}$ is an electron hole. If the hole carriers are incorporated in the valence band comprising mainly of O *2p* states, Equation (4-2) is rewritten with an oxygen hole ($O_O^{\cdot}$).[36, 39]

$$V_O^{\bullet\bullet} + 1/2\ O_2 + O_O^X \rightarrow 2\ O_O^{\cdot} \qquad (4\text{-}3)$$

The proton and hole carriers are in equilibrium by the following reactions.

$$H_2O + 2\ O_O^{\cdot} \rightarrow 2\ OH_O^{\cdot} + 1/2\ O_2 \qquad (4\text{-}4)$$

Coupling Equation (4-3) and (4-4) gives Equation (4-1).

In the case of LSM, the association between $V_O^{\bullet\bullet}$ and $O_2$ gas involves valence change of Mn cations,[40] so that reaction (4-2) is modified as follows

$$V_O^{\bullet\bullet} + 1/2\ O_2 + O_O^{\times} + 2\ Mn(III)_{Mn}^{\times} \rightarrow 2\ O_O^{\times} + 2\ Mn(IV)_{Mn}^{\cdot} \qquad (4\text{-}5)$$

Combining Equation (4-3) and (4-5) yields the hydration reaction mediated by Mn oxidation.

$$Mn(III)_{Mn}^{\times} + V_O^{\cdot\cdot} + O_O^{\cdot} + H2O \leftrightarrow Mn(IV)_{Mn}^{\cdot} + 2OH_O^{\cdot} \qquad (4\text{-}6)$$

Equation (4-6) suggests that oxygen holes are indispensable for proton uptake in LSM. In fact, manganese perovskite comprising Mn(IV) such as $La_{1-x}Sr_xMnO_3$, $La_{1-x}Ca_xMnO_3$, and $Bi_{1-x}Ca_xMnO_3$ have been reported to generate hole carriers in O *2p* states through strong Mn *3d*-O *2p* hybridization.[41-45] Such oxygen holes have a crucial role in the colossal magneto resistivity, magnetron-electron coupling, metallic ferromagnetism, and so on. To verify the formation of oxygen holes, O K-edge XAFS spectra were measured for hydrated and dehydrated LSM series (Figure 4-14). Peak α located at about 529 eV corresponds to the electron transition from O 1*s* to O 2*p* state hybridized with Mn 3*d* (Mn3*d*-O2*p*), and peaks β and γ are attributed to the transition to the hybridized states consisting of La/Sr 3*d* and O 2*p* as well as Mn 4*s* and O 2*p*, respectively. In *C*-LSM73, peak α of the dehydrated sample is more intense than that of the hydrated one, indicating that the number of unoccupied O 2*p* states hybridized with Mn *3d* decreases by bulk hydration. This provides direct evidence for the decline of oxygen holes in *C*-LSM73 through hydration. On the other hand, the spectra of *C*-LSM91 and *R*-LSM73 remains unchanged with hydration treatments, which is rather consistent with the less-pronounced hydration behavior of them (Table 4-2).

Based on Equation (4-6), there must be one-to-one relationship between the changes of Mn valence state and oxygen stoichiometry. The changes of oxygen stoichiometry in

*C*-LSMN73 should be corresponding to hydration capability $\Delta n$ (0.07; Table 4-2), which is almost same as Mn valence change (0.05; Table 4-2) by hydration. In addition, half of the changes of *CN* also give the changes of oxygen stoichiometry, and the value (0.09; Table 4-2) is consistent with the valence change. These unequivocally demonstrate that the hydration/dehydration reactions of *C*-LSM73 are driven by coupled redox reactions of manganese cation and oxide anion according to equation (4-6).

A schematic reaction model for the hydration/dehydration reactions is proposed as shown in Figure 4-15. Here, oxygen hole carriers are assumed to localize on oxygen atoms. Under this assumption, the creation of oxygen hole carriers in LSM can be interpreted as intermixing of the ligand-to-metal charge transfer (LMCT) states such as $d^4\underline{L}^1$ with the ionic states ($d^3\underline{L}^0$).[41,46] Thus, the LSM matrix can be described by coexisting $Mn^{3+}$-$O^-$ and $Mn^{4+}$-$O^{2-}$ configurations, which correspond to the LMCT states and ionic states, respectively. Here, $d^n$ is the Mn *3d* orbital occupied by *n* electrons, and $\underline{L}^n$ are oxygen 2*p* orbitals with *n* holes. From the EXAFS results (Figure 4-12), the incorporation of oxide ions into oxygen vacancies for hydration causes oxidation of the adjacent Mn cations from $Mn^{3+}$ to $Mn^{4+}$, with a simultaneous increase in the local coordination number around the Mn cations. The oxygen holes must be replaced by water protons to cancel the excess positive charge due to Mn oxidation, and thus the $Mn^{3+}$-$O^-$ configuration is converted to $Mn^{4+}$-$O^{2-}$.

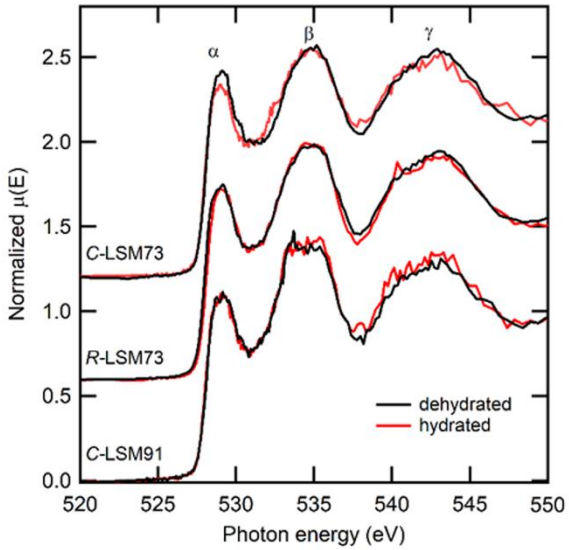


Figure 4-14 O K-edge XAS spectra of hydrated and dehydrated phases for *C*-LSM91, *C*-LSM73, and *R*-LSM73. The hydrated and dehydrated phases were pretreated respectively in wet and dry air at 430 ℃, respectively, for 6 h. Black and red distinguish the dehydrated and hydrated phases, respectively. α, β, and γ peaks are represented in the main text.

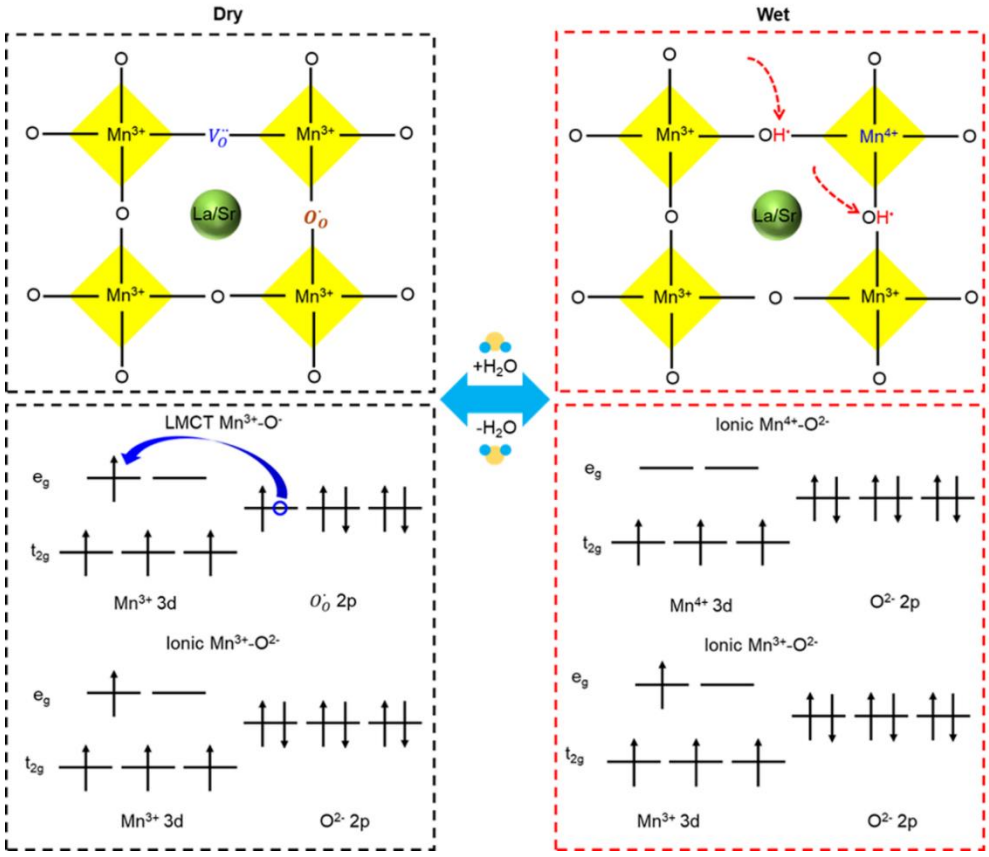


Figure 4-15 Mechanism for the hydration/dehydration reactions of *C*-LSM73, driven by the interconversion between the LMCT states ($d^4\underline{L}^1$ configuration) and ionic states ($d^3\underline{L}^0$ configuration).

### 4-4-2 Comparison of proton concentrations to other triple conductors

Finally, the amounts of water sorption of *C*-LSM73 are compared with other triple conductors, and the results are summarized in Table 4-2. In more recent years, Zohourian *et al.* investigated the proton uptake behavior of 18 compositions among the perovskite-type $Ba_{1-x}Sr_xFeO_{3-\delta}$ derivatives. They proposed that the basicity of the oxide ion is crucial for proton uptake by the metal oxides.[47] A- or B-site substitutions by cations with larger electronegativity result in a decrease in electron density, *i.e.* the basicity of oxide ions, and therefore proton attachment is less favorable.[47] $Ba_{0.95}La_{0.05}Fe_{0.8}Zn_{0.2}O_{3-\delta}$ which was designed with this concept has the highest reported proton concentration (~0.1) among the perovskite-related oxides (Table 1).[47] Notably, the concentration of *C*-LSM73 (~0.14; Table 1) are corresponding to the value of $Ba_{0.95}La_{0.05}Fe_{0.8}Zn_{0.2}O_{3-\delta}$, despite the higher calibration temperature of *C*-LSM73 than $Ba_{0.95}La_{0.05}Fe_{0.8}Zn_{0.2}O_{3-\delta}$ (415 *vs.* 200 ℃). Moreover, the proton concentration in *C*-LSM73 is comparable to those of well-known proton conductors such as $BaCe_{0.9}Y_{0.1}O_3$ (~0.1) and $BaZr_{0.9}Y_{0.1}O_3$ (~0.08) at 600 ℃ in wet $N_2$ atmosphere ($p_{H2O}$ = 0.023 atm).[16,19,21,48,49] In conclusion, *C*-LSM can uptake a larger amount of proton defects than other reported triple conductors in the IT region.

## 4-5 Conclusions

In summary, we demonstrated that cubic-perovskite type $La_{0.7}Sr_{0.3}MnO_{2.95}$ undergoes reversable hydration/dehydration reactions at intermediate temperatures. This oxide can retain water with a mole fraction of more than 0.07 at 415 ℃ in air, which is much higher than the hydration amounts of other perovskite-based triple conductors. Cubic-type $La_{0.7}Sr_{0.3}MnO_{2.95}$ undergoes decline of antibonding O *2p* states hybridized with Mn *3d* orbitals together with oxidation of $Mn^{3+}$ to $Mn^{4+}$ through the hydration and thus retains bulk protons in the concentrations of 0.14 in wet air at around 415 ℃. These discoveries offer a general guideline to design triple conductors operating in air conditions, namely, that transition metal oxides possessing large amounts of oxygen vacancies and oxygen hole carriers could be promising mixed conducting materials. This guideline will help the development of new electrode materials for next-generation $H^+$-conducting oxide fuel cells and electrolyzers.

## 4-6 References


1. J. Dailly, S. Fourcade, A. Largeteau, F. Mauvy, J. C. Grenier and M. Marrony, *Electrochimica Acta*, 2010, **55**, 5847-5853.
2. Y. Lin, R. Ran and Z. Shao, *International Journal of Hydrogen Energy*, 2010, **35**, 8281-8288.
3. K. Kravchyk, E. Quarez, C. Solís, J. Serra and O. Joubert, *international journal of hydrogen energy*, 2011, **36**, 13059-13066.
4. C. Duan, J. Tong, M. Shang, S. Nikodemski, M. Sanders, S. Ricote, A. Almansoori and R. O'Hayre, *Science*, 2015, **349**, 1321-1326.
5. D. K. Lim, H. N. Im, B. Singh and S.-J. Song, *Journal of The Electrochemical Society*, 2015, **162**, F547-F554.
6. S. Choi, C. J. Kucharczyk, Y. Liang, X. Zhang, I. Takeuchi, H. I. Ji and S. M. Haile, *Nature Energy*, 2018, **3**, 202-210.
7. R. Strandbakke, O. Dyrlie, F. S. Hage and T. Norby, *Journal of The Electrochemical Society*, 2016, **163**, F507-F515.
8. Y. Aoki, E. Tsuji, T. Motohashi, D. Kowalski and H. Habazaki, *The Journal of Physical Chemistry C*, 2018, **122**, 22301-22308.
9. G. Wang, T. Xu, S. Wen and M. Pan, *Science China Chemistry*, 2015, **58**, 871-878.
10. X. Luo, Y. Yang, Y. Yang, D. Tian, X. Lu, Y. Chen, Q. Huang and B. Lin, *Electrochimica Acta*, 2018, **260**, 121-128.
11. Z. J. Razi, S. Sebt and A. Khajehnezhad, *Journal of Theoretical and Applied Physics*, 2018, **12**, 243-248.
12. N. Miniajluk, J. Trawczyński, M. Zawadzki and W. Tylus, *Advances in Materials Physics and Chemistry*, 2018, **8**, 193.
13. L. Rørmark, K. Wiik, S. Stølen and T. Grande, *Journal of Materials Chemistry*, 2002, **12**, 1058-1067.
14. I. K. Andersen, E. K. Andersen, P. Norby and E. Skou, *Journal of Solid State Chemistry*, 1994, **113**, 320-326.
15. S. Cimino, L. Lisi, R. Pirone, G. Russo and M. Turco, *Catalysis today*, 2000, **59**, 19-31.
16. K. Kreuer, *Solid State Ionics*, 1999, **125**, 285-302.
17. M. Karlsson, M. E. Björketun, P. G. Sundell, A. Matic, G. Wahnström, D. Engberg, L. Börjesson, I. Ahmed, S. Eriksson and P. Berastegui, *Physical Review B*, 2005, **72**, 094303.
18. R. Zohourian, R. Merkle, G. Raimondi and J. Maier, *Advanced Functional Materials*, 2018, **28**, 1801241.
19. D. Poetzsch, R. Merkle and J. Maier, *Faraday discussions*, 2015, **182**, 129-143.
20. D. Poetzsch, R. Merkle and J. Maier, *Physical Chemistry Chemical Physics*, 2014, **16**, 16446-16453.
21. J. Mizusaki, N. Mori, H. Takai, Y. Yonemura, H. Minamiue, H. Tagawa, M. Dokiya,

H. Inaba, K. Naraya and T. Sasamoto, *Solid state ionics*, 2000, **129**, 163-177.
22. A. Y. Zuev and D. Tsvetkov, *Solid State Ionics*, 2010, **181**, 557-563.
23. A. N. Grundy, B. Hallstedt and L. J. Gauckler, *Calphad*, 2004, **28**, 191-201.
24. R. A. De Souza, M. S. Islam and E. Ivers-Tiffée, *Journal of Materials Chemistry*, 1999, **9**, 1621-1627.
25. J. Rana, M. Stan, R. Kloepsch, J. Li, G. Schumacher, E. Welter, I. Zizak, J. Banhart and M. Winter, *Advanced Energy Materials*, 2014, **4**, 1300998.
26. F. Farges, *Physical review B*, 2005, **71**, 155109.
27. C. Henderson, J. Charnock, J. Smith and G. Greaves, *American Mineralogist*, 1993, **78**, 477-485.
28. D. Joseph, A. K. Yadav, S. Jha and D. Bhattacharyya, *Bulletin of Materials Science*, 2013, **36**, 1067-1072.
29. A. Gaur, B. D. Shrivastava and H. Nigam, *Proceedings of the Indian National Science Academy*, 2013, **79**, 921-966.
30. B. Wei, Z. Lü, X. Huang, M. Liu, N. Li and W. Su, *Journal of Power Sources*, 2008, **176**, 1-8.
31. J. Wong, F. Lytle, R. Messmer and D. Maylotte, *Physical Review B*, 1984, **30**, 5596.
32. Y. Li, X. Wang, Y. Gao, Q. Zhang, G. Tan, Q. Kong, S. Bak, G. Lu, X. Q. Yang and L. Gu, *Advanced Energy Materials*, 2019, **9**, 1803087.
33. V. Celorrio, L. Calvillo, C. A. van den Bosch, G. Granozzi, A. Aguadero, A. E. Russell and D. J. Fermín, *ChemElectroChem*, 2018, **5**, 3044-3051.
34. D. M. Melo, F. M. Borges, R. C. Ambrosio, P. M. Pimentel, C. N. da Silva Júnior and M. A. Melo, *Chemical Physics*, 2006, **322**, 477-484.
35. V. Cuartero, J. Blasco, G. Subías, J. García, C. Meneghini and G. Aquilanti, *Physical Review B*, 2015, **92**, 125118.
36. S. J. Song, E. D. Wachsman, S. E. Dorris and U. Balachandran, *Solid State Ionics*, 2002, **149**, 1-10.
37. T. Norby and Y. Larring, *Current Opinion in Solid State and Materials Science*, 1997, **2**, 593-599.
38. D. K. Lim, M.-B. Choi, K. T. Lee, H. S. Yoon, E. Wachsman and S. J. Song, *International Journal of Hydrogen Energy*, 2011, **36**, 9367-9373.
39. C. J. Park, H. W. Ryu, J. H. Moon, J. S. Lee and S. J. Song, *Ceramics International*, 2009, **35**, 1769-1773.
40. C. R. Fell, D. Qian, K. J. Carroll, M. Chi, J. L. Jones and Y. S. Meng, *Chemistry of Materials*, 2013, **25**, 1621-1629.
41. D. Sarma, O. Rader, T. Kachel, A. Chainani, M. Mathew, K. Holldack, W. Gudat and W. Eberhardt, *Physical Review B*, 1994, **49**, 14238.
42. M. C. Martin, G. Shirane, Y. Endoh, K. Hirota, Y. Moritomo and Y. Tokura, *Physical Review B*, 1996, **53**, 14285.
43. Y. Murakami, D. Shindo, H. Chiba, M. Kikuchi and Y. Syono, *Physical Review B*, 1999, **59**, 6395.

44. K. M. Krishnan and H. Ju, *Physical Review B*, 1999, **60**, 14793.
45. S. Grenier, K. Thomas, J. Hill, U. Staub, Y. Bodenthin, M. García-Fernández, V. Scagnoli, V. Kiryukhin, S. W. Cheong and B. Kim, *Physical review letters*, 2007, **99**, 206403.
46. T. Saitoh, A. Bocquet, T. Mizokawa, H. Namatame, A. Fujimori, M. Abbate, Y. Takeda and M. Takano, *Physical Review B*, 1995, **51**, 13942.
47. R. Zohourian, R. Merkle, G. Raimondi and J. Maier, *Advanced Functional Materials*, 2018, **28**, 1801241.
48. K. D. Kreuer, *Annual Review of Materials Research*, 2003, **33**, 333-359.
49. K. Kreuer, T. Dippel, Y. M. Baikov and J. Maier, *Solid State Ionics*, 1996, **86**, 613-620.

# Chapter 5 Mixed Proton–electron–oxide Ion Triple Conducting Manganite as Efficient Cobalt-free Cathode for Protonic Ceramic Fuel Cells

## 5-1 Introduction

Manganese base perovskites, i.e. $La_{1-x}Sr_xMnO_3$ have been recognized to poorly-active cathode materials for PCFCs in comparison to cobalt base oxides.[1-7] However, it is still highly demanded to develop Co-free alternatives for PCFCs because of the relatively high reactivity, resource scarcity, and cost of Co oxides.[8] As already demonstrated in Chapter 4, cubic-perovskite type $La_{0.7}Sr_{0.3}MnO_{2.95}$ (C-LSM73) undergoes reversible thermochemical hydration/dehydration reactions at intermediate temperatures, which is driven by the charge disproportionation between O and Mn, and retain 0.07 mole fraction $H_2O$ at 415 ºC in wet air, which can be comparable with the well-known electrolyte $Ba(Zr,Ce,Y)O_3$.[9] Similarly, its derivatives $La_{0.7}Sr_{0.3}Mn_{1-x}Ni_xO_{3-\delta}$ (LSMN; $x$ = 0.1 and 0.3) must have such hydration/dehydration behavior. Therefore, C-LSM73 and its derivatives LSMN are potential Co-free, $H^+/e^-/O^{2-}$ triple conducting cathodic materials for advanced PCFCs owing to its sufficient proton conductivity at intermediate temperatures.

Herein, we demonstrate the hydration/dehydration reactions of LSMN, and the applications of C-LSM73 and its derivatives $La_{0.7}Sr_{0.3}Mn_{1-x}Ni_xO_{3-\delta}$ (LSMN; $x$ = 0.1 and 0.3) as the cathode of PCFCs. C-LSM73 and its derivatives LSMN can help significantly lower the cathodic polarization resistance of Zr-rich side $BaZr_{0.4}Ce_{0.4}Y_{0.2}O_3$ (BZCY442)-based PCFCs. The aliovalent substitution of $Mn^{4+}$ with $Ni^{3+}$ sufficiently improves the hydration capacity of $La_{0.7}Sr_{0.3}MnO_{3-\delta}$ owing to increased oxygen vacancies for water association. Thus, the $La_{0.7}Sr_{0.3}Mn_{1-x}Ni_xO_{3-\delta}$ cathode, including the widely-used $La_{0.6}Sr_{0.4}Co_{0.2}Fe_{0.8}O_3$ (LSCF6428), exhibits low

cathodic polarization resistance at intermediate temperatures. This confirms their applicability as a cobalt-free PCFC cathodic material.

## 5-2 Experimental section

### 5-2-1 Synthesis of LSMN

$La_{0.7}Sr_{0.3}Mn_{1-x}Ni_xO_{3-\delta}$ (LSMN; $x$ = 0.1, 0.3) fine powders were synthesized via a citrate precursor route described in Chapter 3-2-1.

### 5-2-2 Fabrication of PCFCs

The fuel electrode-supported PCFCs were fabricated by solid-state reactive sintering with a sintering aid of $Zn(NO_3)_2$. The cells in this Chapter is the lack of $La_{0.5}Sr_{0.5}CoO_3$ (LSC55) film deposited in BZCY442, the other procedures are same with cells prepared in Chapter 3 as detailly described in Chapter 3-2-2.

### 5-2-3 Characterizations

#### (a) Structural characterizations

XRD and SEM were carried out for the phase impurity and microstructure of LSMN oxides and fuel cells, the measurement conditions were detailed described in Chapter 3-2-3. *In-situ* transmittance IR spectra was conducted by FT-IR-4600 Fourier Transform Infrared Spectrometer from JASCO. The details were shown in Chapter 4-2-2.

#### (b) Rietveld structure refinement

The XRD patterns were refined by the Rietveld method using the Material Studio software over the 2θ range of 20−80°.

#### (c) Thermodynamic characterizations for hydration

The TG measurements for possibility of hydration and hydration ability cyclic were performed by the same techniques and conditions mentioned in Chapter 3-2-3 and

Chapter 4-2-2.

**(d) Single crystal X-ray absorption spectroscopy**

The *in-situ* extended X-ray absorption fine structure (EXAFS) for the Mn K-edge and Ni K-edge was obtained on the BL01B1 station of *Spring-8* facility, Japan Synchrotron Radiation Research Institute (JASRI). The measuring details were described in Chapter 4-2-2.

**(e) Fuel cell test**

The current–voltage (*I–V*), current–power (*I–P*) and impedance spectra of fuel cell were carried out in a Solartron 1260A frequency response analyzer implemented with a Solartron 1287 potentiostat, the measured details were described in Chapter 3-2-3.

## 5-3 Results and discussion

### 5-3-1 Preparation of LSMN

Figure 5-1 shows the XRD patterns of $La_{0.7}Sr_{0.3}Mn_{1-x}Ni_xO_{3-\delta}$ (LSMN; $x$ = 0.1 and 0.3), which are denoted hereinafter by LSMN7391 and LSMN7373, respectively. First, single cubic-perovskite phases of LSMN7391 and LSMN7373 were obtained by annealing (800 ℃ for 15 h in pure $O_2$) based on our previous report;[9] these are called *C*-LSMN7391 and *C*-LSMN7373, respectively. Both *C*-LSMN7391 and *C*-LSMN7373 completely transform to a rhombohedral phase (*R*) after annealing at 1000 ℃ under pure $O_2$ for 15 h, as confirmed by a Rietveld analysis conducted previously.[9] The rhombohedral LSMN oxides are abbreviated as *R*-LSMN7391 and *R*-LSMN7373.

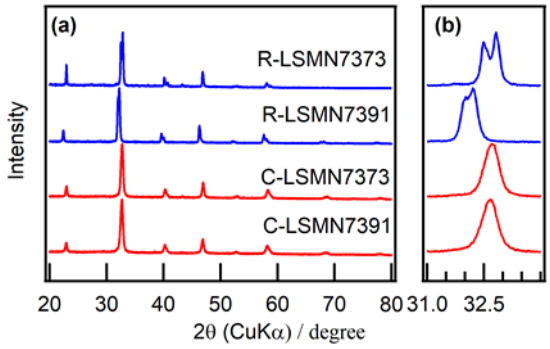


Figure 5-1 (a) XRD patterns of cubic- and rhombohedral-type $La_{0.7}Sr_{0.3}Mn_{1-x}Ni_xO_{3-\delta}$ ($x$ = 0.1, and 0.3). (b) Expansion of (110) peaks for cubic phase, and (110) and (104) peaks for rhombohedral phase.

### 5-3-2 Hydration/dehydration reactions of LSMN

Figures 5-2a–d show the thermogravimetric (TG) curves of the *C*-LSMN samples, measured at temperatures ranging from room temperature (RT, 30 ℃) to 1000 ℃ under dry and wet Ar (including 10 ppm of $O_2$ additive) and air. (In the discussion hereinafter, the Ar gas includes 10 ppm of $O_2$.). Both *C*-LSMN7391 and *C*-LSMN7373 exhibit three steps of thermal weight losses both in Ar and in air. The weight losses at $T < 200$ ℃ and at approximately 700 ℃ can be attributed to the desorption of surface $H_2O$ and the lattice oxygen loss with the reduction from $Mn^{4+}$ to $Mn^{3+}$,[10] respectively. *C*-LSMN exhibits a clear mass loss at approximately 400 ℃, probably because of the dehydration following the release of bulk $H_2O$.[9] The onset temperature corresponding to the clear mass loss is 350 ℃ in dry atmosphere and it increases to 402, 411, and 430 ℃ when increasing the water partial pressure ($p_{H2O}$) to 0.003, 0.009, and 0.023, respectively, for *C*-LSMN7373 (Figure 5-3a). The onset temperatures are not sensitive to the oxygen partial pressure ($p_{O2}$): the clear mass loss starts at 350 °C in dry air and at 430 °C in wet air ($p_{H2O} = 0.023\ p_0$), which are the same as those in dry and wet Ar ($p_{H2O} = 0.023\ p_0$), respectively (Figures 5-2c and d). These characteristics prove that the mass losses at approximately 400 ℃ are related to thermochemical dehydration reactions. In contrast, the corresponding rhombohedral phases, namely *R*-LSMN7391 and *R*-LSMN7373, do not show apparent weight losses in the temperature range of 200–700 ℃ in dry and wet atmospheres (Figures 5-2e–h), indicating that the rhombohedral phase does not undergo enhanced hydration when $p_{H2O} = 0.023\ p_0$.

To verify the capability of reversible proton uptake and release through thermochemical hydration/dehydration reactions, the mass changes are monitored at 415 ℃ by repeatedly switching between dry and wet ($p_{H2O} = 0.023\ p_0$) atmospheres every 30 mins, as shown in Figures 5-3c–f. *C*-LSMN exhibits reversible mass changes when dry/wet switching in both Ar and air atmospheres (Figures 5-3c–f), with a mass gain on exposure to wet gases ($p_{H2O} = 0.023\ p_0$) and an equal mass loss when exposed

to dry gases. Here, the weight variable (*ΔW)* is defined as the mean weight difference between the samples equilibrated in dry and wet conditions for five switching cycles. *C*-LSMN7391 exhibits *ΔW* of approximately 0.40 and 0.44 wt% in wet Ar and air, respectively (Table 1; Figures 5-3c and e), and *C*-LSMN7373 exhibits *ΔW* of 0.64 wt% in Ar and 0.78 wt% in air (Table 1; Figures 5-3d and f); the latter values are higher than those of *C*-LSM73 (0.5 wt%).[35] The hydration/dehydration cycles are completely repeatable, because the mass loss during dehydration and mass gain during hydration agree within 10%. As for *R*-LSMN, the TG curves at 415 ℃ are almost flat as the Ar/air is changed between dry and wet conditions (Figure 5-4), which is in accordance with the unapparent weight losses in the temperature range of 200–700 ℃ in both dry and wet atmospheres (Figures 5-2e–h).

The *ΔW* value of *C*-LSMN7373 is very sensitive to $p_{H2O}$; the values decrease from 0.78 wt% to 0.33 wt% to 0.07 wt% when $p_{H2O}$ is decreased from 0.023 to 0.009 to 0.003 in wet air (Figure 5-3b). This shows that *C*-LSMN can undergo thermochemical hydration reactions even at elevated temperatures.

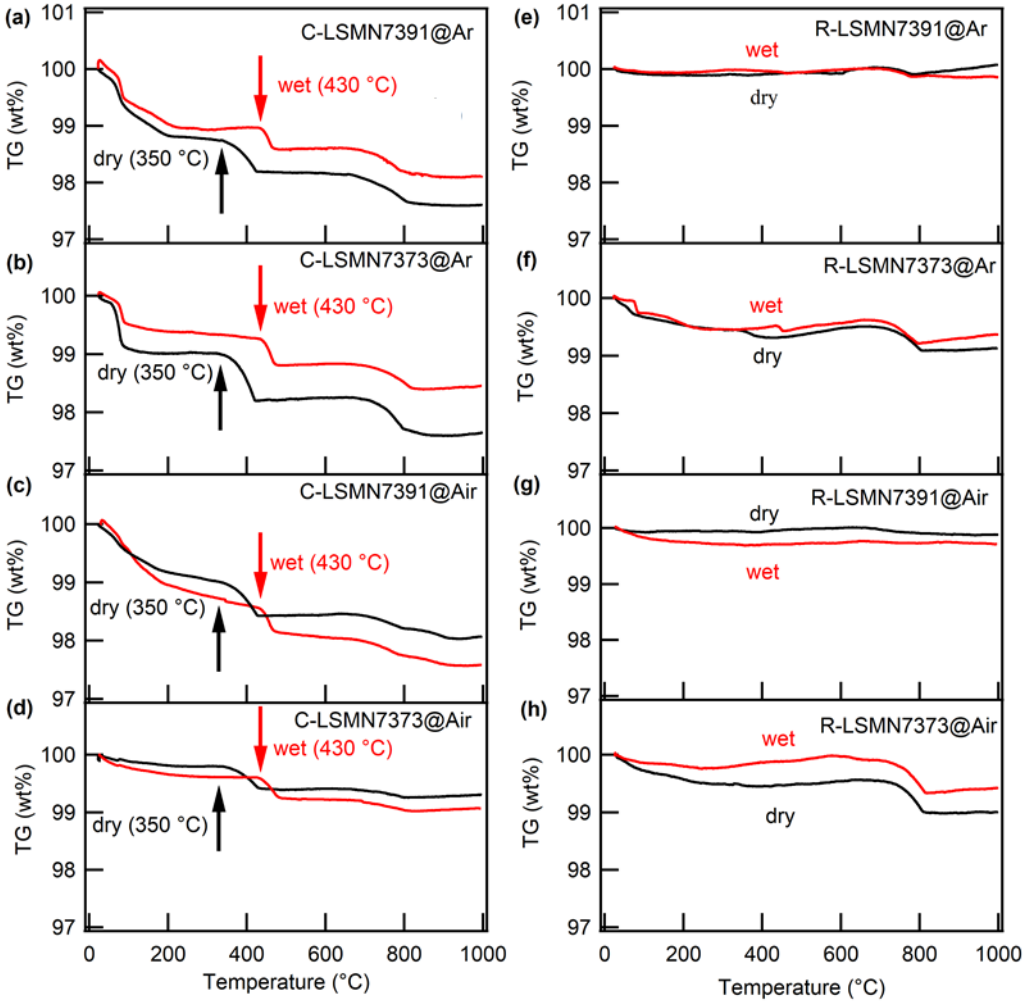


Figure 5-2 TG curves measured at temperatures ranging from RT to 1000 ℃ in dry and wet Ar (10 ppm $O_2$ additive) (a, b, e, f) and air (c, d, g, h) for *C*-LSMN7391, *C*-LSMN7373, and *R*-LSMN7391, *R*-LSMN7373. In (a)–(d), the black and red arrows indicate the onset temperatures for dehydration in dry and wet atmospheres, respectively.

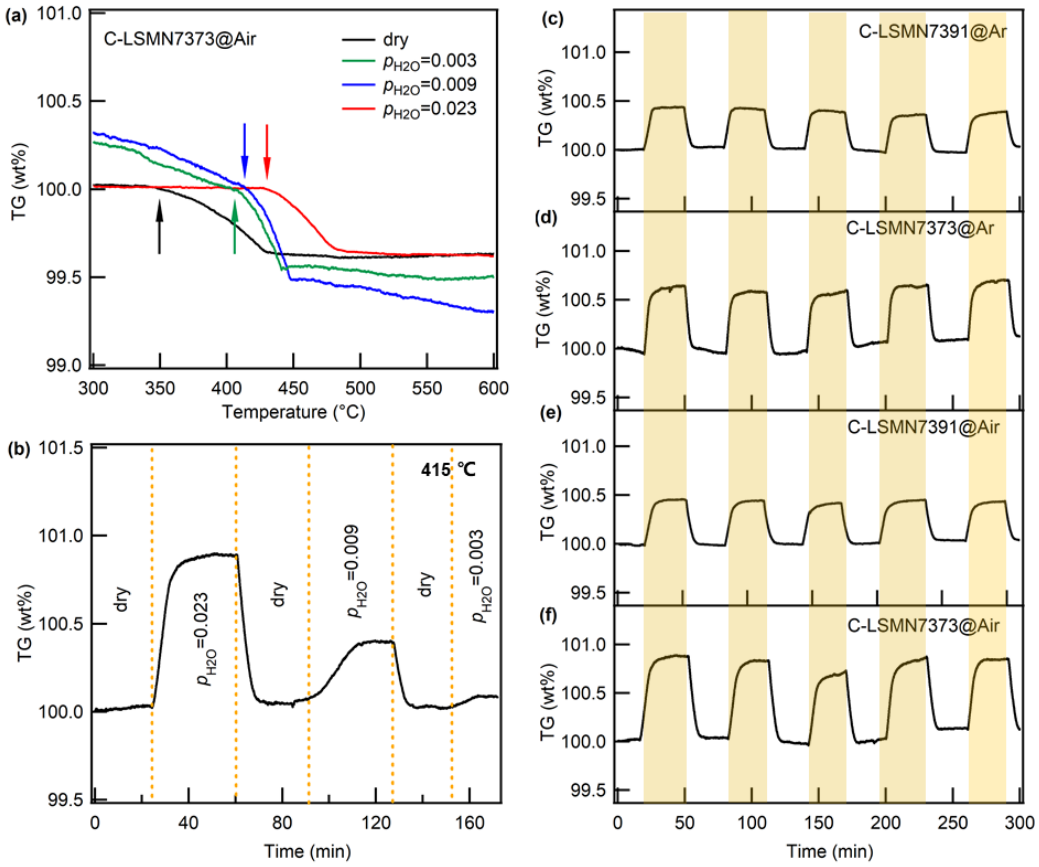


Figure 5-3 (a) TG curves of *C*-LSMN7373 under wet air atmosphere with different $p_{H2O}$. Here, '100 wt%' of the TG curves was set at the weight of onset temperatures of releasing bulk water for the comparison. In (a), the arrows indicate the onset temperature to start dehydration. (b) Weight gain/loss in response to atmospheric switching between wet/dry air every 30 mins at 415 ℃ for *C*-LSMN7373 with different $p_{H2O}$. Weight gain/loss of *C*-LSMN7391 and *C*-LSMN7373 in response to atmospheric switching between wet/dry Ar (c, d) and air (e, f) every 30 mins at 415 ℃. The pale-yellow areas represent the duration for which the samples were under wet atmosphere.

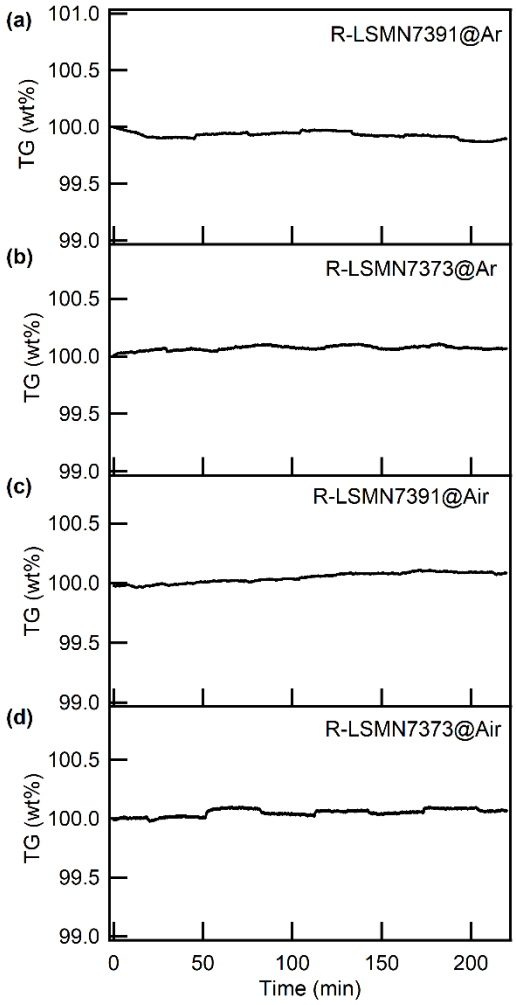


Figure 5-4 Weight gain/loss in response to atmospheres by repeatedly switching wet and dry Ar (a, b) / air (c, d) every 30 mins for *R*-LSMN7391 and *R*-LSMN7373 at 415 ℃, $p_{H2O}$=0.023 $p_0$.

Table 5-1 Hydration properties of *C*-LSMN and other triple conductors.

| Systems | ΔW (wt%) | Δn[a] | Proton concentration (mol%) | Temperature (°C) | $p_{H2O}$ (atm) | Ref. |
|---|---|---|---|---|---|---|
| *C*-$La_{0.7}Sr_{0.3}Mn_{0.9}Ni_{0.1}O_{2.93}$ | 0.44 (air)<br>0.40 (Ar) | 0.055 (air)<br>0.051 (Ar) | 0.110 (air)<br>0.102 (Ar) | 415 | 0.023 | This work |
| *C*-$La_{0.7}Sr_{0.3}Mn_{0.7}Ni_{0.3}O_{2.94}$ | 0.78 (air)<br>0.64 (Ar) | 0.098 (air)<br>0.080 (Ar) | 0.196 (air)<br>0.160 (Ar) | 415 | 0.023 | This work |
| *C*-$La_{0.7}Sr_{0.3}Mn_{0.7}Ni_{0.3}O_{2.94}$ | 0.33 (air) | 0.042 (air) | 0.084 (air) | 415 | 0.009 | This work |
| *C*-$La_{0.7}Sr_{0.3}Mn_{0.7}Ni_{0.3}O_{2.94}$ | 0.07 (air) | 0.008 (air) | 0.016 (air) | 415 | 0.003 | This work |
| *C*-$La_{0.7}Sr_{0.3}MnO_{2.95}$ | 0.56 (air)<br>0.51 (Ar) | 0.071 (air)<br>0.064 (Ar) | 0.142 (air)<br>0.128 (Ar) | 415 | 0.023 | 9 |
| $PrBa_{0.5}Sr_{0.5}Co_{1.5}Fe_{0.5}O_{5+\delta}$ | - | 0.018 | 0.036 | 200 | 0.02 | 11 |
| $Ba_{0.95}La_{0.05}Fe_{0.8}Zn_{0.2}O_{3-\delta}$ | - | 0.050 | 0.10 | 200 | 0.016 | 12 |
| $BaCo_{0.4}Fe_{0.4}Zr_{0.2}O_{3-\delta}$ | - | - | 0.015-0.05 | 200-400 | 0.015 | 13 |
| $Ba_{0.5}Sr_{0.5}Fe_{0.8}Zn_{0.2}O_{3-\delta}$ | - | - | 0.015 | 350 | 0.02 | 14 |
| $Ba_{0.5}Sr_{0.5}Fe_{0.8}Zn_{0.2}O_{3-\delta}$ | - | - | 0.02 | 400 | 0.02 | 14 |
| $Ba_{0.5}Sr_{0.5}Fe_{0.8}Zn_{0.2}O_{3-\delta}$ | - | - | 0.013-0.032 | 350-600 | 0.02 | 14 |
| $PrBa_{0.5}Sr_{0.5}Co_{1.5}Fe_{0.5}O_{5+\delta}$ | - | 0.009 | 0.018 | 600 | 0.02 | 11 |
| $Ba_{0.95}La_{0.05}Fe_{0.8}Zn_{0.2}O_{3-\delta}$ | - | 0.023 | 0.046 | 400 | 0.016 | 12 |
| $Ba_{0.95}La_{0.05}Fe_{0.8}Zn_{0.2}O_{3-\delta}$ | - | 0.012 | 0.024 | 500 | 0.016 | 12 |
| $BaCo_{0.4}Fe_{0.4}Zr_{0.1}Y_{0.1}O_{3-\delta}$ | - | 0.095 | 0.019 | 500 | 0.0095 | 15 |

### 5-3-3 *In-situ* Mn K-edge EXAFS

The hydration/dehydration reactions of *C*-LSM73 are driven by the coupling of the association between oxygen vacancy and water and the carriers exchange between oxygen hole and water protons, as represented in Equation (5-1).[9]

$$\mathrm{Mn(III)}_{\mathrm{Mn}}^{\times} + V_O^{\cdot\cdot} + \mathrm{O}_{\mathrm{O}}^{\cdot} + \mathrm{H_2O} \leftrightarrow \mathrm{Mn(IV)}_{\mathrm{Mn}}^{\cdot} + 2\mathrm{OH}_{\mathrm{O}}^{\cdot} \qquad (5\text{-}1)$$

In Equation (1), the Kröger–Vink notation is used, with $\mathrm{OH}_{\mathrm{O}}^{\bullet}$ being the proton defect, $\mathrm{O}_{\mathrm{O}}^{\cdot}$ the oxygen hole, $\mathrm{Mn(III)}_{\mathrm{Mn}}^{\times}$ Mn(III) cations on Mn site, $\mathrm{Mn(IV)}_{\mathrm{Mn}}^{\cdot}$ Mn(IV) cations on Mn site, and $V_O^{\bullet\bullet}$ the oxygen vacancy.

In proton-conducting ceramic electrolytes, such as $BaZr_{1-x-y}Ce_xY_yO_3$, the proton carriers are incorporated via the association between oxygen vacancies and water

molecules, as represented in Equation (5-2). [16,17,18]

$$O_O^X + V_O^{\bullet\bullet} + H_2O_{(g)} \leftrightarrow 2OH_O^{\bullet} \quad (5\text{-}2)$$

Here, $O_O^X$ is the lattice oxygen. In metal oxides, the association between oxygen vacancies and oxygen gas is in equilibrium.

$$V_O^{\bullet\bullet} + 1/2\ O_2 \rightarrow O_O^X + 2\ h^{\bullet} \quad (5\text{-}3)$$

Here, $h^{\bullet}$ is an electron hole. If the hole carriers are incorporated into the valence band comprising mainly of O *2p* states, Equation (5-3) can be rewritten with an oxygen hole ($O_O^{\cdot}$). [19,20]

$$V_O^{\bullet\bullet} + 1/2\ O_2 + O_O^X \rightarrow 2\ O_O^{\cdot} \quad (5\text{-}4)$$

In the case of LSM, the association between $V_O^{\bullet\bullet}$ and $O_2$ gas involves valence change in Mn cations.[21] Therefore, reaction (5-2) can be modified as follows:

$$V_O^{\bullet\bullet} + 1/2\ O_2 + 2Mn(III)_{Mn}^{\times} \rightarrow O_O^X + 2Mn(IV)_{Mn}^{\cdot} \quad (5\text{-}5)$$

The proton and hole carriers are in equilibrium as follows.

$$H_2O + 2\ O_O^{\cdot} \rightarrow 2\ OH_O^{\cdot} + 1/2\ O_2 \quad (5\text{-}6)$$

Coupling Equations (5-4) and (5-6) gives Equation (5-2). Moreover, combining Equations (5-4) and (5-5) yields the charge disproportionation as

$$Mn(III)_{Mn}^{\times} + O_O^{\cdot} \leftrightarrow Mn(IV)_{Mn}^{\cdot} + O_O^X \quad (5\text{-}7)$$

Therefore, Equation (5-1) can be interpreted by coupled reactions of the water–vacancy association (Equation (5-2)) and the charge disproportionation (Equation (5-7)). In fact, we demonstrated the valence change of O and Mn atoms for the hydration of C- LSM73 by means of synchrotron X-ray adsorption spectroscopy.[9]

To elucidate the average Mn valence state change and local structure rearrangements by hydration/dehydration reactions with the charge disproportionation, an extended X-

ray absorption fine structure (EXAFS) analysis was conducted for LSMN oxides with the reference samples of $LaMnO_3$ and $CaMnO_3$. Figure 5-5 shows the normalized absorption in the X-ray adsorption near edge structure (XANES) region of the pristine *C*-LSMN and *R*-LSMN samples, along with the reference samples of $LaMnO_3$ and $CaMnO_3$ at 415 °C. These oxides exhibit a weak pre-edge peak at approximately 6540 eV (Figure 5-5), attributed to the electric dipole forbidden transition of *1s* electron to an unoccupied *3d* orbital, and subsequently, yield a vertically rising main edge with a maximum peak at approximately 6553 eV corresponding to the electron transition from *1s* to *4p* orbitals.[9,22] In the *K*-edge XANES of manganese oxides, the adsorption edge shifts to higher energy in proportion to the average Mn valence states, since the core electron binding energy linearly increases with the positive charges on the cations.[37,38] Hence, a relative shift in comparison to reference materials, called the chemical shift, allows determining the average Mn valence states of these oxides if the crystal structures are analogous each other.[23-25] Previously, we evaluated the Mn valence state in perovskite-type $La_{1-x}Sr_xMnO_{3-\delta}$ series by combining the iodometry for a quenched sample and the chemical shifts of the Mn *K*-edge XANES,[33] confirming that Mn *K*-edge monotonically increases in proportion to the oxidation states of Mn cations; thus, the valence states could be properly determined with the calibration lines prepared by $LaMnO_3$ and $CaMnO_3$ references. Based on this, the Mn valence state of $La_{1-x}Sr_xMn_{1-y}Ni_yO_{3-\delta}$ was determined from the chemical shift of Mn K-edge by fixing the Mn valence states of $LaMnO_3$ and $CaMnO_3$ references at 415 °C in dry air to +3.20 and +3.99, respectively.[29,41]

Figures 5-6a–d show the normalized absorption in the XANES region of *C*-LSMN and *R*-LSMN, measured during dry/wet atmosphere switching in air at 415 °C. The absorption edge positions of *C*-LSMN7391 and *C*-LSMN7373 shift from 6549.98 and 6550.28 eV to 6550.22 and 6550.78 eV, respectively, when switching from dry to wet air (Figures 5-6a and b), resulting in an increase in the average Mn valence state from

3.17 and 3.26 to 3.24 and 3.40 for *C*-LSMN7391 and *C*-LSMN7373, respectively (Figure 5-6i). However, *R*-LSMN7391 and *R*-LSMN7373 do not exhibit chemical shifts throughout the dry/wet switching (Figures 5-6c and d), and thus, their average Mn valence states remain at 3.31 and 3.39, respectively, (Figure 5-6i and Table 5-2).

The Ni K-edge XANESs for C- and R-LSMN at 415 °C in dry air overlap with each other, and their adsorption edge positions are higher than that of NiO but identical to that of $LaNiO_3$ reference, indicating that Ni nominally takes +3 valence state in all LSMN regardless of the structure (cubic or rhombohedral) (Figure 5-7). In addition, the *in situ* Ni K-edge XANES spectra show that Ni does not change to a higher valence state via hydration (Figure 5-8), confirming Ni cations of all LSMN remain in 3+ valence state throughout the hydration/dehydration reaction at approximately 400 °C. We conclude that *C*-LSMN undergoes hydration/dehydration coupled with Mn redox by Equation (1) as is the case with the corresponding reaction of *C*-LSM73.[33]

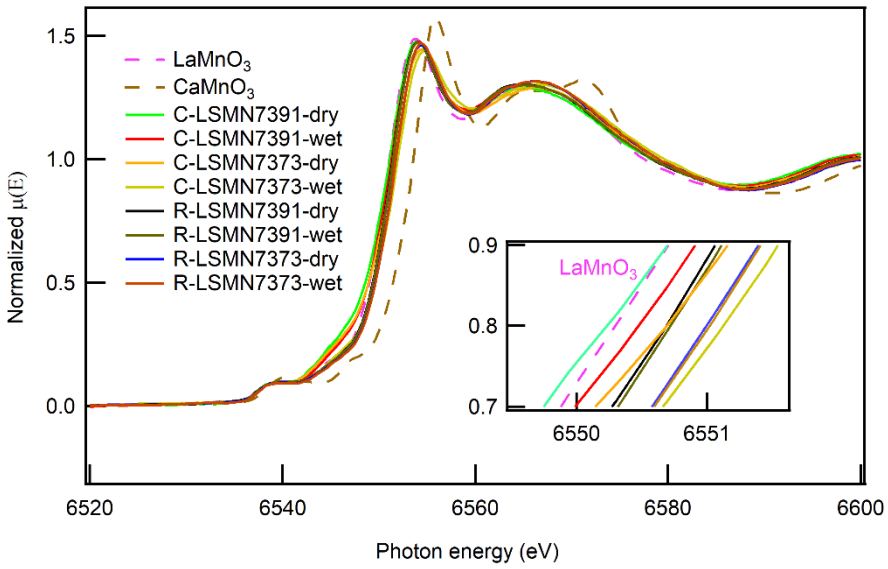


Figure 5-5 Mn K-edge XANES spectra of $La_{0.7}Sr_{0.3}Mn_{1-x}Ni_xO_{3-\delta}$ and reference samples $LaMnO_3$ and $CaMnO_3$ taking +3.20 and +3.99 valence states, determined by iodometry, respectively, at 415 ℃ under dry and wet air. The inset shows expansion of adsorption edge region.

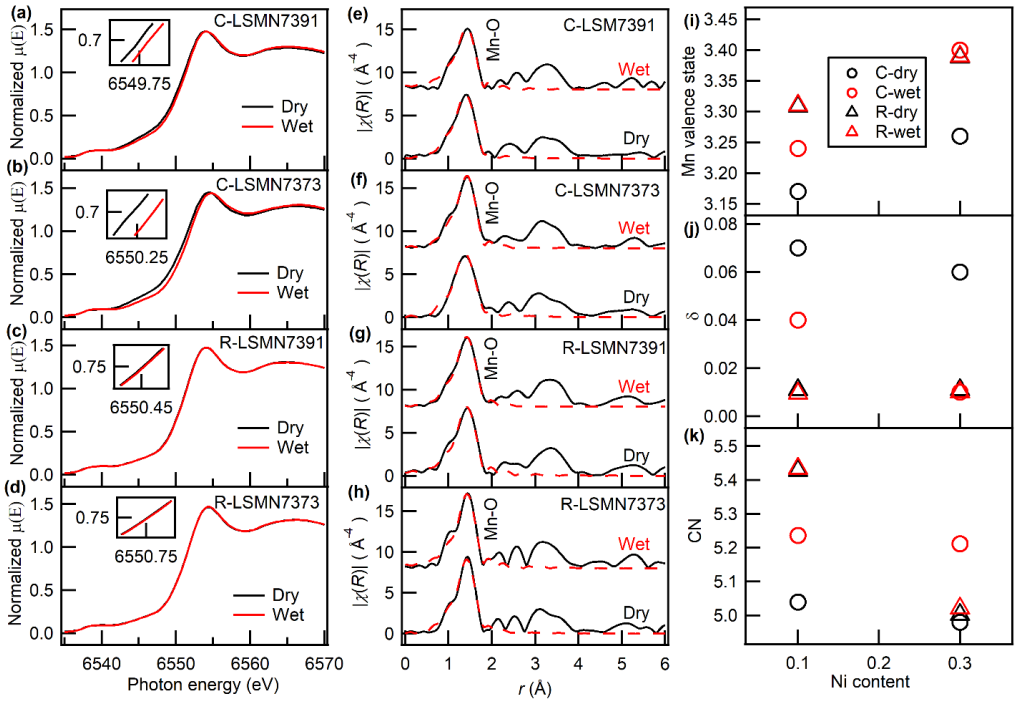


Figure 5-6 *In situ* Mn *K*-edge XANES spectra of (a) *C*-LSMN7391, (b) *C*-LSMN7373, (c) *R*-LSMN7391, and (d) *R*-LSMN7373 in a cycle of dry and wet air supplied at 415 °C. Insets of (a)–(c) show the enlarged absorption edge region. Radial distribution functions obtained by Fourier transforming the EXAFS at 415 °C under dry air for (e) *C*-LSMN7391, (f) *C*-LSMN7373, (g) *R*-LSMN7391, and (h) *R*-LSMN7373. In (e)–(h), the black and red lines indicate the observed and curve-fitting profiles to the 1st coordination shell (Mn-O), respectively. (i) Average Mn valence state determined from the chemical shift of absorption edges depicted in (a–d). (j) Oxygen deficiency (δ) calculated from the valence states of cations. (k) Oxygen-coordination number (*CN*) of Mn cations determined by EXAFS fitting analysis depicted in (e–h). In (i)–(k), the circular and triangular symbols indicate cubic and rhombohedral phases, and the black and red colors help distinguish between dry and wet atmospheres, respectively.

Table 5-2 Analytical results by EXAFS fitting and iodometry.

| Samples | Conditions | Mn valence state[c] | $\delta$ | *CN* | r/Å | *DW* | Mn valence state (iodometry)[d] | $\delta$ (iodometry)[d] |
|---|---|---|---|---|---|---|---|---|
| *C*-LSMN7391 | dry | 3.17 | 0.07 | 5.04±0.55 | 1.91 | 0.008±0.001 | 3.25 | 0.03 |
| | wet | 3.24 | 0.04 | 5.24±0.47 | 1.90 | 0.008±0.001 | 3.33 | -0.005 |
| *C*-LSMN7373 | dry | 3.26 | 0.06 | 4.98±0.62 | 1.90 | 0.007±0.002 | 3.32 | 0.03 |
| | wet | 3.40 | 0.01 | 5.21±0.56 | 1.91 | 0.007±0.001 | 3.44 | -0.01 |
| *R*-LSMN7391 | dry | 3.31 | 0.01 | 5.43±0.74 | 1.91 | 0.007±0.002 | 3.35 | -0.01 |
| | wet | 3.31 | 0.01 | 5.43±0.61 | 1.92 | 0.008±0.002 | 3.37 | -0.02 |
| *R*-LSMN7373 | dry | 3.39 | 0.01 | 5.00±0.50 | 1.90 | 0.006±0.001 | 3.45 | -0.02 |
| | wet | 3.39 | 0.01 | 5.02±0.72 | 1.89 | 0.006±0.002 | 3.48 | -0.035 |

[c] Mn Valence state and oxygen deficiency determined by XANES analysis.

[d] Mn Valence state and oxygen deficiency calculated determined by iodometry. The negative sign represents the oxygen excess (for example, -0.005 means the oxygen stoichiometry is 3.005).

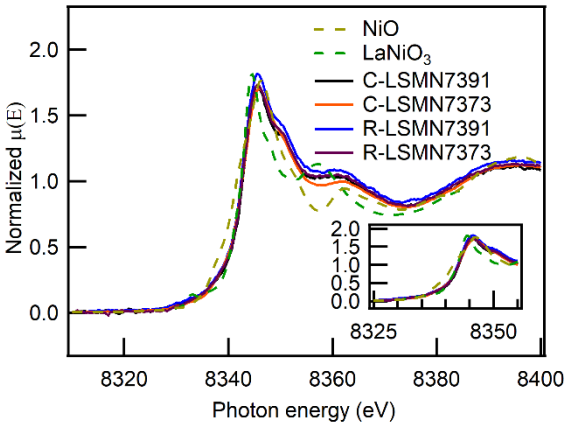


Figure 5-7 Ni K-edge XANES spectra of $La_{0.7}Sr_{0.3}Mn_{1-x}Ni_xO_{3-\delta}$ and reference samples NiO and $LaNiO_3$ taking +2 and +3 valence states, respectively, at 415 °C under dry air. The inset shows expansion of adsorption edge region.

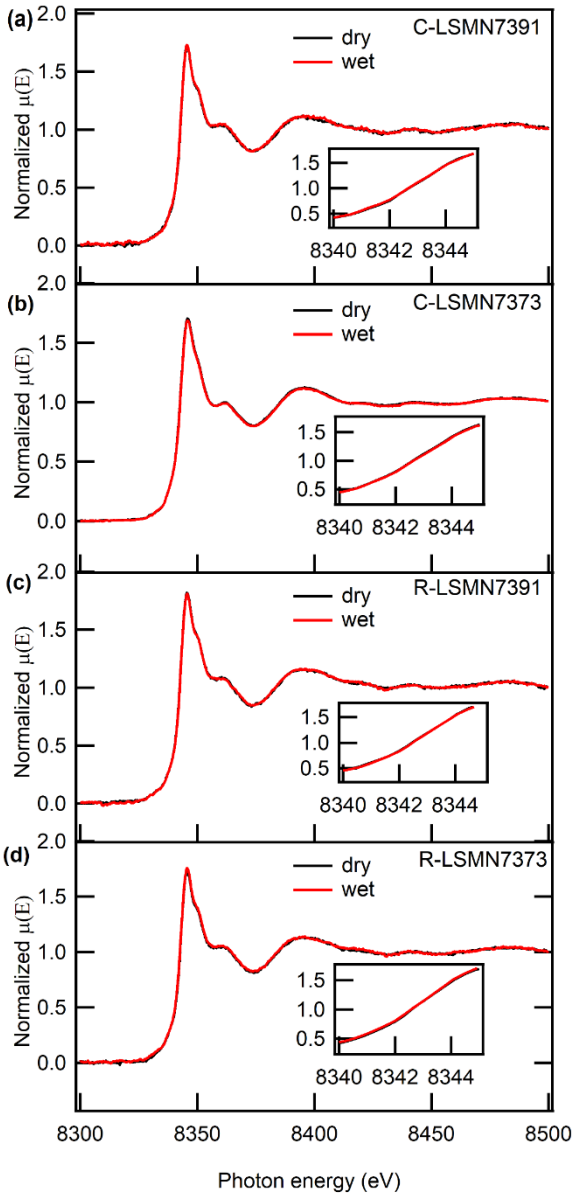


Figure 5-8 *In-situ* Ni *K*-edge XANES spectra of (a) *C*-LSMN7391, (b) *C*-LSMN7373, (c) *R*-LSMN7391 and (d) *R*-LSMN7373 in a cycle of dry and wet air supply at 415 ℃. Insets of (a)-(c) show the enlarged absorption edge regions.

Figures 5-6e–h show the radial distribution function (RDF) obtained from the Fourier transform EXAFS. For the LSMN oxides, the first coordination shells corresponding to an intense peak in the range of approximately 1.6–2.0 Å can be attributed to the shortest shell of Mn−O bond, and the second and the third shells distributed in the range of 2.0–4.0 Å can be assigned to the coherence in Mn−La or Mn−Sr and in Mn−Mn.[33] The curve fitting analysis to the first Mn−O coordination shell of *C*-LSMN converged well when using the atomic coordinates of cubic or rhombohedral perovskite $LaMnO_3$ as an initial set, yielding a Mn-O distance (*r*) of approximately 1.9 Å. It has been widely recognized that EXAFS normally underestimates *CN* around metal atoms because of the annihilation by other heavy atoms and large contribution of Debye-Waller factor.[26] Meanwhile, the *CN* around Mn exhibits the apparent trend of increasing by hydration: the values of *C*-LSMN7391 and *C*-LSMN7373 change from 5.04±0.55 and 4.98±0.62 to 5.24±0.47 and 5.21±0.56, respectively (Figure 5-6k; Table 2). Regardless of the relatively large errors, these results imply that oxygen vacancies of the *C* phase decrease via hydration. This feature is also supported by Rietveld refinement on powder XRD patterns, because the site occupancy of O atoms significantly increases by hydration in *C* phase with the lattice shrinkage due to the increase in Coulombic attraction between oxide and metal ions (Figure 5-9; Table 5-3 and 5-4).[10]

Un-hydrated *R* phase (*R*-LSMN7391 and *R*-LSMN7373) maintains *CN* at a constant value (5.43±0.74 (0.61) and 5.00±0.50 (0.72), respectively) irrespective of the humidity (Figures 5-6k and Table 5-2). These results prove that $H_2O$ is incorporated by the association between water molecules and oxygen vacancies according to equation (5-1).

The oxidation states of Mn cations in LSMN oxides were also examined by iodometry. For the analysis, all powder specimens were once annealed in dry and wet air at 415 °C for 6 h, quenched in desiccator, and immediately dissolved into 0.1 M HCl solutions. The chemical analysis results in Mn valence states equaling to 3.25 and 3.33

for *C*-LSMN7391 in dry and wet air, respectively, and 3.35 and 3.37 for the corresponding *R* phase in dry and wet air, respectively (Figure 5-10 and Table 5-2). Similarly, it gives 3.32 and 3.44 for *C*-LSMN7373 in dry and wet air, respectively, and 3.45 and 3.48 for the *R* phase in dry and wet air, respectively. These values are in close agreement with ones determined by Mn *K*-edge XANES, which validates the results of EXAFS measurements.

Oxygen vacancies are crucial to hydration/dehydration reactions according to Equation (5-1). EXAFS and iodometry analysis verify that cubic phase possesses sufficient amount of oxygen vacancies in dry atmosphere. Oxygen deficiency ($\delta$) in $La_{0.7}Sr_{0.3}Mn_{1-x}Ni_xO_{3-\delta}$ is roughly calculated with the Mn valence state determined by XANES and iodometry, assuming that the net charges on La, Sr, Ni, and O are fixed at +3, +2, +3, and −2, respectively (Figures 5-6j and 5-10). Iodometry confirmed that $\delta$ in dry air (0.03) is almost equivalent with one in dry Ar (0.02) for C-LSMN7391, meaning that $\delta$ is not sensitive to $p_{O2}$. Several groups have also reported that $\delta$ of $La_{0.7}Sr_{0.3}MnO_{3-\delta}$ (LSM73) remains unchanged with $p_{O2}$, keeping nearly 0 in the $p_{O2}$ region from $10^5$ to 0.1 Pa at temperatures below 600 °C.[41,27] This would be due to the relatively large value of oxygen vacancy formation enthalpy ($\Delta H$ ~ 115 kJ $mol^{-1}$),[27] which results in very small value of $\exp(-\Delta H/RT)$ in the relatively low temperature range with a gas constant *R*. The $\delta$ values of dehydrated *C*-LSM7391 and *C*-LSMN7373 are determined to 0.07 and 0.06, respectively, by XANES and to 0.03 and 0.03, respectively, by iodometry (Table 5-2).

On the other hand, XANES yield relatively small $\delta$ values (~0.01) for both dehydrated *R*-LSMN7391 and *R*-LSMN7373, and, moreover, iodometry indicates the oxygen excess in both *R* phase. Thus, they would not undergo hydration because of the low concentration of oxygen vacancies, unlike *C*-LSMN with abundant oxygen vacancies.

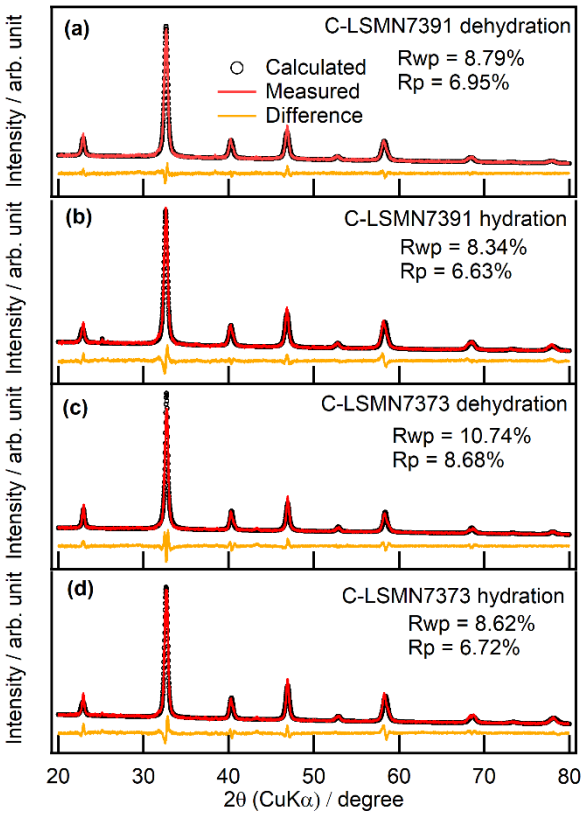


Figure 5-9 Rietveld refinement profiles for hydrated and dehydrated *C*-LSMN7391 and *C*-LSMN7373 assuming models of cubic (*Pm-3m*, #221). Here, the *C*-LSMN was annealing under dry and wet air at 415 ℃ to obtain dehydrated and hydrated samples.

Table 5-3. Lattice constants and *R* factors refined by Rietveld analysis for hydrated and dehydrated *C*-LSMN.

| Samples | Space group | a=b=c (Å) | α=β=γ | $R_{wp}$ | $R_p$ |
|---|---|---|---|---|---|
| C-LSMN7391 (dehydrated) | Pm-3m | 3.878 | 90° | 8.79% | 6.95% |
| C-LSMN7391 (hydrated) | Pm-3m | 3.867 | 90° | 8.34% | 6.63% |
| C-LSMN7373 (dehydrated) | Pm-3m | 3.872 | 90° | 10.74% | 8.67% |
| C-LSMN7373 (hydrated) | Pm-3m | 3.866 | 90° | 8.62% | 6.72% |

Table 5-4. Atomic coordinates and site occupancies refined by Rietveld analysis for hydrated and dehydrated *C*-LSMN.

| Samples | Elements | *x* | *y* | *z* | Occupancy | $U_{iso}$ / Å$^2$ |
|---|---|---|---|---|---|---|
| *C*-LSMN7391 (dehydrated) | La | 0 | 0 | 0 | 0.711 | 0.084 |
| | Sr | 0 | 0 | 0 | 0.302 | 0.052 |
| | Mn | 0.5 | 0.5 | 0.5 | 0.904 | 0.08 |
| | Ni | 0.5 | 0.5 | 0.5 | 0.099 | 0.129 |
| | O | 0 | 0.5 | 0.5 | 0.956 | 0.040 |
| *C*-LSMN7391 (hydrated) | La | 0 | 0 | 0 | 0.714 | 0.030 |
| | Sr | 0 | 0 | 0 | 0.294 | 0.003 |
| | Mn | 0.5 | 0.5 | 0.5 | 0.916 | 0.026 |
| | Ni | 0.5 | 0.5 | 0.5 | 0.099 | 0.003 |
| | O | 0 | 0.5 | 0.5 | 1.013 | 0.001 |
| *C*-LSMN7373 (dehydrated) | La | 0 | 0 | 0 | 0.701 | 0.008 |
| | Sr | 0 | 0 | 0 | 0.302 | 0.005 |
| | Mn | 0.5 | 0.5 | 0.5 | 0.695 | 0.013 |
| | Ni | 0.5 | 0.5 | 0.5 | 0.295 | 0.020 |
| | O | 0 | 0.5 | 0.5 | 0.965 | 0.013 |
| *C*-LSMN7373 (hydrated) | La | 0 | 0 | 0 | 0.705 | 0.014 |
| | Sr | 0 | 0 | 0 | 0.302 | 0.076 |
| | Mn | 0.5 | 0.5 | 0.5 | 0.716 | 0.027 |
| | Ni | 0.5 | 0.5 | 0.5 | 0.296 | 0.076 |
| | O | 0 | 0.5 | 0.5 | 1.042 | 0.025 |

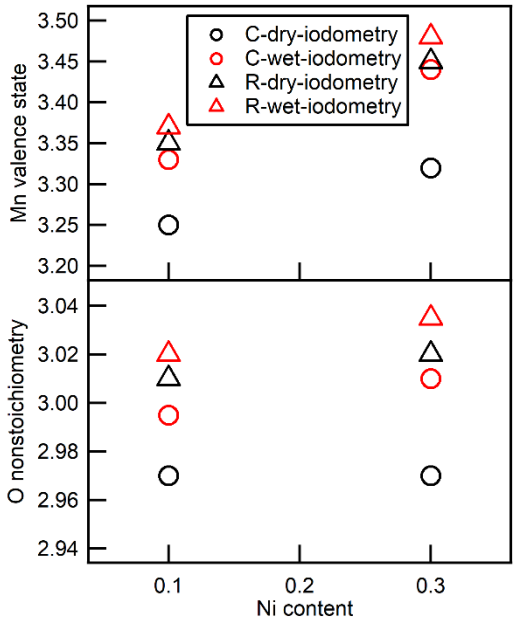


Figure 5-10. Mn valence state and oxygen nonstoichiometry determined by iodometry for C- and R-LSMN oxides annealed in dry and wet air at 415 ℃ for 6 h.

### 5-3-4 Hydration ability of LSMN

The hydration capability ($\Delta n$), which is defined as the mole fraction of water absorbed (($n$($H_2O$)) to $n$($La_{0.7}Sr_{0.3}Mn_{1-x}Ni_xO_{3-\delta}$) ($\Delta n$ =$n$($H_2O$) / $n$(LSMN)), can be roughly estimated from the $\Delta W$ values. Here, the molecular formulae of dehydrated *C*-LSMN7391 and *C*-LSMN7373 are assumed to be $La_{0.7}Sr_{0.3}Mn_{0.9}Ni_{0.1}O_{2.93}$ and $La_{0.7}Sr_{0.3}Mn_{0.7}Ni_{0.3}O_{2.94}$, respectively, using $\delta$ as calculated above. The $\Delta n$ values of *C*-LSMN7391 and *C*-LSMN7373 are 0.055 and 0.098, respectively, in air (Table 5-1), which are consistent with the values expected from Mn valence changes (0.07 and 0.14 for *C*-LSMN7391 and *C*-LSMN7373, respectively; Figure 5-6i; Table 2) through hydration/dehydration reactions. The resultant proton concentrations of *C*-LSMN7391 and *C*-LSMN7373 are 0.102 and 0.160, respectively, in Ar and 0.11 and 0.196, respectively, in air. Surprisingly, these values are comparable to the proton concentrations of well-known proton conductors $BaCe_{0.9}Y_{0.1}O_3$ (~0.1) and $BaZr_{0.9}Y_{0.1}O_3$ (~0.08) under wet $N_2$ atmosphere ($p_{H2O}$ = 0.023 atm) at 600 °C.[12]

Both *C*-LSMN7391 and *C*-LSMN7373 tend to have larger $\Delta n$ in air rather than that in Ar. Equilibrium constant of equation (5-1) $k_1$, is given by:

$$k_1 = \frac{[Mn^{4+}] \cdot [\mathrm{OH}_{\mathrm{O}}^{\cdot}]^2}{[Mn^{3+}] \cdot [V_O^{\bullet\bullet}] \cdot [\mathrm{O}_{\mathrm{O}}^{\cdot}] \cdot p_{H2O}} \qquad (5\text{-}8)$$

Equilibrium constant of equation (5-4), $k_4$, is given by:

$$k_4 = \frac{[\mathrm{O}_{\mathrm{O}}^{\cdot}]^2}{[V_O^{\bullet\bullet}] \cdot [\mathrm{O}_{\mathrm{O}}^{\mathrm{x}}] \cdot p_{O2}} \qquad (5\text{-}9)$$

Combined (5-8) and (5-9), the proton concentration $[\mathrm{OH}_{\mathrm{O}}^{\cdot}]$ can be represented as follows.

$$[OH_O^{\cdot}]^2 = \frac{k_1 \cdot \sqrt{k_4} \cdot [Mn^{3+}] \cdot \sqrt{[V_O^{\bullet\bullet}]^3} \cdot \sqrt{[\mathrm{O}_{\mathrm{O}}^{\mathrm{x}}]} \cdot \sqrt[4]{p_{O2}} \cdot p_{H2O}}{[Mn^{4+}]} \qquad (5\text{-}10)$$

In a separate experiment, the *C* phase was confirmed to have the same $[Mn^{3+}]/[Mn^{4+}]$ ratio in both Ar and air atmosphere at 415 ℃ by means of XANES. $[V_O^{\bullet\bullet}]$ of LSMN is almost constant in the $p_{O2}$ range from $10^{-4}$ to $10^{5}$ Pa at temperatures below 600 ℃, as mentioned above. Hence, equation (5-10) suggests $[OH_O^{\cdot}]$ thus increases with $p_{O2}$ at a fixed $p_{H2O}$ attributed to the increase of $[O_O^{\cdot}]$ in equation (5-6). This feature is consistent with the observed $p_{O2}$ dependence of $\Delta n$. These provide a verification that *C*-LSMN undergoes bulk hydration by equation (5-1) coupled of equation (5-2) and (5-7).

Figure 5-11 shows the transmittance IR spectroscopy of O–H stretching modes of *C*- and *R*-LSMN7373 in the wavenumber range of 3100–3500 $cm^{-1}$, measured at elevated temperatures in wet air. The absorption band of O–H stretching is evident even at 600 °C in *C*-LSMN7373, however, it disappears at temperatures above 400 °C in the *R* phase. Hence the *C* phase is confirmed to be hydrated, retaining protonic defects, near the operation temperatures of PCFCs.

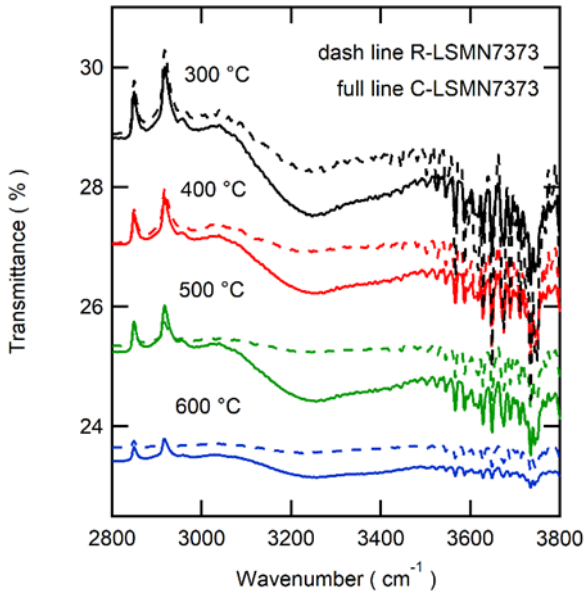


Figure 5-11 Transmittance IR spectra of hydroxyl stretching modes for C- and R-LSMN7373 at elevated temperatures (300-600 ℃) in wet air. The full and dashed lines indicate C and R phase, respectively.

### 5-3-5 Performances of LSMN cathodes on PCFCs

The bulk hydration ability of *C*-LSMN ensures proton conduction at intermediate temperatures, though the conductivity remains unclear. Hence, these oxides are attractive for PCFC cathodes in the intermediate temperature region of 500–600 °C. We examined the performance of PCFCs with *C*-LSMN porous cathodes by fabricating anode-supported thin film cells based on a $BaZr_{0.4}Ce_{0.4}Y_{0.2}O_3$ (BZCY442) electrolyte. The anode/electrolyte half cells were fabricated by single-step co-sintering process (as reported elsewhere); the porous cathode layer was deposited on electrolyte thin films by screen-printing and subsequent annealing at 700 °C.[28] The XRD patterns of the pulverized half cells show no formation of impurity phases on the anode and electrolyte (Figure 5-12). The grain size of highly dense BZCY442 electrolytes is approximately 7 μm (Figure 5-13a), and their thickness is approximately in the range of 18–19 μm for the measured cells (Figure 5-13c). The anode maintains good porosity to provide enough sites for hydrogen reduction (Figure 5-13b). For comparison, we examined the cells with *C*-LSM73 and $La_{0.6}Sr_{0.4}Co_{0.2}Fe_{0.8}O_3$ (LSCF6428) cathodes on BZCY442 based anode-supported cells with largely the same electrolyte thickness. The SEM images of these cathodes (Figure 5-14) were taken after they were annealed for 2 h at 700 ℃; all of them have similar microstructure. The primary particle sizes are less than 100 nm for all specimens.

Figures 5-15a–e show the current–voltage–power (*I–V–P*) curves for the PCFCs with various cathodes in the temperature range of 500–700 °C. The open circuit voltages (OCVs) of *C*– and *R*–LSMN at 500–700 ℃ are listed in Table 5-5 together with the theoretical OCVs. All LSMN cells exhibit smaller OCV values than the theoretical ones at temperatures above 600°C, attributed to the increased hole conductivity of BZCY442 electrolytes.[17] OCVs of *C* phase are slightly higher than those of *R* phase and LSCF6428. Particularly, C-LSMN7373 cell gives the similar OCV (1.12 V) as the theoretical value (1.16 V) at 500°C, while LSCF6428 cell show the OCV below 1.0 V, which implies

that proton conductivity of the cathode reduces the migration of holes into electrolyte.

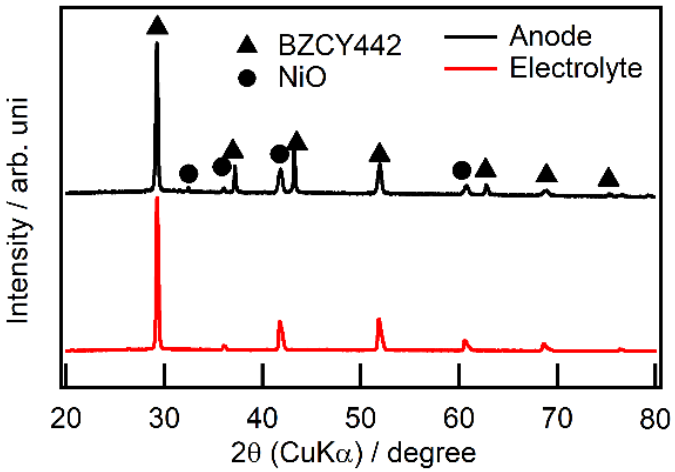


Figure 5-12 XRD patterns of anode and electrolyte for pulverized anode supported half cells based on BZCY442 electrolyte.

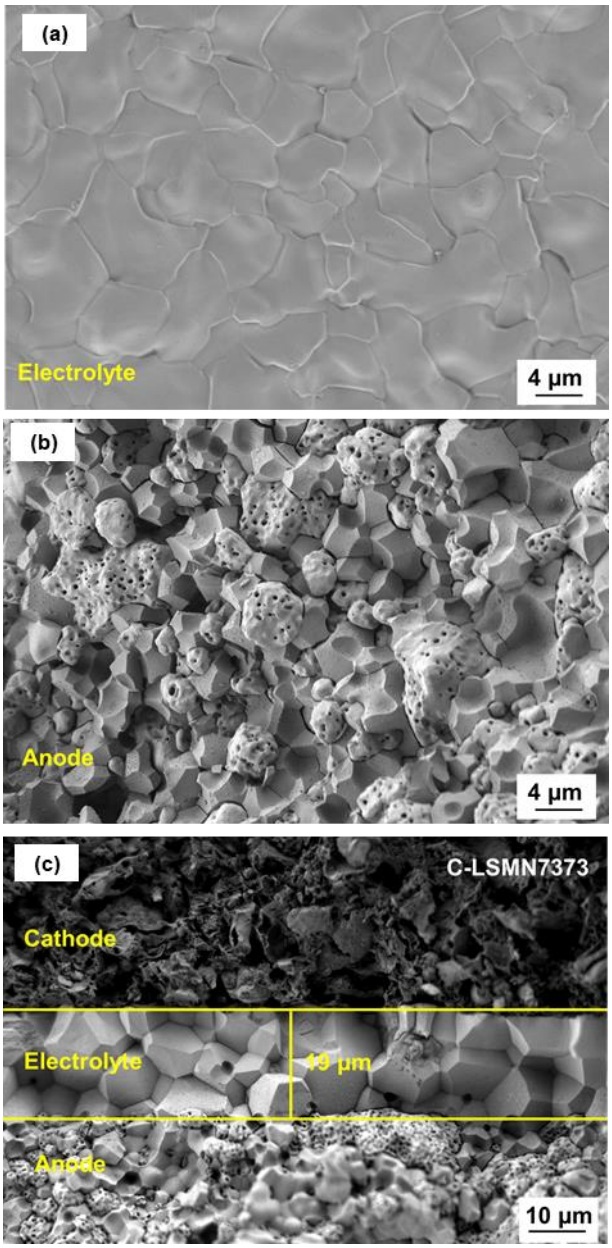


Figure 5-13 SEM images for the (a) surface of electrolyte, (b) cross section of anode, and (c) cross section of anode-supported cells with *C*-LSMN7373 cathode.

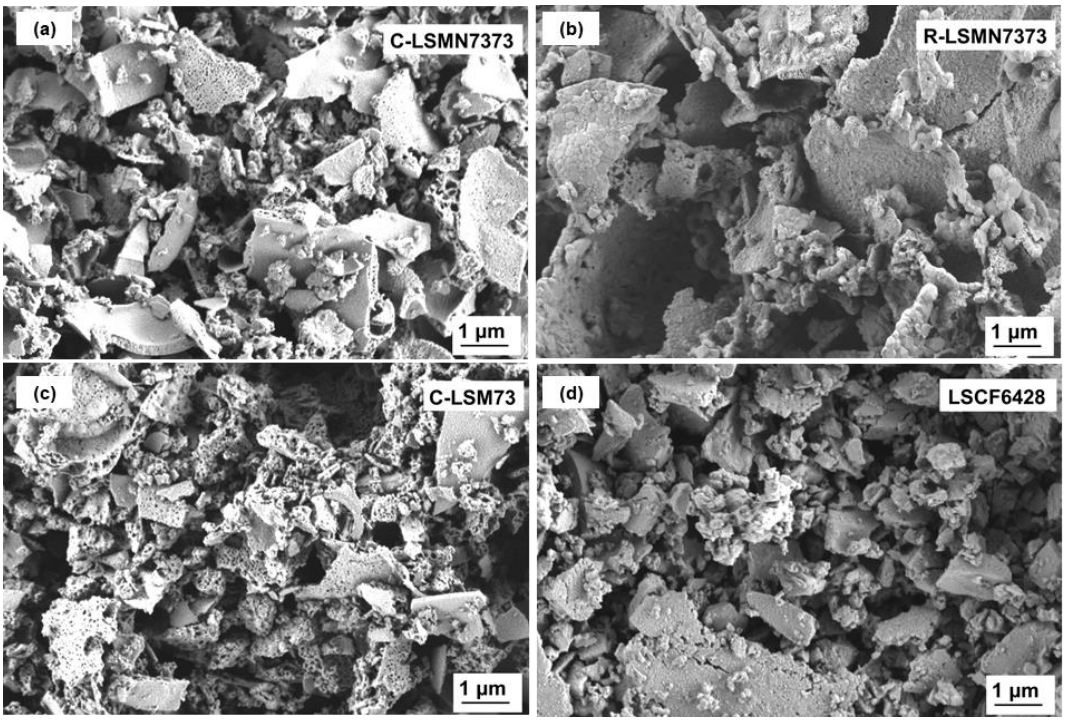


Figure 5-14. SEM images of (a) *C*-LSMN7373, (b) *R*-LSMN7373, (c) *C*-LSM73, and (d) LSCF6428 cathodes after annealed at 700 ℃ for 2 hours.

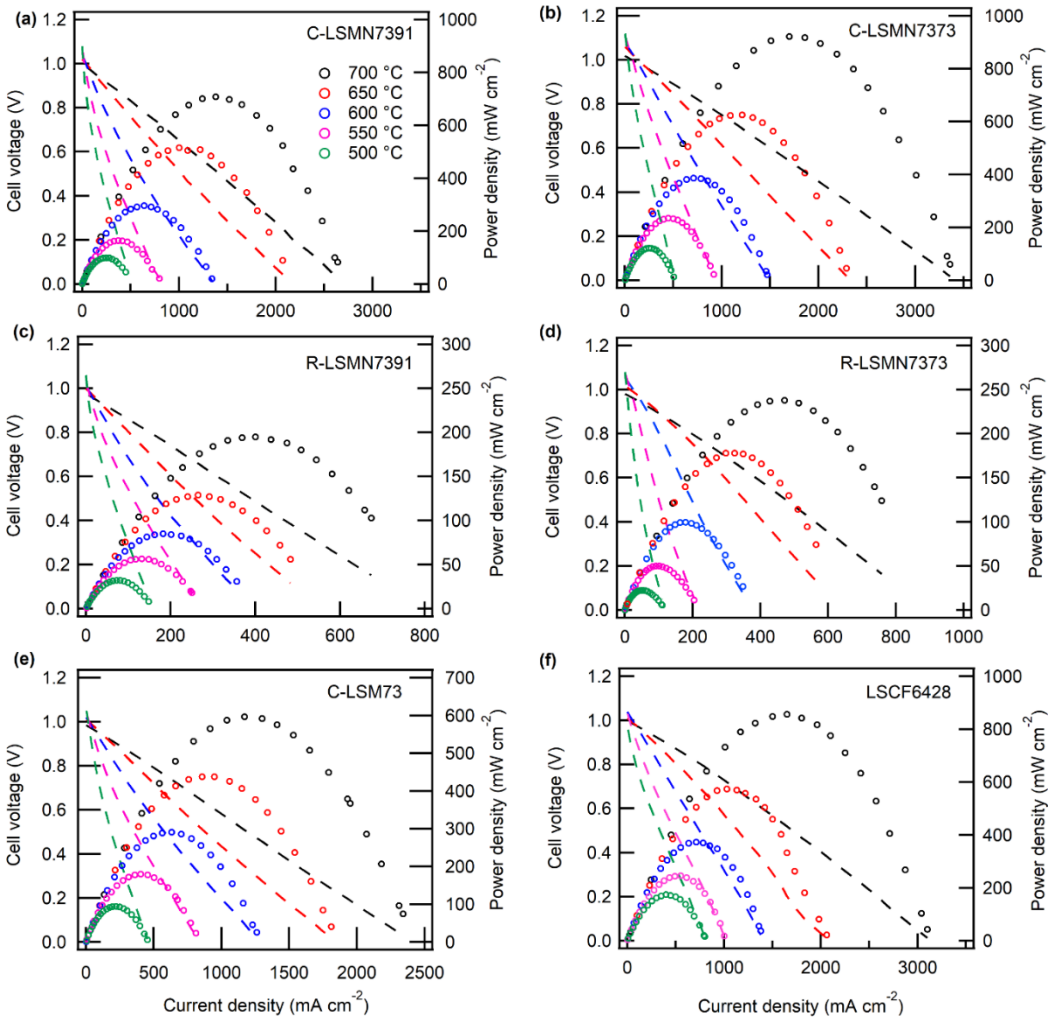


Figure 5-15 *I–V* and *I–P* curves of PCFCs with cathodes *C*-LSMN7391 (a), *C*-LSMN7373 (b), *R*-LSMN7391 (c), *R*-LSMN7373 (d), C-LSM73 (e), and LSCF6428 (f), in the temperature range of 500–700 °C.

Table 5-5. Theoretical and observed open circuit voltages (OCVs) of PCFCs with LSMN and LSCF cathodes at 700, 600 and 500 ℃.

| OCVs | Theoretical | C-LSMN7391 | C-LSMN7373 | R-LSMN7391 | R-LSMN7373 | LSCF6428 |
|---|---|---|---|---|---|---|
| 700 ℃ | 1.140 | 0.99 | 1.02 | 0.97 | 0.98 | 0.99 |
| 600 ℃ | 1.152 | 1.03 | 1.08 | 1.00 | 1.05 | 1.04 |
| 500 ℃ | 1.164 | 1.08 | 1.12 | 1.06 | 1.08 | 0.98 |

The power densities of the PCFCs with a *C*-LSMN cathode (Figures 5-15a and b) are much higher than those with a *R*-LSMN cathode in both LSMN7391 and LSMN7373 at all temperatures (Figures 6c and d). The peak power densities (PPDs) of the *C*-LSMN7391 and *C*-LSMN7373 cells at 700 °C are 708 and 992 mW $cm^{-2}$, respectively. At 600 °C, the PPDs for *C*-LSMN7391 and *C*-LSMN7373 are 296 and 386 mW $cm^{-2}$, respectively, which are two and three times greater than the values of the corresponding *R*-LSMN cells (84 and 100 mW $cm^{-2}$ at 600 ℃), respectively (Figure 5-16a; Table 5-6). Moreover, the PPD of the *C*-LSMN7373 cell is slightly higher than that of the cells with a widely-used cobaltite cathode LSCF6428 (373 mW $cm^{-2}$) at 600 ℃ (Figures 5-15f and 5-16a).

Recently, Choi *et al.* reported outstanding power outputs of a $BaZr_{0.4}Ce_{0.4}Y_{0.1}Yb_{0.1}O_3$ (BZCYYb4411)-based PCFC with $H^+/O^{2-}/e^-$ triple-conducting $PrBa_{0.5}Sr_{0.5}Co_{1.2}Fe_{0.8}O_3$ (PBSCF) cathode, in which the PPD exceeded 0.8 W $cm^{-2}$ at 600 °C.[8] Nevertheless, in most PCFCs comprising Zr-rich side $BaZr_xCe_{1-x-y}Y_yO_3$ solid solutions ($x > 1-x-y$), the PPD is in the range of 0.1–0.3 W $cm^{-2}$ at 600 °C with cobalt-oxide cathodes. [4-6, 28-32] Moreover, the performances of the fuel cells with Mn-based perovskite cathodes are normally much lower than those of the cells with cobalt-base cathodes at intermediate temperatures below 700 °C, because the relatively low oxide ion conductivity of the former limits the reaction rate at TPBs.[2,3,4] The *C*-LSMN cells exhibit similar or even superior fuel cell performances to the LSCF6428 ones, although the performance of the

*R*-LSMN cells is inferior to the LSCF one (Figure 5-16a; Table 5-6). This shows that the *C*-LSMN cathodes sufficiently decrease the cathodic polarization resistance owing to the formation of extended reaction area by proton conductivity.

Figures 5-17a-e show the electrochemical impedance spectra of each cell at 700, 650, 600, 550, and 500 ℃ under OCV conditions. In general, the Nyquist plots of impedance responses of PCFCs have the *x*-intercept in a high-frequency region, which corresponds to electrolyte resistances ($R_{ohm}$). After the intercept, they exhibit broad semi-arcs due to the interfacial polarization resistance at the cathode side,[3] and, the diameters of the arcs provide polarization resistance ($R_p$) at the cathode side. The diameters of the semi arcs of the fuel cells with *C*-LSMN cathodes are several times smaller than those of the cells with *R*-LSMN ones, revealing that $R_p$ of the former is much lower than that of the latter despite their similar chemical compositions. Figure 5-16b shows $R_p$ for various cathode-type cells, determined from the diameters of the impedance semi-arcs under OCV condition. The gap in $R_p$ of the *C*- and *R*-phase cathodes tends to increase with decreasing temperatures. The $R_p$ values of the *C*-LSMN7373 cell are 0.43 and 3.44 Ω $cm^2$ at 600 and 500 ℃, respectively, which are much lower than the corresponding values of the *R*-LSMN7373 cell (1.14 and 14.01 Ω·$cm^2$) by a factor of 2.6 and 4.1 at 600 and 500 ℃, respectively. Similarly, the $R_p$ values of the *C*-LSMN7391 cell are 0.68 and 3.60 Ω $cm^2$ at 600 and 500 ℃, respectively, which are lower than the corresponding values of the *R*-LSMN7391 cell. These features prove that the proton conductivity of *C*-LSMN cathodes efficiently lower the polarization resistances.

The *C*-LSM73 cathode exhibits higher $R_p$ than the Ni-substituted ones, and thus, the PPD of the *C*-LSM73 cell (291 and 95 mW $cm^{-2}$ at 600 and 500 ℃, respectively) is much lower than that with the *C*-LSMN7373 (Table 5-6; Figures 5-15b, e, and 5-16a). The valence state of Ni cation is lower than the average value of Mn cations (> +3) in all samples as confirmed by EXAFS, so that the concentration of the oxygen vacancies must increase, thus increasing the concentrations of proton carriers with Ni substitution

according to Equation (1). In fact, $\Delta n$ of *C*-LSM73 (0.07) is lower than that of *C*-LSMN7373 (0.098; Table 5-1). *C*- LSMN7373 outperforms the *C*-LSM73 cell probably because of the higher proton conductivity.

Figure 5-16c shows the Arrhenius plots of $R_p^{-1}$ for BZCY442 cells. The activation energies (*E*a) related to $R_p$ are 96.7 and 108 kJ mol$^{-1}$ for *C*-LSMN7391 and *C*-LSMN7373, respectively; these values are lower than those of the *R*-LSMN7391 (114.8 kJ mol$^{-1}$) and *R*-LSMN7373 (123.1 kJ mol$^{-1}$) cells (Table S4) and even lower than the widely used cathode materials, such as LSCF6428 (134.5 kJ mol$^{-1}$), $Pr_2NiO_4$ (102.9 kJ mol$^{-1}$),[5] and $BaZr_{0.4}Ce_{0.4}Y_{0.2}O_3$-$Ba_{0.5}Sr_{0.5}(Co_{0.8}Fe_{0.2})Ti_{0.9}O_{3-\delta}$ (BZCY-BSCFT; 100.2 kJ mol$^{-1}$).[6] $R_p$ of *C*-LSMN7373 cell is slightly larger than those of LSCF6428 one at temperatures above 600°C owing to relatively high *E*a of the latter (Figures 5-16b). Nevertheless, the former yields the similar PPDs as the latter, which is probably due to the relatively small hole leakage, as mentioned above (Figures 5-16a and c).

Finally, the durability of *C* phase was examined by conducting galvanostatic operation of fuel cells under 800 mA cm$^{-2}$ at 700 ℃. The cell yielded a stable output without degradation for 35 hours (Figure 5-18). XRD for the cathode after the durability test confirms that the oxide retains the cubic structure (Figure 5-19). As mentioned above, the superior cathode performances of *C*-LSMN to *R*-LSMN highlights that proton conduction in *C*-LSMN series helps sufficiently lower the cathodic polarization resistance by extending the effective reaction areas from proton-electron-gas TPB zones to the overall electrode surface (Figures 5-20a, b and c). In conclusion, cubic- type LSMN perovskites are beneficial to $H^+/O^{2-}/e^-$ triple-conducting cathodes, making them a promising Co-free cathode material for advanced PCFCs operating at intermediate temperatures.

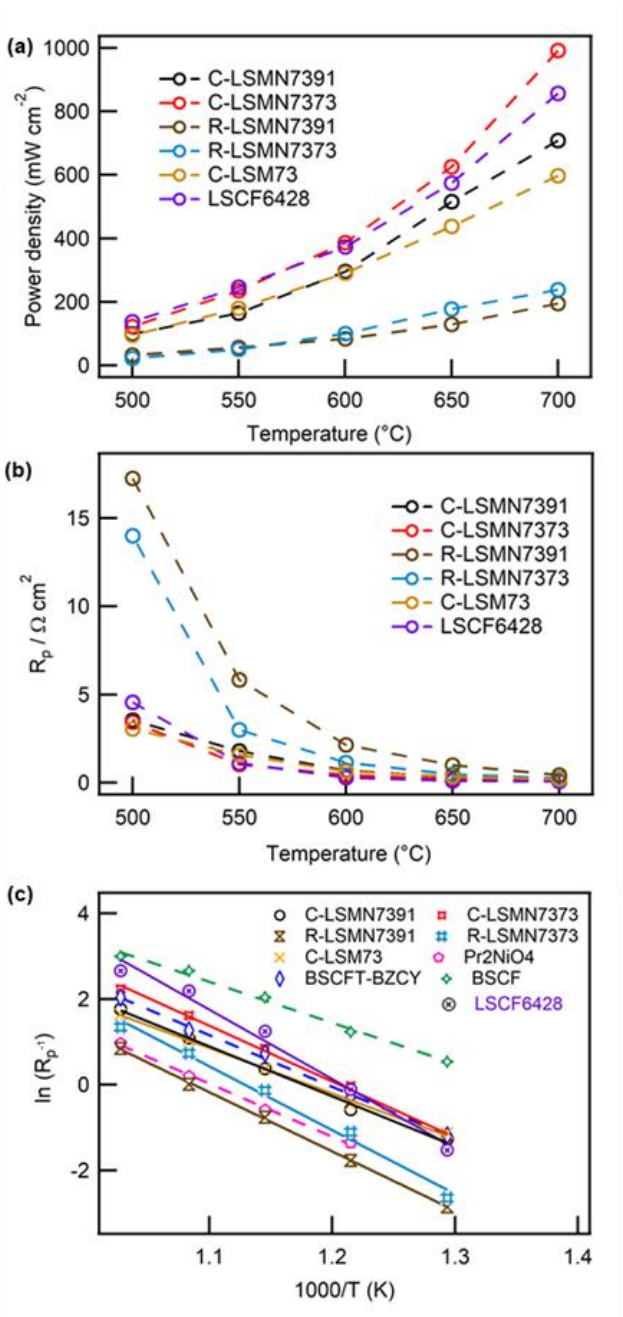


Figure 5-16 Plots of (a) peak power densities and (b) cathodic polarization resistance ($R_p$) as a function of the temperature. (c) Arrhenius plots of the reciprocal of $R_p$ for BZCY442-base PCFCs with various cathodes. In (c), the full lines are the ones measured in this work, whereas the dashed lines are the replots of data obtained previously for BSCF, $Pr_2NiO_4$, and BSCFT-BZCY, respectively.

Table 5-6 Performances of PCFCs comprising BZCY442 electrolyte with various cathodes at 600 ℃, and ones using $La_{1-x}Sr_xMnO_3$ cathodes at 600 ℃.

| Cathode | Electrolyte | Ea (kJ/mol) | PPD (mW $cm^{-2}$) | $R_p$ (Ω $cm^2$) | Ref |
|---|---|---|---|---|---|
| *C*-LSMN7391 | BZCY442 | 96.7 | 296 | 0.68 | This work |
| *C*-LSMN7373 | BZCY442 | 108.1 | 386 | 0.43 | This work |
| *R*-LSMN7391 | BZCY442 | 114.8 | 84 | 2.14 | This work |
| *R*-LSMN7373 | BZCY442 | 123.1 | 100 | 1.14 | This work |
| *C*-LSM73 | BZCY442 | 88.1 | 291 | 0.69 | This work |
| LSCF6428 | BZCY442 | 134.5 | 273 | 0.29 | This work |
| BSCF | BZCY442 | 79.5 | 276 | 0.74 | 7 |
| $Pr_2NiO_4$ | BZCY442 | 102.9 | 102 | 0.77 | 5 |
| BZCY-BSCFT | BZCY442 | 100.2 | 194 | 0.91 | 6 |
| BSCF | BZCY442 | - | 230 | - | 7 |
| BSCF | BZCY442 | - | 161 | 0.18 | 4 |
| LSM | BZCYYb4411 | - | 350 | - | 33 |
| LSM | BZCY622 | - | 17 | - | 1 |
| LSM6530 | BZYbCu | - | 51 | 0.55 | 2 |
| LSM82 | BCY85 | - | 80 | 7.3 | 3 |

Abbreviations: $La_{0.6}Sr_{0.4}Co_{0.2}Fe_{0.8}O_3$ (LSCF6428), $Ba_{0.5}Sr_{0.5}Co_{0.2}Fe_{0.8}O_3$ (BSCF), $Ba_{0.5}Sr_{0.5}(Co_{0.8}Fe_{0.2})_{0.9}Ti_{0.1}O_{3-\delta}$ (BZCY-BSCFT), $(La_{0.65}Sr_{0.3})MnO_{3-\delta}$ (LSM6530) , $La_{0.8}Sr_{0.2}MnO_3$ (LSM82), $BaZr_{0.4}Ce_{0.4}Y_{0.2}O_3$ (BZCY442), $BaZr_{0.4}Ce_{0.4}Y_{0.1}Yb_{0.1}O_3$ (BZCYYb4411), $Ba(Zr_{0.84}Yb_{0.15}Cu_{0.01})O_{3-\delta}$ (BZYbCu), $BaCe_{0.85}Y_{0.15}O_3$ (BCY85).

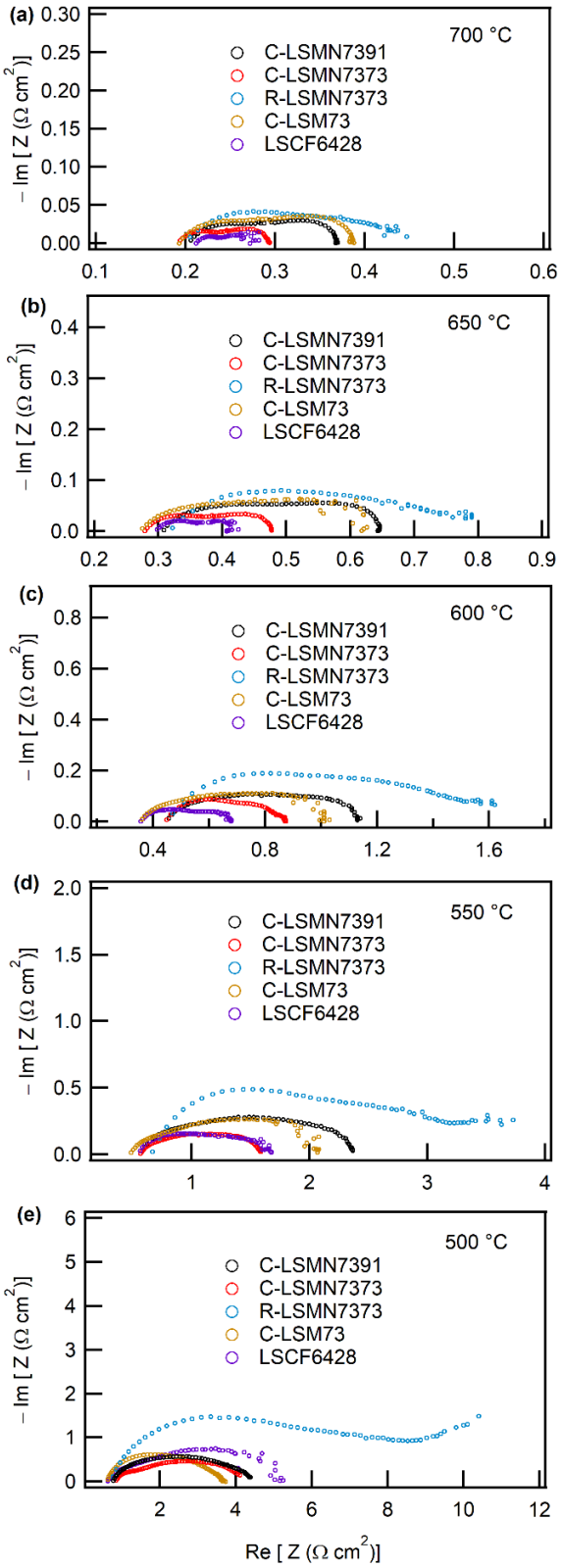


Figure 5-17 Electrochemical impedance spectroscopy of the anode-supported cells with various cathodes, measured at (a) 700, (b) 650, (c) 600, (d) 550 and (e) 500 ℃ under OCV condition.

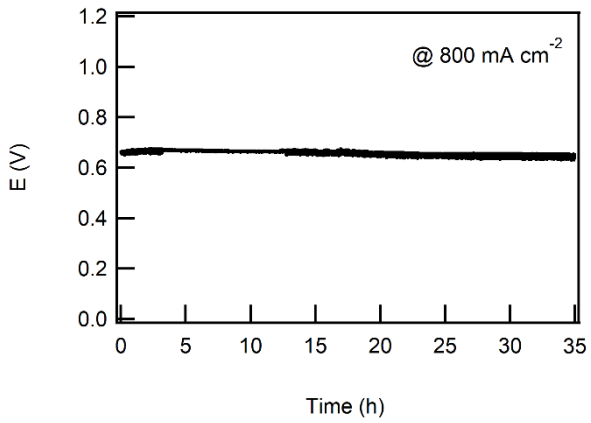


Figure 5-18 Durability test of C-LSMN7373 cell in a galvanostatic operation under 800 mA $cm^{-2}$ at 700 ℃.

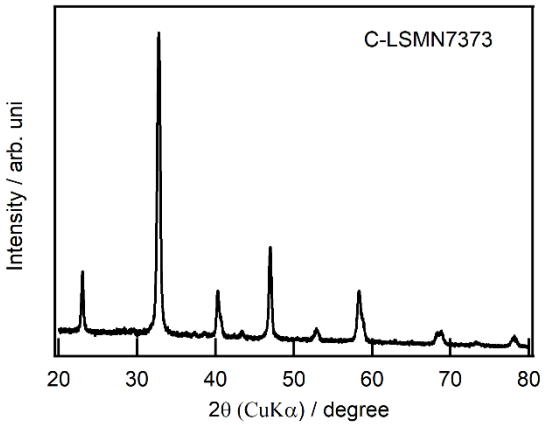


Figure 5-19 XRD pattern of C-LSMN7373 after the durability test shown in Figure 5-18.

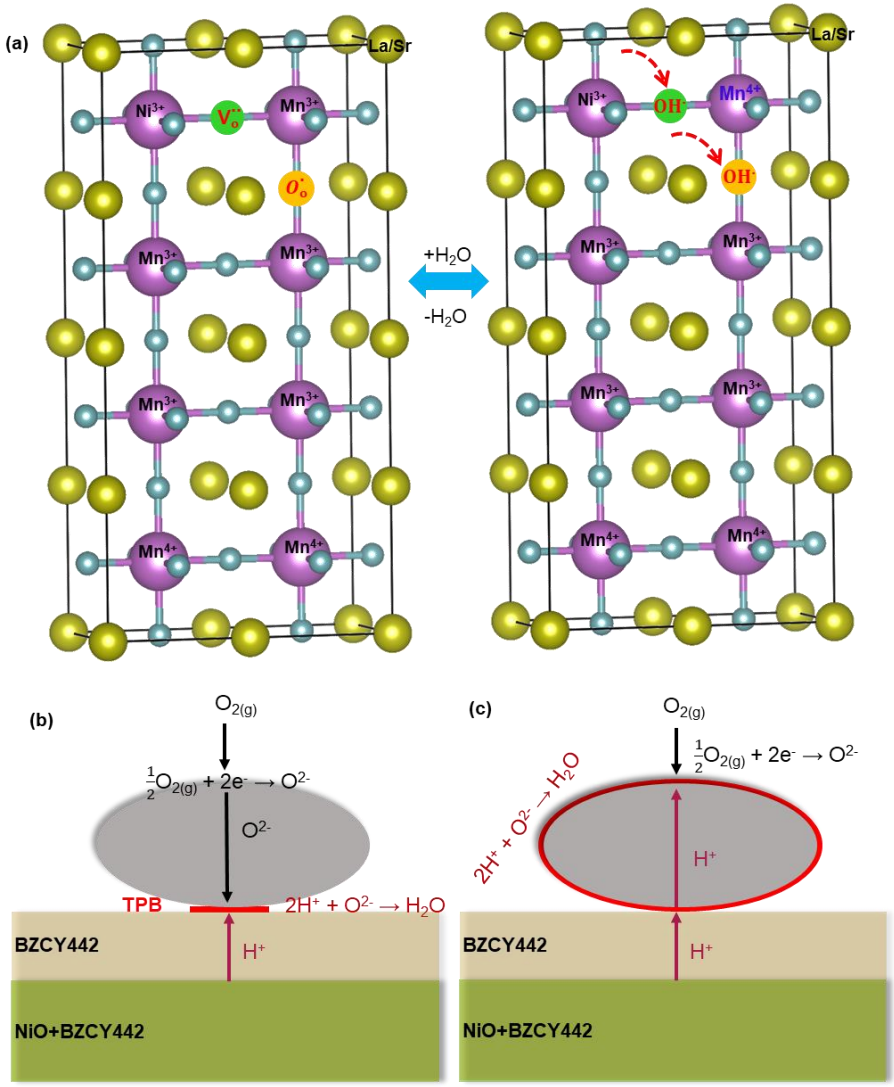


Figure 5-20 (a) Mechanism of thermochemical hydration/dehydration reaction for *C*-LSMN, schematic of cathode reaction of (b) $O^{2-}/e^{-}$ mixed conductors and (c) $H^{+}/O^{2-}/e^{-}$ triple conducting conductors on PCFCs.

## 5-4 Conclusions

In summary, we demonstrated that cubic-type $La_{0.7}Sr_{0.3}Mn_{1-x}Ni_xO_{3-\delta}$ (*C*-LSMN) are beneficial to $H^+/e^-/O^{2-}$ triple conducting cathodes intended for PCFCs operating at intermediate temperatures. *C*-LSMN undergoes thermochemical hydration at approximately 400 ℃ in air by gaining proton carriers of 0.2 mole fraction, which is quite similar to the concentration of the widely-used proton conducting ceramic $BaCe_{0.9}Y_{0.1}O_3$. However, rhombohedral-type $La_{0.7}Sr_{0.3}Mn_{0.7}Ni_{0.3}O_3$ (*R*-LSMN) does not undergo hydration because of the lack of oxygen vacancies. Accordingly, $BaZr_{0.4}Ce_{0.4}Y_{0.2}O_3$ thin film fuel cells with *C*-LSMN cathodes exhibited a lower polarization resistance than the analogous cells with the *R*-LSMN cathodes by one order of magnitude in the temperature range of 500–600 ℃, because the effective cathode reaction areas could be extended from triple phase boundaries to the overall cathode surface through enhanced proton conduction. In fact, the cell with cubic-type $La_{0.7}Sr_{0.3}Mn_{0.7}Ni_{0.3}O_3$ exhibited a similar cathodic polarization resistance as the cell with the widely-used LSCF6428 cathode and yielded peak power densities of 122 and 386 mW $cm^{-2}$ at 500 and 600 ℃, respectively. In conclusion, cubic-type $La_{0.7}Sr_{0.3}Mn_{1-x}Ni_xO_{3-\delta}$ is a promising Co-free cathode material for PCFCs operating at intermediate temperatures.

## 5-5 References


1. Y. Okuyama, N. Ebihara, K. Okuyama and Y. Mizutani, *ECS Trans.* 2009, **68**, 2545.
2. J. S. Park, J. H. Lee, H. W. Lee and B. K. Kim, *ECS Trans.* 2009, **25**, 795.
3. D. K. Lim, H. N. Im, B. Singh and S. J. Song, *Journal of The Electrochemical Society*, 2015, **162**, F547-F554.
4. Y. Guo, Y. Lin, R. Ran and Z. Shao, *Journal of Power Sources*, 2009, **193**, 400-407.
5. N. Nasani, D. Ramasamy, S. Mikhalev, A. V. Kovalevsky and D. P. Fagg, *Journal of Power Sources*, 2015, **278**, 582-589.
6. L. Bi, E. Fabbri and E. Traversa, *Electrochemistry Communications*, 2012, **16**, 37-40.
7. Y. Liu, Y. Guo, R. Ran and Z. Shao, *Journal of Membrane Science*, 2013, **437**, 189-195.
8. Y. Niu, W. Zhou, J. Sunarso, L. Ge, Z. Zhu and Z. Shao, *Journal of Materials Chemistry*, 2010, **20**, 9619-9622.
9. N. Wang, S. Hinokuma, T. Ina, H. Toriumi, M. Katayama, Y. Inada, C. Zhu, H. Habazaki and Y. Aoki, *Chemistry of Materials*, 2019, **31**, 8383-8393.
10. S. R. Bishop, D. Marrocchelli, W. Fang, K. Amezawa, K. Yashiro and G. W. Watson, *Energy & Environmental Science*, 2013, **6**, 1142.
11. S. Choi, C. J. Kucharczyk, Y. Liang, X. Zhang, I. Takeuchi, H.-I. Ji and S. M. Haile, *Nature Energy*, 2018, **3**, 202-210.
12. R. Zohourian, R. Merkle, G. Raimondi and J. Maier, *Advanced Functional Materials*, 2018, **28**, 1801241.
13. D. Poetzsch, R. Merkle and J. Maier, *Faraday discussions*, 2015, **182**, 129-143.
14. D. Poetzsch, R. Merkle and J. Maier, *Physical chemistry chemical physics : PCCP*, 2014, **16**, 16446-16453.
15. C. Duan, J. Tong, M. Shang, S. Nikodemski, M. Sanders, S. Ricote, A. Almansoori and R. O'Hayre, *Science*, 2015, **349**, 1321-1326.
16. K. Kreuer, *Solid State Ionics*, 1999, **125**, 285-302.
17. T. Norby and Y. Larring, *Current Opinion in Solid State and Materials Science*, 1997, **2**, 593-599.
18. D. K. Lim, M.-B. Choi, K. T. Lee, H.-S. Yoon, E. Wachsman and S. J. Song, *International Journal of Hydrogen Energy*, 2011, **36**, 9367-9373.
19. S.-J. Song, E. D. Wachsman, S. E. Dorris and U. Balachandran, *Solid State Ionics*, 2002, **149**, 1-10.
20. C. J. Park, H. W. Ryu, J. H. Moon, J. S. Lee and S. J. Song, *Ceramics International*, 2009, **35**, 1769-1773.
21. C. R. Fell, D. Qian, K. J. Carroll, M. Chi, J. L. Jones and Y. S. Meng, *Chemistry of Materials*, 2013, **25**, 1621-1629.

22. J. Rana, M. Stan, R. Kloepsch, J. Li, G. Schumacher, E. Welter, I. Zizak, J. Banhart and M. Winter, *Advanced Energy Materials*, 2014, **4**, 1300998.
23. C. Henderson, J. Charnock, J. Smith and G. Greaves, *American Mineralogist*, 1993, **78**, 477-485.
24. A. Gaur, B. D. Shrivastava and H. Nigam, *Proceedings of the Indian National Science Academy*, 2013, **79**, 921-966.
25. B. Wei, Z. Lü, X. Huang, M. Liu, N. Li and W. Su, *Journal of Power Sources*, 2008, **176**, 1-8.
26. B. Lengeler and P. Eisenberger, *Physical Review B*, 1980, **21**, 4507-4520.
27. J. H. K. H. U. Anderson, *JOURNAL OF SOLID STATE Chemistry of Materials*, 1989, **83**, 52-60.
28. S. Jeong, T. Kobayashi, K. Kuroda, H. Kwon, C. Zhu, H. Habazaki and Y. Aoki, *RSC Advances*, 2018, **8**, 26309-26317.
29. J. Xiao, W. Sun, Z. Zhu, Z. Tao and W. Liu, *Materials Letters*, 2012, **73**, 198-201.
30. C. L. Tsai, M. Kopczyk, R. Smith and V. H. Schmidt, *Solid State Ionics*, 2010, **181**, 1083-1090.
31. Y. Liu, R. Ran, M. O. Tade and Z. Shao, *Journal of membrane science*, 2014, **467**, 100-108.
32. W. Sun, L. Yan, Z. Shi, Z. Zhu and W. Liu, *Journal of power sources*, 2010, **195**, 4727-4730.
33. S. Choi, T. C. Davenport and S. M. Haile, *Energy & Environmental Science*, 2019, **12**, 206-215.

# Chapter 6 Summary

The work discussed in this thesis centered around design, fabrication, characterization of the mixed $H^+/O^{2-}/e^-$ triple conducting perovskites, and application of these oxides to protonic solid oxide cells for energy conversion. First, the mixed $H^+/O^{2-}/e^-$ triple conducting $La_{0.8}Sr_{0.2}Co_{1-x}Ni_xO_{3-\delta}$ (LSCN) and $La_{1-y}Sr_yMn_{1-x}Ni_xO_{3-\delta}$ (LSMN) were developed with the massive proton carries incorporation by hydration, which can be comparable with the well-known electrolytes, such as $BaCe_{0.9}Y_{0.1}O_3$ and $BaZr_{0.9}Y_{0.1}O_3$. Then, the hydration mechanisms of LSCN and LSMN were clearly elaborated, which give the guidelines to develop more efficient triple phase conductors. Finally, the efficiency of these mixed $H^+/O^{2-}/e^-$ triple conducting perovskites (*eg*. PCFCs and PCECs) were certified by application as the air electrodes of protonic ceramic cells. The outstanding results of this thesis were briefly summarized as follows:

Firstly, $La_{0.8}Sr_{0.2}Co_{1-x}Ni_xO_{3-\delta}$ (LSCN, $x$=0-0.3) oxides were demonstrated to exhibit bulk proton conduction at intermediate temperature region by pronounced hydration/dehydration reactions with retaining sufficient mole fraction of water under wet air atmosphere in at temperatures below 800℃. They gain bulk proton carriers at the range of 0.06-0.15 mole fraction by thermochemical hydration/dehydration reactions at around 400℃, which was carried out by the association reaction of oxygen vacancy and water via analyzing the Co, Ni *L*-edge and O *K*-edge spectra. The sufficiently high electrical performances close to the champion data were obtained by applying mixed $H^+/e^-/O^{2-}$ triple phase conducting LSCN oxides to the air electrodes of protonic ceramic cells based on Zr-rich $BaZr_{0.4}Ce_{0.4}Y_{0.2}O_3$ electrolyte. The current densities, peak power densities and polarization resistance reached 0.68 A $cm^{-2}$ at 1.3 V in electrolysis mode, 0.65 W $cm^{-2}$ in fuel cell mode, and 0.09 Ω $cm^2$ under open circuit voltage at 600℃, respectively, which are superior to the well-known $La_{0.6}Sr_{0.4}Co_{0.2}Fe_{0.8}O_3$ measured at the same conditions. The impressive electrical

performances indicate that mixed $H^+/e^-/O^{2-}$ triple phase conducting LSCN oxides are promising air electrodes for protonic ceramic cells operating in intermediate temperature region.

Secondly, cubic $La_{0.7}Sr_{0.3}MnO_{3-\delta}$ (C-LSM73) was found to gain large amounts of proton carriers (0.15 mole fraction) even at 415℃ at $p_{H2O}$ of 0.023 atm, which was much higher than the values reported for other perovskite-based triple conductors. The massive proton uptake was conducted via hydration/dehydration reactions, driven by the charge disproportionation between oxygen and manganese atoms. C-LSM73 undergoes the decline of antibonding O *2p* states hybridized with Mn *3d* orbitals together with oxidation of $Mn^{3+}$ to $Mn^{4+}$ by hydration. These results offer a general concept to design mixed $H^+/e^-/O^{2-}$ triple phase conductors operating in air conditions.

Thirdly, C-LSM73 and its derivates $La_{0.7}Sr_{0.3}Mn_{1-x}Ni_xO_{3-\delta}$ were evaluated as an air electrode of PCCs operating in the region of 500－600℃. C-$La_{0.7}Sr_{0.3}Mn_{0.7}Ni_{0.3}O_{3-\delta}$ (C-LSMN7373) were found to retain about 0.1 mole fraction $H_2O$ under wet air at 415℃ by the same thermochemical hydration reaction as C-LSM73. The cathode performances are examined by fabricating thin-film fuel cells with a $Ba(Zr_{0.4}Ce_{0.4}Y_{0.2})O_3$ electrolyte. The peak power density of the PCFCs with C-LSMN7373 cathode is comparable to the widely used $La_{0.6}Sr_{0.4}Co_{0.2}Fe_{0.8}O_3$ cathode, although the manganite perovskites normally show poor performances in comparison to the cobaltite ones due to the poor oxide ion conductivity. In conclusion, cubic-type LSMNs is a promising Co-free cathode material for PCFCs operating at intermediate temperatures.

When the dehydration reaction (6-1) spontaneously occurs at a temperature, the reaction free energy, $\Delta G_0(T)$, must be negative as follows.

$$2OH_O^{\bullet} \rightarrow O_O^X + V_O^{\bullet\bullet} + H_2O_{(g)} \qquad (6\text{-}1)$$

$$\Delta G_0(T) = \Delta H_0 - T\Delta S_0 \leq 0 \qquad (6\text{-}2)$$

Here, $\Delta H_0$ and $\Delta S_0$ are the dehydration enthalpy and entropy at a standard pressure $p_0$ = 100 kPa, respectively. Since the equilibrium of reaction 6-1 is dependent on $H_2O$ partial pressure ($p_{H2O}$), the $\Delta G(T, p_{H2O})$ at $p_{H2O}$ can be represented with $\Delta G_0(T)$ as follows:

$$\Delta G(T, p_{H2O}) = \Delta G(T) + RT \ln(p_{H2O}/p_0) \quad (6\text{-}3)$$

Under equilibrium, i.e., $\Delta G(T, p_{H2O}) = 0$, equation 6-3 is rewritten by

combining with equation 6-2:

$$(p_{H2O}/p_0) = \exp(\Delta S_0/R) \exp(-\Delta H_0/RT) \quad (6\text{-}4)$$

which provides the equilibrium water partial pressure at a given temperature.

Under a fixed $p_{H2O}$, equation 6-4 suggests that the dehydration of metal oxides progresses more by heating in the region above the threshold temperature ($T_{de}$), which given by the following.

$$-\Delta H_0/RT_{de} = \ln(p_{H2O}/p_0) - (\Delta S_0/R) \quad (6\text{-}5)$$

$T_{de}$ is the onset temperature of the dehydration, which is observed in TG curves (Fig. 3-3, 4-5, and 5-2). This indicates that higher $p_{H2O}$ is needed to establish defect equilibrium (6-1) at higher temperatures. In case of dehydration of metal oxides, $\Delta S_0$ is given by the mixing entropy related to the defect equilibrium (6-1) between oxygen vacancies and water gases, and thus can be approximated to ~120 J $K^{-1}$ $mol^{-1}$) at 673 K.[1] Accordingly, the dehydration enthalpy $\Delta H_0$ can be calculated by using equation 6-4 with the experimentally-observed $T_{de}$ and $p_{H2O}$.

LSCN and C-LSMN possesses $T_{de}$ of 430 and 450 ℃, respectively, at $p_{H2O}$ = 0.023 atm, as is observed in Figure 3-3, 4-5, and 5-2, respectively. Hence the hydration enthalpy ($\Delta H_{hyd}$), which is negative sign of $\Delta H_0$, are determined to -107 and -104 kJ $mol^{-1}$ for LSCN and C-LSMN, respectively. Based on the $\Delta H_{hyd}$ values, the $T_{de}$ of

LSCN and C-LSMN must become more than 500℃ with increasing $p_{H2O}$ to 0.1 atm, which indicates that both oxides can exhibit efficient proton conductivity even at the PCC's operation temperatures. Such $p_{H2O}$ is not surprisingly high in EC mode. It is concluded that LSCN and C-LSMN can exhibit efficient $H^+/e^-/O^{2-}$ triple conductivity even at temperatures above 500℃ due to the relatively large hydration enthalpy and thereby, are efficient air electrodes to extend reaction zones on proton conducting ceramic electrolyte cells. I firmly believe that this effort must be perused for designing higher/lower temperature mixed $H^+/e^-/O^{2-}$ triple phase conductors, and always hope that this thesis contributes to the further development of Solid State Ionics.

## References


1. Y. Aoki, K. Kuroda, S. Hinokuma, C. Kura, C. Zhu, E. Tsuji, A. Nakao, M. Wakeshima, Y. Hinatsu, and H. Habazaki, J. Am. Chem. Soc. 2017, **139**, 11197−11206.

# Publications

1. Ning Wang, Satoshi Hinokuma, Toshiaki Ina, Hajime Toriumi, Misaki Katayama, Yasuhiro Inada, Chunyu Zhu, Hiroki Habazaki, Yoshitaka Aoki; Incorporation of Bulk Proton Carriers in Cubic Perovskite Manganite Driven by Interplays of Oxygen and Manganese Redox; Chemistry of Materials, 2019, 31, 8383 − 8393.

2. Ning Wang, Satoshi Hinokuma, Toshiaki Ina, Chunyu Zhu, Hiroki Habazaki, Yoshitaka Aoki; Mixed Proton–electron–oxide Ion Triple Conducting Manganite as Efficient Cobalt-free Cathode for Protonic Ceramic Fuel Cells; Journal of Materials Chemistry A, 2020, 8, 11043-11055.

## Acknowledgements

First and foremost, I would like to give my sincerest gratitude to my supervisor, Dr. Yoshitaka Aoki. It has been a true pleasure to have the opportunity to learn from you during the three years (2017.10-2020.9) in the Laboratory of Interfacial Electrochemistry, Graduate school of Chemistry Science and Engineering, Hokkaido University. Thank you for supporting me with your kind guidance, patience, and profound knowledge.

I would also like to sincerely appreciate Professor Hiroki Habazaki, Assistant professor Chunyu Zhu, Assistant professor Sho Kitano, Dr. Damian Kowalski, and Ms. Yoko Iwata, in the Laboratory of Interfacial Electrochemistry, Faculty of Engineering, Hokkaido University. They give me selfless help in academic research, and life.

I would express my thanks to Dr. Satoshi Hinokuma, in National Institute of Advanced Industrial Science and Technology (AIST), Japan; Dr. Toshiaki Ina, in Japan Synchrotron Radiation Research Institute (JASRI); Dr. Misaki Katayama, Synchrotron Radiation Center, Research Organization of Science and Technology, Ritsumeikan University, Japan; Professor Tatsuya Kawada, Dr. Keiji Yashiro, Master student Kotaro Okuyama, in Tohoku University. They gave me a hand in experiment measurements, such like, in-situ FTIR, TDS, *in-situ* extended X-ray absorption fine structure (EXAFS), O K-edge X-ray absorption spectra, Secondary Ion Mass Spectrometry (SIMS).

Many thanks also extended to all the members of Laboratory of interfacial Electrochemical, who have helped a lot in life and academic research, and they made me enjoyable in this lab. Dr. Chiharu Kura, Dr. Chong Kim, Ms. Fadillah Laras, Mr. Yuki Sato, Mr. Seongwoo Jeong, Ms. Chunmei Tang, Mr. Hajime Toriumi, Mr. Ruijie Zhu, Mr. Kentaro Takase, Ms. Miku Saito, Mr. Hikaru Kobayashi, Ms. Minami Takata, Mr. Naohito Yamada, Mr. Shinichi Nishimura, Mr. Katsuuaki Akimoto, and other laboratory members.

Many thanks to *Chinese Scholarship Council* giving me the opportunity to pursue the doctoral degree in Hokkaido University.

I've saved the best for my family and my best friend Ms. Weiyan Li. Thank you for always being understanding and supporting. You always respect my choices and encourage me to have faith in my decisions. Thank you for always listening to whatever I am talking about and being helpful with all the solutions.